Universitat d'Alacant
Universidad de Alicante

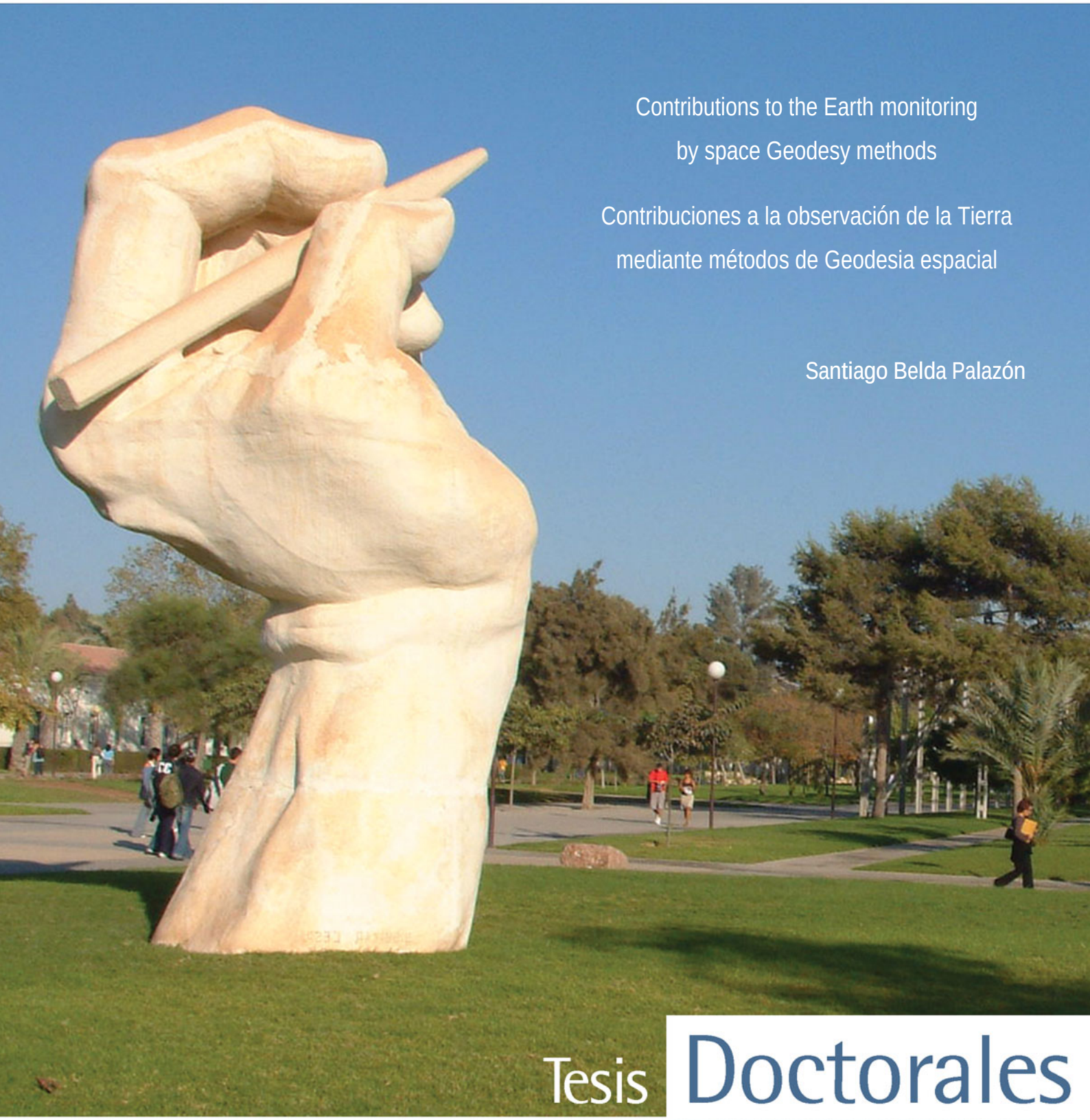

# Contributions to the Earth monitoring by space Geodesy methods

# Contribuciones a la observación de la Tierra mediante métodos de Geodesia espacial

Santiago Belda Palazón

Tesis Doctorales

www.eltallerdigital.com

UNIVERSIDAD de ALICANTE

UNIVERSIDAD DE ALICANTE

# CONTRIBUTIONS TO THE EARTH MONITORING BY SPACE GEODESY METHODS

---

# CONTRIBUCIONES A LA OBSERVACIÓN DE LA TIERRA MEDIANTE MÉTODOS DE GEODESIA ESPACIAL

SANTIAGO BELDA PALAZÓN

TESIS DOCTORAL

Alicante, 17 de Julio de 2015

Universitat d'Alacant
Universidad de Alicante

UNIVERSIDAD DE ALICANTE
DEPARTAMENTO DE MATEMÁTICA APLICADA
ESCUELA POLITÉCNICA SUPERIOR

# CONTRIBUTIONS TO THE EARTH MONITORING BY SPACE GEODESY METHODS

---

# CONTRIBUCIONES A LA OBSERVACIÓN DE LA TIERRA MEDIANTE MÉTODOS DE GEODESIA ESPACIAL

SANTIAGO BELDA PALAZÓN

MENCIÓN DE DOCTOR INTERNACIONAL
DOCTORADO EN MÉTODOS MATEMÁTICOS Y MODELIZACIÓN
EN CIENCIAS E INGENIERÍA

DIRIGIDA POR: DR. JOSÉ MANUEL FERRÁNDIZ LEAL

MEMORIA PARA OPTAR AL GRADO DE DOCTOR
POR LA UNIVERSIDAD DE ALICANTE

*Contributions to the Earth Monitoring by Space Geodesy Methods*

Author: Santiago Belda Palazón

Advisor: José Manuel Ferrándiz Leal

Universitat d'Alacant
Universidad de Alicante

Text printed in Alicante

# Agradecimientos

Gracias a mi director de tesis, el Dr. José Manuel Ferrándiz Leal, por confiar y creer en mí desde el primer día, sin el cual este trabajo no hubiera sido posible.

Por supuesto, no puedo dejar de agradecer al Dr. Mario Trottini y la Dra. Isabel Vigo Aguiar, quienes además de transmitirme su vocación investigadora, me orientaron y ayudaron constantemente.

Quiero dar las gracias al Dr. Harald Schuh y al Dr. Robert Heinkelmann por la calurosa acogida en su grupo de investigación.

Al proyecto AYA2010-22039-C02-01 del Ministerio de Ciencia e Innovación, por financiar la totalidad de este trabajo.

Gracias de verdad a mis compañeros de trabajo, David, Alberto, Pablo, Fernando, María del Carmen y Tomás, por sus consejos y recomendaciones, los cuales me han sido y son de gran utilidad.

Agradecer a mis padres y hermanos, Borja, Manuel y Cristina, por su apoyo incondicional de cada día. Sin ellos todos los logros conseguidos en mi vida no hubieran sido posibles.

Y gracias en especial a mi mujer, por estar siempre esperándome con una sonrisa llena de vida y alegría.

Universitat d'Alacant
Universidad de Alicante

Universitat d'Alacant
Universidad de Alicante

# Índice general

**Extended summary in Spanish (Resumen)** **vi**

0.1 Introducción . . . . . vii

0.2 Capítulo 2 . . . . . xi

0.2.1 Análisis de datos . . . . . xii

0.2.2 Estudios realizados . . . . . xiii

0.2.2.1 Señales geofísicas no modeladas . . . . . xiii

0.2.2.2 Diferentes series de EOP a priori . . . . . xiii

0.2.2.3 Marcos de referencia terrestres . . . . . xiv

0.2.2.4 Marcos de referencia celestes . . . . . xiv

0.2.2.5 Transformación de similitud vs. ERP . . . . . xiv

0.2.3 Resultados y conclusiones . . . . . xv

0.3 Capítulo 3 . . . . . xvi

0.3.1 Análisis VLBI: FCN . . . . . xvii

0.3.2 Modelos empíricos de FCN . . . . . xvii

0.3.3 Resultados . . . . . xviii

0.3.3.1 Ventanas móviles . . . . . xviii

0.3.3.2 Amplitud y fase . . . . . xviii

0.3.3.3 Comparación con otros modelos . . . . . xix

0.3.4 Discusión . . . . . xix

0.4 Capítulo 4 . . . . . xx

0.4.1 Descripción de los datos. Metodología . . . . . xx

0.4.2 Filtro de decorrelación . . . . . xxi

0.4.2.1 Tendencias lineales . . . . . xxi

0.4.2.2 GRACE vs. Datos sintéticos . . . . . xxii

Universitat d'Alacant
Universidad de Alicante

0.4.2.3 Continentes vs. Océanos . . . . . xxii
0.4.3 Filtro Gaussiano vs Filtro Fan . . . . . xxiii
0.4.4 Discusión . . . . . xxiii
0.5 Capítulo 5 . . . . . xxiv
0.5.1 Principal resultado . . . . . xxiv
0.5.2 Ejemplo . . . . . xxvi
0.5.3 Discusión y conclusión . . . . . xxvi

**1 Introduction 1**

**2 On the consistency of EOP series, ITRF and ICRF 15**
2.1 Introduction . . . . . 15
2.2 Consistency among reference frames and EOP. General aspects . . . . . 16
2.3 Data analysis . . . . . 18
2.4 Results . . . . . 20
2.4.1 Unmodeled geophysical signals . . . . . 20
2.4.2 Different a priori EOP series . . . . . 22
2.4.3 Terrestrial Reference Frames . . . . . 24
2.4.4 Celestial Reference Frames . . . . . 27
2.4.5 Similarity transformation vs. VLBI ERP differences . . . . . 28
2.5 Discussions and Conclusions . . . . . 30

**3 Testing a new Free Core Nutation empirical model 33**
3.1 Introduction . . . . . 33
3.2 FCN modeling in VLBI data . . . . . 35
3.3 Empirical FCN models . . . . . 36
3.4 Results . . . . . 38
3.4.1 Sliding Window: Size and Displacement . . . . . 38
3.4.2 Amplitude and phase . . . . . 41
3.4.3 Comparison with other models . . . . . 43
3.5 Discussions and Conclusions . . . . . 44

Universitat d'Alacant
Universidad de Alicante

**4 On the Decorrelation Filtering of RL05 GRACE data** **47**
4.1 Introduction . . . . . 47
4.2 Data description and methodology . . . . . 48
4.3 First-Step Filter . . . . . 53
4.3.1 Linear trends . . . . . 53
4.3.2 GRACE versus synthetic data . . . . . 56
4.3.3 Contienents versus ocean . . . . . 59
4.3.4 Parameters selection . . . . . 60
4.4 Second-Step filter . . . . . 62
4.5 Discussion . . . . . 65

**5 A Cautionary Note on the Use of Running Trends** **69**
5.1 Introduction . . . . . 69
5.2 Main Result . . . . . 71
5.3 An Illustration . . . . . 72
5.4 Discussion . . . . . 80
5.5 Conclusions . . . . . 82

**A Appendix** **85**
A.1 Running Trends Analysis: Proof of the Main results . . . . . 85

**References** **87**

**Acronyms** **97**

Universitat d'Alacant
Universidad de Alicante

Universitat d'Alacant
Universidad de Alicante

*La conquista propia es la más grande de las victorias*

Plato

# Extended summary in Spanish (Resumen)

## 0.1 Introducción

Hoy en día, conocer con gran precisión el movimiento de rotación de la tierra es esencial para multitud de aplicaciones cientifico-técnicas (geodesia, astronomía, navegación espacial y geodinámica), además de beneficioso para intentar entender por completo el cambiante sistema tierra. El estudio clásico de la rotación de la tierra considera los movimientos del eje de rotación desde dos puntos de vista diferentes, terrestre y espacial (fig. 1.1). Cinco Parámetros de Orientación de la tierra (EOP) proporcionan la relación entre el Marco de Referencia Terrestre Internacional (ITRF) y el Marco de Referencia Celeste Internacional (ICRF): las coordenadas del polo $(x_p, y_p)$, las correcciones al Polo Celeste por precesión y nutación $(dX, dY)$ y el Tiempo Universal (UT1) o su equivalente Ángulo de Rotación de la Tierra (ERA) [Petit and Luzum, 2010]. Series temporales de EOP son proporcionadas por diferentes organismos, siendo los más destacados el Observatorio Naval de los EEUU (USNO) y el Servicio Internacional de Rotación de la Tierra y Sistemas de Referencia (IERS). Este último es el responsable de modelar y predecir la rotación de la tierra, así como de elaborar y mantener el ICRF e ITRF. En la nota técnica del IERS 2010 ("IERS Conventions 2010") los EOP se definen como los ángulos de tres matrices de rotación ($Q$, $R$ y $W$) que relacionan la orientación del Sistema de Referencia Celeste geocéntrico (GCRS) con la del ITRF (ecuación 1.1) [Petit and Luzum, 2010].

El Sistema de Observación Geodésico Global (GGOS) integra las diferentes técnicas geodésicas, diferentes modelos y métodos para conseguir un mejor entendimiento de los procesos geodinámicos y del cambio global. GGOS, por tanto, presenta la base científica e infraestructural para todas las investigaciones geodésicas, siendo su principal objetivo

asegurar la consistencia entre las tres áreas fundamentales de la geodesia (figura 1.7): Geometría, Orientación y el Campo Gravitatorio. El ITRF e ICRF son la base para la mayoría de observaciones geodésicas, jugando un papel fundamental en GGOS. Esto quiere decir que las imprecisiones en cualquiera de estos dos marcos limitarán la calidad de las observaciones, y podrían dar lugar a interpretaciones erróneas de los resultados. Por ejemplo, un error de 1 $mm\ y^{-1}$ en la velocidad relativa entre la superficie media y el centro de masas de la tierra puede llevar a imprecisiones del orden de 0.4 $mm\ y^{-1}$ en la medición del nivel medio del mar [Kierulf and Plag, 2006].

La interferometría de muy larga base (VLBI) es una de las técnicas más precisas para estudiar, modelar y controlar los EOP, además de ser el único método capaz de definir marcos de referencia celestes y medir la rotación de la tierra respecto a este marco. Esta técnica radioastronómica lleva operativa más de 40 años, siendo extremadamente útil para multitud de aplicaciones geodésicas (exploración del sistema solar, variaciones en el nivel del mar, determinación precisa de órbitas, estudios de rotación de la tierra, etc) algunas de las cuales podrían parecer a primera vista poco relacionadas, pero en realidad dependen de las realizaciones de los marcos de referencia. VLBI mide la diferencia de tiempo ($\tau$, retardo geométrico o ”delay“) en la recepción de la señal de microondas emitida por radiofuentes extragalácticas que es recibida simultáneamente en dos o más radiotelescopios [Schuh and Böhm, 2013]. Con la ecuación 1.2 es posible estimar esta diferencia de tiempo, donde $\mathbf{b}$ es la distancia entre las antenas que observan simultáneamente a la misma fuente (línea-base o ”baseline“) y $\mathbf{s_0}$ es la dirección a la fuente o cuásar (figura 1.2).

Para la determinación precisa de las posiciones que definen los marcos de referencia terrestre y celeste es imprescindible medir, desde una red global de radiotelescopios VLBI situados en la superficie terrestre, un gran número de diferencias de tiempo ($\tau$) provenientes de multitud de cuásares que se encuentran distribuidos de manera homogénea por toda la bóveda celeste. Estas observaciones suelen verse afectadas por una serie de errores (retardos troposférico, ionosférico, relativístico, debido al instrumental, etc) que deben ser corregidos [Cannon, 1999] para alcanzar precisiones subcentimétricas en el cálculo de las líneas-base y de unos pocos microarcosegundos ($\mu as$) en la determinación de las posiciones de las radiofuentes extragalácticas. Debido a que las antenas VLBI se encuentran fijas a la superficie terrestre, cualquier cambio en sus coordenadas estará íntimamente ligado, entre otra muchas cosas, a variaciones de los EOP.

Normalmente, la estrategia seguida para estudiar los EOP, así como en cualquier otro tipo de medición geodésica, consiste en un proceso iterativo que está dividido en 4 etapas (figura 1.3) [Dehant et al., 2005; Schuh and Böhm, 2013]:

1. Se calculan modelos de EOP utilizando observaciones geodésicas, modelos convencionales y experimentos realizados en laboratorio.

2. Estos modelos de EOP son aplicados para predecir nuevos EOP.

3. Los valores predichos (calculados) son comparados con las observaciones geodésicas (Observado menos calculado).

4. Finalmente, estos residuales son estudiados y analizados para inferir en nuevos modelos de EOP.

El sistema VLBI de hoy en día emplea las bandas S (2.2-2.4 GHz) y X (8.2-8.95 GHz) para medir las diferencias de tiempo ($\tau$), generalmente haciendo uso de sesiones de observación de aproximadamente 24 horas. Debido a la necesidad de determinar las variaciones en los EOP con una elevada resolución temporal (mediciones continuas durante los siete días de la semana) y de utilizar amplias bandas del espectro electromagnético, se está desarrollando un nuevo sistema VLBI (VLBI2010) que se espera esté operativo en los próximos años [Petrachenko, 2009]. España y Portugal están desarrollando una nueva red de cuatro radiotelescopios ubicados en Madrid, Canarias y Azores. Esta red conocida como RAEGE (Red Atlántica de Estaciones Geodinámicas y Espaciales), tiene previsto mejorar las mediciones geodésicas a consecuencia de que todos sus radiotelescopios estarán equipados con las especificaciones de diseño de VLB2010 o VGOS (Sistema de Observación Geodésico VLBI). Las investigaciones realizadas por Belda et al. [2014a] comprobaron el sustancial avance que producirá en los EOP la integración de los radiotelescopios RAEGE en la red global de VLBI (figura 1.4).

Disponer de observaciones globales es de gran utilidad para poder caracterizar rigurosamente los cambios espaciales y temporales a los que está sometido continuamente el planeta Tierra, teniendo estos cambios a su vez una gran repercusión sobre el campo gravitatorio y la rotación de la Tierra. Por un lado, cualquier desplazamiento de masa producido en el interior o exterior de la superficie terrestre, provocará un cambio en el campo gravitatorio. Por otra parte, un movimiento de masa provocará una perturbación en el tensor

Universitat d'Alacant
Universidad de Alicante

de inercia de la Tierra, afectando a su rotación (definida por ley del momento angular). De manera que un mejor conocimiento de estas variaciones otorgará una mayor información sobre la dinámica terrestre [Chao, 1994]. De lo expuesto anteriormente se puede deducir que las fluctuaciones temporales de gravedad posibilitan el estudio de la rotación terrestre y viceversa. Por lo tanto, un análisis conjunto del campo gravitatorio y de los EOP ayudará a entender los procesos geofísicos que gobiernan el sistema Tierra [Peters et al., 2002]. Para que estas distribuciones de masa repercutan significativamente en la geodinámica terrestre tiene que suceder que grandes cantidades de masa sean desplazadas enormes distancias [Chao, 1994].

Actualmente, la Geodesia contribuye a modelar una gran variedad de procesos geofísicos (el deshielo, la redistribución de las aguas continentales, el nivel del mar, el ajuste isostático o ajuste postglacial, la circulación oceánica y atmosférica, la marea lunisolar, el movimiento de las placas tectónicas y la convección del manto) para lograr entender qué causas y consecuencias son las que producen las variaciones en los EOP (figura 1.5). En el sistema de referencia celeste es posible detectar variaciones pequeñas pero no despreciables, del eje de rotación de la Tierra debido a las diferentes propiedades de los materiales de que están compuestos el núcleo y la corteza terrestre (fluído y sólido). Esta es la razón que hace que los eje de rotación de las citadas capas diverjan ligeramente el uno del otro, provocando un pequeño cabeceo del eje de rotación de la Tierra con un periodo cercano a los 430 días y una amplitud media de aproximadamente 100 $\mu as$ (FCN). A causa de que el FCN presenta un complejo patrón de comportamiento, en el que predominan las excitaciones geofísicas, los modelos teóricos (teoría de nutación IAU2000) no son capaces de predecirlo, teniendo que ser complementados con precisos modelos empíricos de FCN [Krásná et al., 2013; Lambert, 2007; Malkin, 2010].

La distribución y transferencia de masa es determinante para entender la evolución de nuestro clima. Los importantes avances de las mediciones gravimétricas, han permitido detectar cambios de masa producidos en los fluidos geofísicos y en el interior del planeta Tierra con precisiones del orden de hasta $10^{-9}g$ [Blewitt et al., 2010]. Estos cambios, que se ven reflejados en variaciones temporales de la gravedad, pueden ser estimados por diferentes misiones satelitales (CHAMP, GRACE, GOCE). La misión GRACE (Gravity Recovery And Climate Experiment) consiste en dos satélites que siguen la misma órbita circular, separados una distancia de aproximadamente 220 km, capaces de estimar mediante

el uso de Coeficientes de Stokes (SC) las variaciones que sufre el campo gravitatorio a partir de las variaciones de la distancia que les separa.

Las observaciones del campo gravitatorio realizadas por GRACE y GOCE (Gravity Field and Steady-State Ocean Circulation Explorer) son sensibles a cualquier variación de masa, pudiendo ser de gran utilidad para investigar la rotación terrestre, cambios en el nivel del mar (SLV), alteraciones en la forma del geoide (superficie equipotencial definida por el nivel medio del agua de los mares por debajo de los continentes), la capa de hielo en Groenlandia y la Antártida, etc. Estas observaciones, que no son sensibles a cambios inducidos por la temperatura y salinidad del agua del mar, junto con las mediciones de satélites altimétricos pueden ser utilizadas para determinar la variación del nivel del mar correspondiente al efecto estérico [Watts and Morantine, 1991].

Como se ha comentado, los cambios de la rotación terrestre no son independientes de las variaciones del nivel del mar y el campo gravitatorio. Como consecuencia de esta sólida asociación, los capítulos abordados en esta tesis van dirigidos a ampliar conocimientos en estas tres diferentes, pero conectadas, áreas fundamentales de la Geodesia, con el fin de contribuir a alcanzar los exigentes niveles de precisión y estabilidad definidos por el Sistema de Observación Geodésico Global. En el capítulo 2 se estudia la estabilidad a largo plazo de los actuales marcos de referencia terrestre y celeste, así como de la serie convencional de EOP, todo ello analizando observables VLBI. En el capítulo 3, utilizando estas mismas sesiones VLBI pero con distintas opciones de procesado, se infieren nuevos modelos empíricos de FCN de una elevada resolución temporal. En el capítulo 4 se optimizan los parámetros del filtro de decorrelación para la nueva versión de datos GRACE (RL05) con el propósito de lograr alcanzar una mejor determinación del campo gravitatorio terrestre. Por último, en el capítulo 5 se presenta una fórmula con la que se demuestra que el análisis de las series temporales por tendencias móviles (”Running Trend Analysis”), está sometido a ciertas particularidades que deben de ser conocidas para evitar interpretaciones incorrectas de cualquier observación climática o geodésica, como pueden ser las relacionadas con la variación del nivel del mar (SLV).

## 0.2 Capítulo 2

Un gran número de aplicaciones científico-técnicas, tanto terrestres como espaciales, así como de uso militar y civil, requieren de un alto nivel de precisión en la transformación entre

el ITRF y el ICRF. Es por esto que GGOS reclama exigentes niveles de precisión y estabilidad a los marcos de referencia, 1 mm y 0.1 mm/año respectivamente. Algunas de las razones por las que aún no se ha logrado conseguir dicho propósito podrían ser debidas al diferente procedimiento llevado a cabo en la elaboración del ITRF (basado en las técnicas VLBI, SLR, GNSS y DORIS) y del ICRF (basado solo en VLBI), provocando diferencias en geometría, orientacíon y escala. Por otra parte, la serie de EOP IERS 08 C04 no se encuentra perfectamente alineada con los respectivos marcos de referencia terrestres y celestes. Todas estas pequeñas perturbaciones podrían ser transmitidas a los EOP, provocando inexactitudes en las transformaciones entre el ITRF y el ICRF. A consecuencia de lo comentado anteriormente, el principal objetivo de este capítulo ha ido dirigido a evaluar la consistencia y la estabilidad a largo plazo entre los marcos de referencia convencionales (ITRF2008 [Altamimi et al., 2011]; ICRF2 [Fey et al., 2004]) y la serie oficial de EOP (IERS 08 C04).

Los diferentes análisis VLBI que se han llevado a cabo para intentar cuantificar numéricamente si se cumple con el riguroso objetivo que demanda GGOS han consistido en: (1) comparar varias series de EOP que han sido estimadas usando diferentes TRF (tabla 2.2); (2) analizar el efecto que tiene en los EOP las señales geofísicas no modeladas (por ejemplo, el desplazamiento no lineal que sufren los puntos que definen los TRFs); (3) investigar el impacto que tiene en los EOP el uso de diferentes series de EOP a priori (USNO Finals y IERS 08 C04), así como la utilización de distintos marcos de referencia celestes (ICRF2 y ICRF-ext. 2) (tabla 2.1); (4) comparar los Parámetros de Rotación de la Tierra (ERP) estimados con diferentes TRF con las rotaciones globales de los respectivos marcos.

### 0.2.1 Análisis de datos

La estabilidad entre los marcos de referencia y la serie de EOP ha sido analizada mediante sesiones VLBI comprendidas entre 1984-07-09 y 2013-12-31. El software empleado para el análisis fue VieVS (Vienna VLBI Software) [Böhm et al., 2012] (versión proporcionada por el GFZ, Centro de Investigación Alemán de Geociencias). Por cada sesión VLBI, se calcularon las diferencias ("offsets" o desplazamientos) de los EOP entre el valor VLBI observado y el predicho por el modelo (EOP a priori). Con el objetivo de ser completamente consistente y alcanzar el mayor grado de coherencia, solo se utilizaron los EOP que fueron estimados con un estimador a posteriori de la desviación típica de peso unidad menor a 3 ($< 3\sigma$).

Para poder comparar y estudiar la consistencia entre todas las series temporales de EOP que han sido estimadas con distintas opciones de procesado, se calculó la media ponderada (WM), el valor cuadrático medio ponderado (WRMS) [Nilsson et al., 2014] y un ajuste lineal de las diferencias entre cualquier par de series. La regresión lineal ha sido calculada utilizando el método de mínimos cuadrados, determinando de este modo los dos coeficientes de la recta que mejor se ajustan a los residuales (a las diferencias): el término independiente (en este estudio la órdenada en el origen está referida a la época J2000.0) y la tendencia o deriva.

### 0.2.2 Estudios realizados

#### 0.2.2.1 Señales geofísicas no modeladas

Un gran número de señales geofisicas que interactúan con el sistema tierra no se tienen en cuenta en el procesado de sesiones VLBI. Además, no todas las señales geofísicas que han sido modeladas con complejas funciones matemáticas, representan el fenómeno con completa certidumbre. Un ejemplo claro de todo esto se puede ver en el modelo utilizado para definir las coordenadas de las antenas VLBI, donde solo se han considerado desplazamientos lineales, despreciando cualquier tipo de aceleración. Por tanto, la omisión de ciertas señales geofísicas en el procesado y las deficiencias que tienen los propios modelos recomendados por IERS [Petit and Luzum, 2010] podrían transmitir imprecisiones en el cálculo de EOP y ambigüedad en la estimación de TRF. Para estudiar cómo repercute la omisión de este tipo de señales en los EOP y en los marcos de referencia se calcularon dos series de EOP con diferentes opciones de procesado:

- Fijando las coordenadas de las estaciones a los valores nominales del ITRF2008 (las señales geofísicas no modeladas se propagarán en los EOP)
- Ajustando las coordenadas del ITRF2008 a otras nuevas posiciones (las señales geofísicas no modeladas producirán ligeras variaciones de las coordenadas)

#### 0.2.2.2 Diferentes series de EOP a priori

En un hipotético escenario ideal, se podría asegurar que el proceso iterativo llevado a cabo en VieVS tendría que converger a una única solución, independientemente de los valores a priori utilizados. Sin embargo, en la realidad esto no sucede, ya que desde el punto de visto

físico o matemático la estimación precisa de los EOP no es nada simple. Para resolver este tipo de cuestiones se calcularon varias series de EOP utilizando diferentes valores de EOP a priori, junto con los actuales marcos de referencia (ITRF2008 y ICRF2). En la primera serie se utilizaron los datos de IERS 08 C04 (caso 1). En la segunda, se emplearon los ERP y las coordenadas del polo celeste de la serie IERS 08 C04 y del modelo de precesión-nutación 2006/2000A respectivamente (caso 2). Por último se usaron los valores a priori de la serie USNO Finals (caso 3).

#### 0.2.2.3 **Marcos de referencia terrestres**

Con el fin de detectar algún tipo de inconsistencia entre los diferentes TRFs (tabla 2.2) se calcularon varias series de EOP fijando diferentes marcos de referencia terrestres y utilizando la serie de EOP IERS 08 C04 y ICRF2 como valores a priori. El procesado llevado a cabo en está sección no es válido para estimar precisos EOP, sin embargo es el único modo de descubrir rigurosamente posibles inconsistencias. La explicación se encuentra en que si las coordenadas de cada TRF no fueran fijadas a sus valores a priori, estas cambiarían, impidiendo cuantificar cualquier discrepancia.

#### 0.2.2.4 **Marcos de referencia celestes**

Siguiendo la misma línea de investigación que hasta ahora, donde se ha estudiado el efecto que tiene el empleo de diferentes series de EOP a priori, así como de diferentes TRFs, nos vimos obligados a testear los cambios en la solución a consecuencia de utilizar diferentes marcos de referencia celestes (ICRF2 y ICRF-ext.2) (tabla 2.1). En este caso, el análisis de las sesiones VLBI se realizó con el ITRF2008 y con la serie de EOP IERS 08 C04.

#### 0.2.2.5 **Transformación de similitud vs. ERP**

Para investigar si las diferencias entre las series de EOP que fueron estudiadas en la sección 0.2.2.3 pueden ser atribuidas a diferencias en orientación entre los distintos marcos de referencia terrestres, se utilizó una transformación Helmert de 6 parámetros. Esta transformación fue calculada entre los marcos indicados en la tabla 2.2 con respecto al ITRF2008. Por cada sesión VLBI, fueron estimadas tres traslaciones y tres rotaciones ($T_x, T_y, T_z, R_1, R_2, R_3$), utilizando sólo las coordenadas de las antenas VLBI que participaban en esa sesión. El factor de escala no fue incluido en el ajuste. La ecuación 2.2

muestra la transformación de similitud que fue utilizada, donde $x_i$, $y_i$, $z_i$ son las coordenadas cartesianas del punto i-ésimo común entre dos marcos de referencia, el ITRF2008 y el TRF considerado. Mediante la ecuación 2.3, los ERP fueron comparados con las rotaciones globales $R_1, R_2, R_3$.

### 0.2.3 Resultados y conclusiones

VLBI es la única técnica capaz de materializar marcos de referencia celestes, a parte de ser el único método de medición geodésico capacitado para determinar problemas de inconsistencia entre los marcos celestes y terrestres. Esto se demuestra con los resultados de la regresión lineal expuestos en la tabla 2.7, donde las rotaciones globales estimadas con la transformación de Helmert y los ERP calculados con sesiones de VLBI presentan una gran similitud.

Respecto al estudio que se expuso en la sección 0.2.2.1, se puede concluir que las señales geofísicas no modeladas en el análisis VLBI afectan negativamente a las coordenadas del polo y a $dUT1$ (tabla 2.3), especialmente en $y_{pol}$, con una deriva de 2.9 $\mu as\ yr^{-1}$ y un desplazamiento de -33.5 $\mu as$.

Otro punto importante a destacar es el impacto que produce en la solución final la utilización de diferentes modelos de EOP (tabla 2.4). Uno de los resultados más significativos se produjo entre las series de EOP que fueron estimadas con IERS 08 C04 y USNO Finals, revelando un significativo WRMS de las diferencias de 80 $\mu as$ en el parámetro $dUT1$ (figura 2.2). Por otra parte, las grandes diferencias (WRMS cerca de 160 $\mu as$) encontradas entre las coordenadas del polo celeste estimadas con el caso 1 (libre de FCN) y el caso 2 (afectado por el FCN) (figura 2.2) son debidas a que el modelo de precesión-nutación IAU 2006/2000A sólo modela los efectos que son fáciles de predecir, omitiendo el complejo FCN. Esto constata la importancia de disponer de precisos modelos para poder caracterizar y predecir el FCN. Cuanto mejor sean estos modelos, mejor será la determinación de los EOP.

Diferentes series de EOP calculadas con varios marcos de referencia celestes (ICRF2 y ICRF-ext.2) han ratificado que el análisis de VLBI no depende significativamente de las coordenadas de las fuentes extragalácticas. Las máximas diferencias en EOP (9.9 $\mu as$ en $\Delta X$ y 1 $\mu as\ yr^{-1}$ en $\Delta Y$) (figura 2.6) cumplen con el objetivo de estabilidad de 10 $\mu as$

perseguido por GGOS. Por la tanto, las orientaciones del ICRF2 y ICRF-ext.2 pueden suponerse prácticamente idénticas. Es importante mencionar que los EOP son más sensibles a los errores cometidos en las posiciones de los radiotelescopios que de los cuásares.

Al contrario que sucedió en el estudio anterior, varios problemas de inestabilidad surgieron entre las series temporales de EOP que fueron estimadas fijando diferentes marcos de referencia terrestres. Aunque el ITRF2008, ITRF2005 y ITRF2000 están constreñidos a no presentar diferencias en orientación (condición "No-Net-Rotation", NNR) mayores a 8 $\mu as$ y 8 $\mu as\ yr^{-1}$, los resultados obtenidos (ver figura 2.4) reflejan valores significativamente mayores, en particular en las coordenadas del polo entre el ITRF2000 y el ITRF2008. Los resultados del ajuste lineal de las diferencias entre los diferentes TRFs que aparecen en la tabla 2.5 revelan que VTRF2008 tiende a separarse a -19.9 $\mu as\ yr^{-1}$ en $y_{pol}$ con respecto el ITRF2008, con lo que los convencionales marcos de referencia (ICRF2, ITRF2008) y la serie de EOP IERS 08 C04 no son completamente consistentes. Las diferencias de orientación entre el ITRF2000 y ITRF2008 exhiben una desmesurada deriva en $x_{pol}$ de 19.3 $\mu as\ yr^{-1}$. El parámetro $dUT1$ evidencia importantes inconsistencias en todos los marcos de referencia terrestres que se han estudiado, en particular entre el DTRF2008 y el ITRF2008.

Durante estos últimos 30 años se ha conseguido determinar los EOP con un elevado nivel de precisión, poniendo cada vez más difícil cualquier tipo de mejora. A pesar de este adelanto, nuestro estudio confirma que la serie de EOP IERS 08 C04 no es todavía lo suficientemente precisa como para poder alcanzar el objetivo definido por GGOS. Algunas de las inconsistencias detectadas podrían tener su origen en (1) la combinación de soluciones de varias técnicas geodésicas para materializar el ITRF2008, (2) debido a que el actual TRF hereda la orientación de sus predecesores y (3) el hecho de no modelar la totalidad de las señales geofísicas.

## 0.3 Capítulo 3

El movimiento del eje de rotación de la tierra en el espacio, o más concretamente, en el marco de referencia celeste viene descrito por la teoría de precesión-nutación IAU 2000A, teniendo a su vez que ser complementada con otro modelo que ayude a explicar el cabeceo al que está sometido el eje de rotación terrestre debido a la distinta orientación que presenta el eje de rotación del manto con respecto al núcleo (FCN) [Smith, 1977; Toomre,

1974; Wahr, 1981]. Ningún modelo teórico es capáz de predecir este efecto a causa de su gran variabilidad. Hoy en día, VLBI es la única técnica que permite estimar estas variaciones (nutaciones de aproximadamente 430 días con una amplitud media de 100 $\mu as$). La mejora en el modelado de la rotación de la tierra, pasa por poder determinar modelos que traten de describir lo más precisamente posible el FCN. Es por ello que en este capítulo se han desarrollado y estudiado un gran número de nuevos modelos empíricos basados en observaciones VLBI que fueron analizadas con el programa VieVS. Para explorar el nivel de mejora respecto a los modelos ya existentes, nuestras estimaciones fueron comparadas con los modelos ofrecidos por Krásná et al. [2013] y Lambert [2007], siendo este último el recomendado por "IERS Conventions 2010" (nota técnica 36) [Ma et al., 2009]. Por último, se analizó cómo influye en los modelos empíricos de FCN que estos hayan sido calculados con diferentes series de EOP (IERS 08 C04 y USNO Finals).

### 0.3.1 **Análisis VLBI: FCN**

Es bien conocido que $dX$ y $dY$ proporcionan los desplazamientos ("offsets") del polo celeste con respecto a la posición definida por los modelos de precisión-nutación de la IAU. Desde 1984, es posible determinar estas correcciones con gran precisión gracias a las observaciones VLBI, capaces incluso de detectar la oscilación producida por el FCN, objeto de estudio en este capítulo. Esta fue la principal razón por la que se volvío a hacer uso de la técnica VLBI. Para este análisis, se utilizaron las mismas sesiones que en el capítulo anterior (1984-2013), descartando los EOP con un estimador a posteriori de la desviación típica de peso unidad mayores a 3. Al contrario que sucedió en la sección 0.2.2.3, las velocidades y posiciones de todas las estaciones y fuentes extragalácticas fueron estimadas para conseguir resultados de gran calidad.

### 0.3.2 **Modelos empíricos de FCN**

La ecuación 3.1 fue utilizada para estimar los modelos empíricos de FCN, donde $\sigma = 2\pi/P$ es la frecuencia angular del FCN en el marco de referencia celeste, $A$ es la amplitud, $t$ es el tiempo relativo a J2000.0 y $P$ es el periodo. Las razones por la que la amplitud y fase del FCN no son fijas en el tiempo son una gran incógnita y necesitan ser urgentemente identificadas. Esto nos llevó a analizar una gran variedad de modelos empíricos que fueron ajustados con diferentes ventanas móviles (SW) que oscilaban entre 8 meses

y 7 años ($N_L$) y variando el desplazamiento entre los ajustes consecutivos entre 1 y 12 meses ($N_D$). Todo ello, con el propósito de encontrar la configuración óptima que consiguiese los menores residuales y ayudase a su vez a identificar las causas geofísicas que originan su elevada variabilidad. Para todos los modelos ajustados en este estudio se adoptó un periodo constante de $-431.18$ días sidéreos, valor recientemente estimado por Krásná et al. [2013]. Esto nos permitió estimar amplitudes con tamaños de ventana $N_L$ menores al periodo del FCN, siendo por lo tanto capaces de estimar modelos con una excepcional resolución temporal.

Para estimar los modelos de FCN, se hizo uso de varias soluciones de EOP que fueron calculadas mediante VLBI con diferentes series a priori de ERP (IERS 08 C04 y USNO Finals) y utilizando las coordenadas del CIP (polo celeste intermedio) del actual modelo de nutación. Todos estos modelos fueron derivados de las diferencias entre las coordenadas del polo celeste determinadas con VLBI y las coordenadas predichas por el modelo IAU 2000A (figura 3.1).

### 0.3.3 **Resultados**

#### 0.3.3.1 **Ventanas móviles**

Una gran variedad de modelos de FCN con distintas configuraciones y basados en diferentes series de ERP fueron testados y analizados. A modo ilustrativo, las figuras 3.2a y 3.2b muestran el caso particular de un modelo de FCN que fue calculado con un tamaño de ventana correspondiente a 2 ciclos del FCN y con un desplazamiento de medio año entre ajuste y ajuste. Después de eliminar el efecto del FCN de $dX$ y $dY$ (figuras 3.2c y 3.2d) utilizando todos los modelos estimados, se calculó la desviación estándar de los residuales (figura 3.3c) con el fin de averiguar qué parámetros $N_L$ y $N_D$ se ajustaban mejor a las fluctuaciones producidas por el FCN. De los resultados se deduce que los modelos más precisos fueron los calculados con pequeños valores $N_L$, siendo la serie de ERP USNO Finals la que produce una menor dispersión en la solución final. Los errores se ven reducidos un ocho por ciento al eliminar las sesiones comprendidas en los años 1984-1990.

#### 0.3.3.2 **Amplitud y fase**

Una vez analizados los errores, mediante la ecuación 3.2 se pasó a estudiar la fase y amplitud del FCN que es percibida o captada por cada modelo, con el objetivo de intentar deducir

algún tipo de relación con los cambios geofísicos que suceden constantemente en la Tierra. De la figura 3.5 se concluye que cuanto más estrecha es la longitud de la ventana móvil, mayor es la sensibilidad a cualquier cambio geofísico, y viceversa. Es importante también resaltar que en el periodo comprendido entre 1990-2000 la amplitud se reduce casi hasta la mitad, mientras que en el periodo 2000-2013 este comportamiento es completamente opuesto, incrementando la amplitud.

#### 0.3.3.3 **Comparación con otros modelos**

Por último, todos nuestros modelos de FCN fueron comparados con:

- el modelo recientemente determinado por Krásná et al. [2013], calculado con grupos de datos de 4 años ($\approx$ 3.4 ciclos del FCN) desplazados 1 año.
- el modelo estimado por Lambert [2007], el cuál empleó una longitud de ventana móvil de 2 años ($\approx$ 1.7 ciclos del FCN) desplazada 1 año entre ajustes consecutivos.

La comparación con los citados modelos reveló que el mínimo WRMS localizado aproximadamente en 1.7 y 3.4 ciclos del FCN es completamente consistente con los grupos de datos que usaron Lambert y Krásná (figura 3.6), siendo este último modelo el que presenta una mayor concordancia (WRMS de 12 $\mu as$) con nuestras estimaciones, tal vez como consecuencia de la utilización del mismo software VLBI e idéntico periodo de FCN.

### 0.3.4 **Discusión**

La investigación abordada en este capítulo confirma que los modelos de FCN de alta resolución temporal son más sensibles a cualquier cambio geofísico e incrementan sustancialmente la precisión, alcanzando una mejora frente a los modelos convencionales cercana a 20 $\mu as$. Cabe destacar que los modelos de FCN estimados con diferentes series de ERP producen resultados muy similares, siendo la serie USNO Finals la que aporta las soluciones más precisas. Por último, identificar los fenómenos geofísicos que excitan el FCN, tales como las perturbaciones meteorológicas (variaciones del momento angular atmosférico, oceánico e hidrológico), supondría poder predecir y modelar estas nutaciones con modelos de mayor contenido analítico, ayudando de esta forma a alcanzar el objetivo de precisión perseguido por GGOS.

## 0.4 Capítulo 4

Cualquier cambio en el campo gravitatorio terrestre suele estar motivado por una redistribución de masa, especialmente agua, en la superficie de la tierra. Los mapas asociados a estas anomalıás de masa en superficie pueden ser medidas por la misión GRACE [Chao, 2005; Wahr et al., 1998]. Los datos de GRACE son proporcionados por tres organismos diferentes (GFZ, CSR y JPL) en forma de desarrollos mensuales de armónicos esféricos (SC, Coeficientes de Stokes, $C_{lm}$, $S_{lm}$), pero existe un problema técnico y los SC, según van aumentando en grado y orden, incrementan el contenido de ruido, lo que supone un impedimento para conseguir una alta resolución espacial. Esto obliga a filtrar los datos en SC para poder obtener las anomalías mensuales del geoide con una resolución adecuada. Hoy en día, no existen unas reglas generales para el filtrado, siendo los propios usuarios los que tienen que elegir la opción más conveniente a su juicio. El proceso de filtrado mayoritariamente utilizado consta de dos fases: (1) aplicar el filtro de decorrelación [Swenson and Wahr, 2006] y (2) posteriormente un filtro Gaussiano [Jekeli, 1981; Swenson and Wahr, 2002]. Dependiendo del estudio y de la versión de datos de que se disponga, estos filtros deben de ser nuevamente parametrizados. En otoño de 2012, una nueva versión de coeficientes de Stokes fue publicada por las tres agencias (RL05). Esta se caracteriza por ser una versión mejorada de su predecesora (RL04), siendo todavía un requisito indispensable filtrar los datos. La necesidad de tener actualizados los parámetros de los citados filtros para el RL05 es de vital importancia para la geodesía. Es por ello, que en este capítulo se ha revisado la metodología de filtrado de Swenson and Wahr [2006] con el objetivo de encontrar los parámetros que proporcionen los mínimos residuales (válidos para aplicaciones globales). El filtro Gaussiano y el filtro anisotrópico "Fan"[Zhang et al., 2009] también fueron investigados.

### 0.4.1 Descripción de los datos. Metodología

Para determinar los nuevos parámetros del filtro de decorrelación fueron utilizados los SC de las tres las agencias espaciales CSR, GFZ y JPL. El periodo de estudio estuvo comprendido entre enero de 2004 y diciembre de 2011. Debido a problemas técnicos de los satélites GRACE, los SC de los meses 2011/01 y 2011/06 no pudieron utilizarse en los cálculos. Después de aplicar la ecuación 4.1 a dichos datos, se obtuvo la variación de masa super-

ficial ($\sigma$) representada en mapas mensuales con una resolución de $1^\circ \times 1^\circ$ [Chao, 2005; Wahr et al., 1998].

Para un orden fijo $m$, los SC presentan importantes errores de correlación en los grados pares e impares $(l)$, ruido producido como consecuencia del muestreo de datos a lo largo de las órbitas polares de GRACE. Swenson and Wahr [2006] propuso un filtro de decorrelación para subsanar estas imprecisiones. El método consiste en que por cada grado par (impar), se elimina un polinomio de grado n ajustado a los SC adyacentes de grado par (impar) que define una ventana que va cambiando de tamaño. La anchura $\omega$ de dicha ventana, viene dada por la ecuación 4.2 [Duan et al., 2009] que depende de los parámetros $A, k, \gamma$ y $p$. De la figura 4.1 se deduce que la elección de unos u otros valores que pueden tomar estos parámetros nos llevará a distintos valores $\omega$, influyendo en el procesado de los datos de GRACE. La ventana óptima será la que mejor se ajuste a la distribución de los errores de los SC (figura 4.2). Aplicando este criterio, se pudo fijar fácilmente los parámetros $\gamma = 0.04$ y $p = 3.4$. La elección del resto de parámetros no fue tan sencilla. Para ello, los datos de GRACE, junto con unos SC sintéticos que fueron creados para simular datos de GRACE libres de cualquier tipo de ruido, fueron filtrados probando una gran variedad de parametrizaciones: $A$ fue testado de 10 a 24; $k$ de 20 a 44 y $l$ de 10 a 45. Este último parámetro delimita la región de los SC que se quedaron sin filtrar. Es importante destacar que el filtro de decorrelación no suele aplicarse a los SC de bajo grado y orden debido al escaso ruido que presentan. Para el RL02, Chen et al. [2007] dejó sin filtrar los SC de grado y orden menor que 7. Para el RL05 está región se vió ampliada considerablemente a consecuencia de la mejor calidad de los datos. Groenlandia y la Antártida fueron excluidas del análisis.

### 0.4.2 Filtro de decorrelación

#### 0.4.2.1 Tendencias lineales

Filtros de decorrelación muy agresivos pueden producir una leve atenuación de la señal. Mientras que un filtrado débil puede provocar que los datos se vean afectados por algún tipo de señal no deseada. En resumen, el filtrado óptimo se encontrará localizado entre estos dos casos. En está sección repasamos la estrategía seguida por Duan et al. [2009] para hallar los parámetros del filtro de decorrelación que mejor se ajusten a los datos de GRACE del RL05.

Mediante el cálculo del rms (Root mean Square) de las tendencias lineales de los mapas de masa de superficie estimados con los datos de GRACE y datos sintéticos (ambos filtrados), se hizo una primera aproximación de los parámetros $A, k$ y $l$. Al normalizar este rms respecto al rms previo al filtrado (figura 4.3), se comprobó que el mayor rms se encontraba en los datos sintéticos, cosa completamente lógica ya que el filtro produce atenuación mayoritariamente en datos ruidosos y no en la señal. Por tanto, el filtro óptimo fue el que maximizó las diferencias del rms de las tendencias lineales entre los datos sintéticos y los datos de GRACE (figura 4.4). De estas diferencias se comprueba la importancia de elegir correctamente el parámetro $l$, alcanzando el mayor gradiente entre los grados 35 y 45. Por ejemplo, los datos CSR alcanzaron las mayores diferencias con $l = 38$ y $(A, k) = (24, 20)$. Para poder concretar más detenidamente la elección estos parámetros, fueron necesarios más estudios que son expuestos a continuación.

#### 0.4.2.2 GRACE vs. Datos sintéticos

Una serie de correcciones atmosféricas y oceánicas fueron aplicadas a los datos GRACE con el fin de poderlos comparar con los datos sintéticos de la forma más realista posible. Ya que el filtro de decorrelación no es capaz de reducir al máximo el ruido, fue necesario utilizar un filtro Gaussiano isotrópico de radio 500 km, definido en la ecuación 4.3. La única diferencia con respecto a la ecuación 4.1 es el término $W_{lr}$, parámetro que depende del grado $l$ y un radio $r$. Por cada punto del mapa de los datos GRACE (filtrados por decorrelación y por el filtro Gaussiano) se calculó el rms de las diferencias con respecto a los datos sintéticos sin filtrar. La figura 4.5 muestra la media espacial ponderada del rms para cada parametrización. Los mínimos errores fueron alcanzados entre $36 \leq l \leq 39$, $10 \leq A \leq 16$ y $20 \leq k \leq 28$. La máxima correlación con los datos sintéticos (figura 4.6) se dió con $38 \leq l \leq 39$, $A \sim 14$ y $20 \leq k \leq 28$ para los datos CSR y con $36 \leq l \leq 40$, $10 \leq A \leq 14$ y $20 \leq k \leq 28$ para los datos GFZ y JPL. Se puede comprobar que en ambos análisis el mínimo residual y la máxima correlación se alcanzan aproximadamente con los mismos valores (parámetros).

#### 0.4.2.3 Continentes vs. Océanos

En este análisis nos basamos en el criterio seguido por Chen et al. [2007]. La idea descansa en el hecho de que la variación de masa en superficie es mayor en continentes que

en océanos. De esta manera, si algún tipo de ruido fuera añadido a las SC, estos se transmitirían tanto en continentes como en océanos. Por eso, el filtro más adecuado fue el que consiguió maximizar la relación señal ruido entre continentes y océanos. La figura 4.9 exhibe esta relación para los diferentes filtros de decorrelación que fueron probados. El máximo ratio fue conseguido con valores que oscilan entre $38 \leq l \leq 43$, $14 \leq A \leq 16$ y cualquier $k$ para los datos CSR y con $38 \leq l \leq 41$, $12 \leq A \leq 14$ y cualquier $k$ para los datos GFZ y JPL.

### 0.4.3 Filtro Gaussiano vs Filtro Fan

En esta sección se profundizó en el filtro Gaussiano, ampliamente extendido en el uso de datos GRACE. Utilizando el filtro de decorrelación con los parámetros que mejor se ajustaban para los datos RL05, los SC se volvieron a filtrar de nuevo con distintos filtros Gaussianos (probando varios valores de r comprendidos entre 240 km a 520 km). Para este estudio se volvió a calcular el ratio de variabilidad entre continentes y océanos (figura 4.11). El máximo ratio, y por lo tanto el filtro óptimo, se alcanzó con valores de $r = 380$ km para los datos CSR, $r = 420$ km para el GFZ y $r = 400$ km para el JPL. Estos resultados se vieron superados al utilizar el filtro anisotrópico Fan (figura 4.13). A diferencia del Gaussiano, este filtro no depende solo del grado de los SC, sino que también lo hace del orden. Es decir, el filtro Fan combina dos filtros Gaussianos (ecuación 4.4) que son aplicados tanto al grado como al orden [Zhang et al., 2009]. Los radios que logran aumentar el ratio al máximo son con $(r_l, r_m) = (290, 690)$ km para la agencia CSR, $(r_l, r_m) = (310, 820)$ km para el centro GFZ y $(r_l, r_m) = (290, 640)$ km para el grupo JPL.

### 0.4.4 Discusión

Según los resultados del análisis estadístico llevado a cabo en este capítulo se deduce que: (1) el ruido que poseen los SC se distribuyen de la misma forma para las tres agencias; (2) la porción de SC que se deja sin filtrar es la parte más crítica en el proceso de filtrado; (3) los datos del RL05 son menos ruidosos que los de la versión anterior (RL04),se debe a ello que la porción de SC sin filtrar haya aumentado con estos nuevos datos; (4) la parametrización óptima para el filtro de decorrelación (válida para aplicaciones globales) usando los datos CSR, JPL y GFZ está próxima a $l = 38$, $A = 14$, $k = 24$, $\gamma = 0.04$ y $p = 3.4$. Con el fin de analizar el nivel de mejora, estos nuevos parámetros fueron comparados con los que se

venían utilizando anteriormente para aplicaciones oceánicas y continentales [Chambers and Bonin, 2012; Chen et al., 2007; Duan et al., 2009]. De los resultados de esta comparación (tablas 4.1 y 4.2) se concluye que, los nuevos parámetros sugeridos son los más adecuados para el RL05 e investigaciones a escala global.

## 0.5 Capítulo 5

Los geodestas están especializados en adquirir, analizar e interpretar cualquier tipo de medición espacial, aérea y terrestre, teniendo estos un papel determinante en intentar comprender el por qué de los cambios a los que continuamente está sometido nuestro planeta Tierra. El "Running Trend analysis" (RTA) es uno de los métodos más extendidos en investigaciones climáticas para analizar cualquier serie temporal univariante (con datos u observaciones individuales recogidos a intervalos iguales de tiempo, es decir, equidistantes los unos de los otros), así como para medir el grado de asociación entre series de distintas variables [Hamlington et al., 2014; 2013; Holgate and Woodworth, 2004; Palmer and McNeall, 2014; Santer et al., 2014]. RTA es un método dinámico que consiste en hacer regresiones lineales de un grupo de observaciones consecutivas de una serie temporal. Normalmente, la serie de tendencias generada (RT, Running Trends) es utilizada como un resumen estadístico de la serie original, pudiendo ser de gran provecho para posteriores estudios. Sin embargo, las interpretaciones que se derivan de este análisis no son tan sencillas como parecen. Por esto el principal objetivo de este capítulo ha sido intentar esclarecer las causas por las que en determinadas ocasiones este tipo de análisis puede llevar a incorrectas interpretaciones de sus resultados. En la sección 0.5.1 se expuso una fórmula recursiva con la que se demostró , con el ejemplo de la seción 0.5.2, que el uso de RTA como única herramienta estadístico-descriptiva puede llevar a suposiciones erróneas, por lo que se aconseja acompañar a estos resultados con análisis estadísticos complementarios que sean capaces de medir el correcto funcionamiento de esta técnica.

### 0.5.1 Principal resultado

Sea una serie temporal de $n$ puntos que se encuentran igualmente espaciados en el tiempo $(t_1, t_2, \ldots, t_n)$ y $\Delta$ el intervalo de tiempo transcurrido entre dos puntos consecutivos, el vector tiempo puede ser expresado como:

$$t_k = t_1 + k\Delta, \;\; k = 0, 1, \ldots, n-1.$$

L es un número entero positivo que puede oscilar entre $2 \leq L \leq n-1$.
$W_1, W_2, \ldots, W_{n-L+1}$ define las ventanas móviles de longitud $L\Delta$ que empiezan a desplazarse desde $t_1$ con un intervalo fijo $\Delta$.

$$W_j = \{t_j, t_{j+1}, \ldots, t_{j+L-1}\}, \;\; j = 1, 2, \ldots, N-L+1.$$

Cada ventana $W$ contiene exactamente $L$ de los $n$ puntos de la serie $t_1, t_2, ..., t_n$.
Dada una serie temporal cualquiera $\{y_t\} = (y_{t_1}, y_{t_2}, \ldots, y_{t_n})$, se ha definido la serie de RT asociada a $\{y_t\}$ como la serie $\{\hat{m}_j\} = (\hat{m}_1, \hat{m}_2, \ldots, \hat{m}_{n-L+1})$ que se calcula con la ecuación 5.1 por el método de mínimos cuadrados.

Partiendo de unos valores arbitrarios $m_1^\star, m_2^\star, \ldots, m_{n-L+1}^\star$ y utilizando la fórmula recursiva 1 es posible obtener el conjunto $S^*$ de todas las series temporales $\{y_t\} = (y_{t_1}, y_{t_2}, \ldots, y_{t_n})$, a las cuales les corresponden una serie de tendencias $\{\hat{m}_j\} = (\hat{m}_1, \hat{m}_2, \ldots, \hat{m}_{n-L+1})$ que son exactamente $m_1^\star, m_2^\star, \ldots, m_{n-L+1}^\star$. Cada uno de estos conjuntos es un espacio vectorial de dimensión $L-1$ (para más detalles ver el apéndice A.1).
Teniendo definido $m_1^\star, m_2^\star, \ldots, m_{n-L+1}^\star$, la metodología que se debe seguir para obtener los valores $\{y_t\} = (y_{t_1}, y_{t_2}, \ldots, y_{t_n})$ con estas mismas tendencias se describe con el siguiente proceso recursivo:

- Se deben de elegir aleatoriamente $(y_{t_{n-L+2}}, y_{t_{n-L+3}}, \ldots, y_{t_n})$ en $\mathbb{R}^{L-1}$,
- Una vez elegidos estos valores, $(y_{t_1}, y_{t_2}, \ldots, y_{t_{n-L+1}})$ puede ser estimado usando

$$y_{t_{n-L+1-j}} = \frac{1}{\tilde{t}_1}[c \cdot m_{n-L+1-j}^\star - \sum_{h=1}^{L-1} y_{t_{n-L+1-j+h}} \cdot \tilde{t}_h], \;\; j = 0, 1, \ldots, n-L \qquad (1)$$

donde $\tilde{t}_h = \Delta \cdot (\frac{2h-1-L}{2})$ y $c = \sum_{h=1}^{L} (\tilde{t}_h)^2$.

Es importante destacar que los métodos de estadística descriptiva pretenden caracterizar y resumir los datos originales con la menor distorsión o pérdida de información posible. En RTA, $L$ (longitud de la ventana móvil) es el parámetro más sensible a las causas previamente citadas, ya que cuanto más grande sea este, mayor será la reducción de datos,

Universitat d'Alacant
Universidad de Alicante

y por tanto, menor será la cantidad de información que las tendencias retienen de la serie temporal $\{y_t\}$.

### 0.5.2 Ejemplo

A modo ilustrativo, se expusieron múltiples ejemplos para justificar la relevancia de la fórmula recursiva expuesta en la sección anterior. Para ello, se eligieron aleatoriamente tres series de RT diferentes (tabla 5.1). Suponiendo que éstas fueron calculadas a partir de series temporales de 15 términos y utilizando una ventana móvil de tamaño $L = 5$ fue necesario fijar arbitrariamente L-1=4 valores, $(y_{t_{12}}, y_{t_{13}}, y_{t_{14}}, y_{t_{15}})$. Por cada serie de RT y utilizando las variables libres expuestas en la tabla 5.2, se obtuvieron cinco series temporales distintas (tabla 5.3) que compartían las mismas tendencias que la serie de RT (figuras 5.1,5.2 y 5.3).

### 0.5.3 Discusión y conclusión

De lo expuesto en la sección anterior se pudieron deducir importantes conclusiones. Se ha comprobado que distintas series temporales pueden compartir la misma serie de RT y que diferentes series de RT pueden provenir de datos prácticamente idénticos. Con lo que una fuerte o débil correlación entre diferentes series de RT, no implica con completa seguridad que haya o no asociación. Todo esto quedó probado al comparar algunas de las series temporales que se expusieron en la sección anterior:

- A pesar de que las series temporales (c) y (e) de la figura 5.1 muestran comportamientos o patrones completamente diferentes, sus respectivas series de RT muestran una fuerte asociación.

- Las series temporales (b) de las figuras 5.1,5.2 y 5.3 son muy similares, al contrario de lo que sucede con las series de RT (débil correlación).

Tolo lo expuesto en este capítulo ha probado que la utilización de RTA como única herramienta estadístico-descriptiva, proporciona una confusa descripción de los datos originales, teniendo que ser complementada necesariamente con algún otro tipo de medición estadística, como por ejemplo el R-square y el nivel de significación de la regresión lineal en cada ventana $W_j$.

Universitat d'Alacant
Universidad de Alicante

*The beginning is the most important part of the work.*

Plato

CHAPTER

# 1

# Introduction

Improving the accuracy of the Earth rotation modelling is a significant requirement for many purposes (applications in geodesy, geodynamics, astronomy, and space navigation), among them the need for improving our understanding and knowledge of the changing Earth. Knowledge of the Earth Orientation Parameters (EOP) provide the link between the International Terrestrial Reference Frames (ITRF) and the International Celestial Reference Frames (ICRF). Series of EOP are provided by several Analysis Centers. We emphasize those produced by the United States Naval Observatory (USNO) and by the International Earth Rotation and Reference System Service (IERS). The latter is the international institution responsible of Earth rotation monitoring and prediction and is also in charge of the realization and maintenance of the ICRF and ITRF with the assistance of other International Association of Geodesy (IAG) services. EOP are crucial for correctly executing the aforesaid frame transformations, affecting parameters such as satellite positions, station coordinates, gravitational acceleration vectors, and so on [Bradley et al., 2012]. The classic Earth rotation study considers the movements of the rotation axis as seen from the Earth and the Space separately (fig. 1.1). The five EOP are [Petit and Luzum, 2010]:

- Pole Coordinates ($x_p$, $y_p$): coordinates of the Celestial Intermediate Pole (CIP) with respect to the IERS Reference Pole in the International Terrestrial Reference System (ITRS).

- Celestial Pole Offsets ($dX$, $dY$): observed corrections to the conventional celestial pole needed to obtain the CIP. The conventional celestial pole position is defined by the IAU Precession and Nutation models.

- Earth rotation angle (ERA): angle measured along the intermediate equator of the CIP between the Terrestrial Intermediate Origin (TIO) and the Celestial Intermediate Origin (CIO). Variations in the rotational speed of the Earth and the consequent variations in the ERA are conveniently represented by UT1 Time differences $dUT1$. Universal Time (UT1) is defined by a conventionally adopted linear proportionality to the ERA.

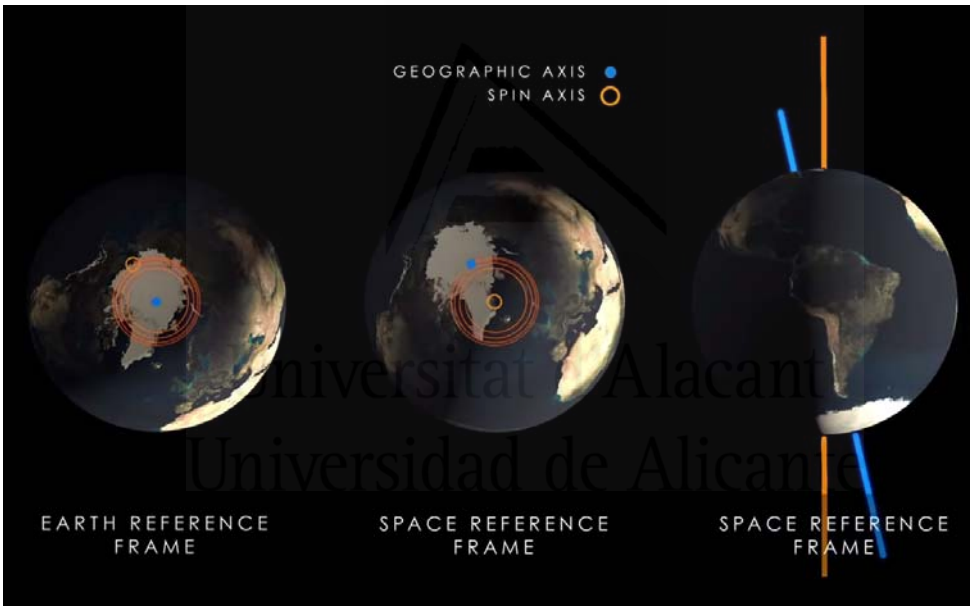


**Figure 1.1:** Earth rotation as viewed from the celestial and terrestrial reference frames. Cortesy of http://lupus.gsfc.nasa.gov/.

In the current IERS conventions the set of EOPs are defined as the arguments of the rotation matrices relating the Geocentric Celestial Reference System (GCRS) orientation to ITRS orientation. It is a three-dimensional rotation which is described by the precession/nutation $Q$, the Earth rotation $R$, and the polar motion $W$ matrices (see Petit and Luzum [2010]):

$$[GCRS] = Q(X, Y, s)R(-ERA)W(-s', x_p, y_p)[ITRS] \tag{1.1}$$

where the corrections angle $s'$ and $s$ locate the position of the TIO and CIO on the equator of the CIP, respectively.

ITRF and ICRF provide essential foundations for most Earth observations in the framework of the Global Geodetic Observing System (GGOS) of the IAG. They provide the universal standards to measure the Earth. Deficiencies in the accuracy of the ITRF and ICRF systems limit the quality of the geodetic observations which could be a primary limiting factor for understanding the Earth change. For intance, 1mm/year error in the secular translations of the origin of the reference frame w.r.t. the Earth System's center of mass could originate an error about 0.4 mm/year in mean global sea level variations [Kierulf and Plag, 2006]. Consequently, the availability of accurate, homogeneous, long-term stable global geodetic reference frames must be ensured as a mandatory framework, and as the metrological basis for Earth observation, in order that the geodetic "fingerprints" of climatic change can be monitored with the appropriate accuracy. This was clearly expressed in the statement from the IAG/GGOS at the Group on Earth Observations (GEO) X Plenary, held in Geneva in January 2014, concerning the Global Earth Observing System of Systems (GEOSS) implementation: "IAG is strongly committed to provide highly precise and stable geodetic reference frames and to promote the monitoring of global change signals. This refers for example to the gravity field and the rotation of the Earth and their variability".

Universitat d'Alacant
Universidad de Alicante

Very Long Baseline Interferometry (VLBI) is one of the most accurate ways to study, model, and control the EOP and references frames. VLBI is unique in its ability to define an inertial reference frame and to measure the Earth orientation in this frame since no other techniques can determine the 5 EOPs. This radio astronomy technique, fully operational for more than forty years, is extremely useful and indispensable for many geodetic applications such as sea level change, precise orbit determination for Global Navigation Satellite System, Earth mass exchanges, deep Space tracking, solar system exploration, etc. The basic and simple geometric concept of VLBI implicates at least two radio telescopes to measure the arrival time difference (time delay $\tau$) of a radio wavefront emitted by a distant quasar, which arrives on Earth as plane wavefronts [Schuh and Böhm, 2013]. The distance between the antennas, that observes the same source at same time, is known as baseline $\mathbf{b}$. Defining $\mathbf{s_0}$ as the direction to the radio source [Campbell, 2000] and baseline $\mathbf{b}$ as the vector from antenna 1 to antenna 2, the time delay can be computed readily as the scalar product (fig. 1.2):

$$\tau = -\frac{\mathbf{b} \cdot \mathbf{s_0}}{c} = t_2 - t_1 \tag{1.2}$$

After signal reception, the radio wavefront is recorded and time-tagged using the time and frequency of stable atomic clocks. Finally, the time delay $\tau$ is measured at the correlator for different centers. Moreover, the computed delay is affected for other significant contributions that must be accounted for and removed. Causes of these perturbations come from the diurnal aberration, mis-synchronization of the reference clocks at each observatory, troposphere, relativistic, ionosphere, cable and instrumental delays [Cannon, 1999].

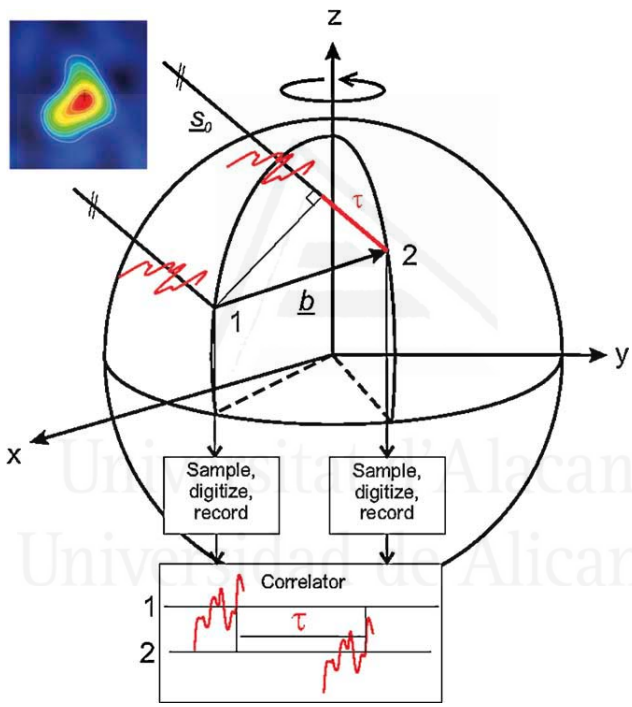


**Figure 1.2:** Basic principle for VLBI. From Schuh and Behrend [2012].

Inertial reference frame and precise positions of the antennas can be estimated using a large number of time difference measurements from many quasars distributed across the sky and observed with a global network of radio telescopes. From these delays and their precise estimates (few picoseconds), the baseline lengths and quasar positions can be computed with sub-centimeter accuracy and with a few milliarcseconds, respectively. The antennas being fixed to the ground, any change in the baseline lengths and in the angles from a series of measurements indicate regional deformation, tectonic plate motion, etc. So that Earth orientation variations can be estimated. The typical scenario for modeling these EOP

variations, in general for any geodetic measurement, is an iterative process as presented in fig. 1.3. The flow diagram can be formulated as two main streams. The principal steps are [Dehant et al., 2005; Schuh and Böhm, 2013]:

1. Observations, conventional models used in data analysis, and laboratory experiments are used to get knowledge on the celestial mechanics, models on the Earth interior, on atmosphere forcing, and tidal and non-tidal ocean forcing in order to infer new EOP models.

2. EOP models are applied to derive EOP predictions.

3. Predictions (computed) values are compared with the geodetic observations using least-square fit (Observed minus computed) to obtain residuals.

4. Finally, the residuals are studied and analyzed to deduce new constraints on the step 1 and 2.

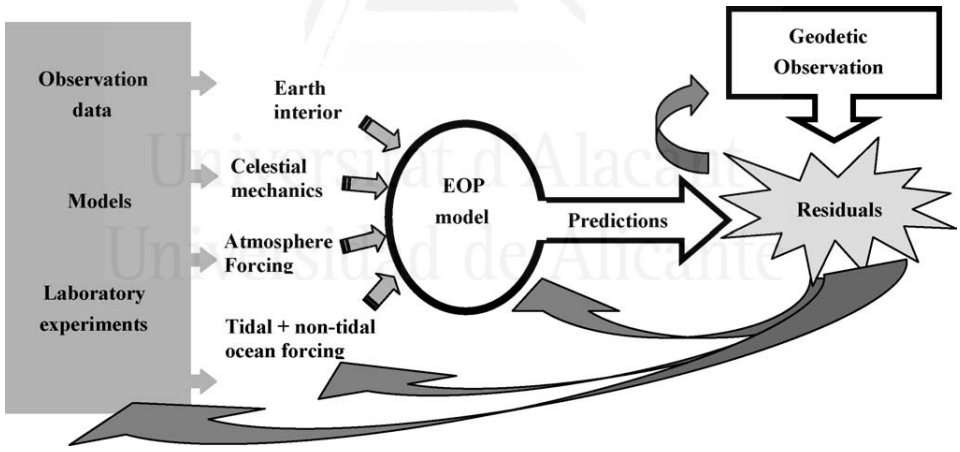


**Figure 1.3:** Scenario for typical geophysical investigations in particular in the frame of the EOP. From Dehant et al. [2005].

The legacy VLBI system preforms measurements at S band (2.2-2.4 GHz) and X band (8.2-8.95 GHz). The need to get more insight on the Earth system and on continuous monitoring of the EOP with a high temporal resolution (seven days per week), an upcoming VLBI system (VLBI2010) based on broadband delay is being developed [Petrachenko, 2009]. It is expected to be operational in the next several years. Further projects are in the proposal or planning stage, such as the New Atlantic Network of Geodynamical and

Space Stations (RAEGE) project. This VLBI network is being built between Spain and Portugal (Yebes, Canary Island, and Azores Island) and it is expected to be fully operational in the near future. The integration of RAEGE radio telescopes in the global VLBI network is expected to improve the geodetic observations. Each Geodetic Fundamental Station in RAEGE will be equipped with one radio telescope VLBI2010 (or VGOS, from VLBI GGOS) specifications (13.2 m diameter, able to operate in a four-band system that uses a broadband feed to span the entire frequency range from 2 to 14 GHz, fast slewing speed), one gravimeter, one permanent GNSS station and, at least at the Yebes site, one SLR facility [1]. Belda et al. [2014a] using simulated VLBI sessions planned with a new scheduling package [Sun et al., 2014] of Vienna VLBI Software (VieVS), that takes into consideration all present and future VLBI2010 specifications, checked the improvements in EOP and baseline length accuracies (fig.1.4). Mainly, the refinement and advance will be due to the large amount of observations and scans, small fast-moving antennas, and the new broadband frequency observations.

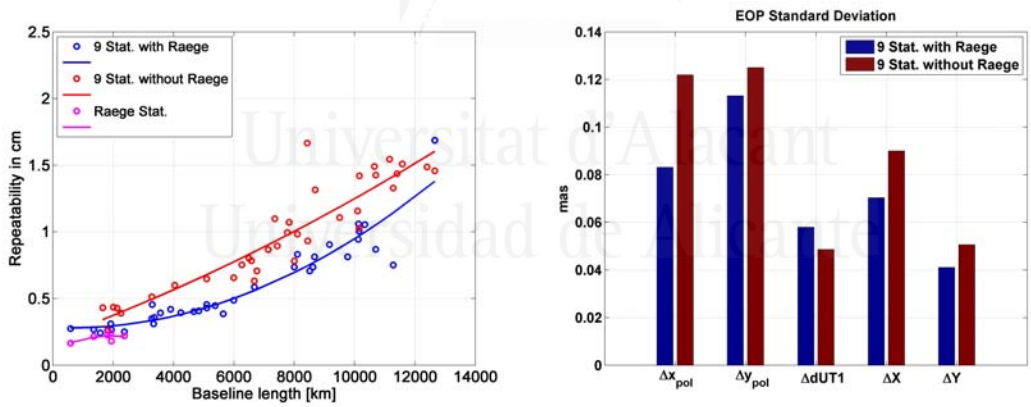


**Figure 1.4:** Improvements in EOP (right) and baseline (left) estimation using the future RAEGE network. From Belda et al. [2014a].

Global observations are necessary to characterize highly accurate spatial and temporal changes of the Earth system that relate to gravity field variations and Earth rotation changes. The Earth's gravity field depends on the mass distribution of the Earth. Therefore, any mass movements in, on or above the Earth produce variations in the gravity field. On the other hand, mass transport will change the Earth's inertia tensor, which affects the Earth rotation

[1] www.raege.net

according to the angular momentum laws. A better knowledge of these variations will provide information about the global changes and dynamic behaviour of the Earth [Chao, 1994]. The temporal variations in the gravity field allow thus the investigation of changes in the Earth's rotation. Vice versa, the investigation of EOP indicates mass movements in and on the Earth. Therefore a common analysis of gravity parameters and EOP may help to better understand the physical processes which cause these signals [Peters et al., 2002].

In summary, variations of Earth rotation are driven by mass redistribution and movements within the Earth System, including the solid Earth, atmosphere, ocean, hydrosphere, and cryosphere. Under the conservation of angular momentum, any variations of Atmospheric angular momentum (AAM), Oceanic angular momentum (OAM), Hydrological angular momentum (HAM) can change Earth's rotation via exchange of angular momentum between the solid Earth and its geophysical fluid envelope. At interannual or shorter (i.e. longer than 1-day) time scales, variations of atmospheric pressure and wind, Ocean Bottom Pressure (OBP) and currents, and Terrestrial Water Storage (TWS) change (plus ice mass change over polar ice sheets and mountain glaciers) are primary driving torques producing Earth rotational changes [Chen et al., 2012].

Two essential criteria for a given geophysical mass redistribution have to concur in order to be significant in its geodynamic effects [Chao, 1994]. A sufficiently large amount of mass has to be involved in the transport, and the effective net transport has to be over great distances. The behaviour of geophysical Earth rotation variations is governed by the angular momentum law, which can be expressed in the form of the Liouville equation [Moritz and Mueller, 1987] in the moving terrestrial reference frame:

$$\dot{H} + \omega \times H = L \tag{1.3}$$

where $\omega$ is the Earth angular velocity, $H$ is the Earth angular momentum, and vector $L$ on the right side denotes the external torques which are exerted by gravitational forces of Sun and Moon. $H$ can be conveniently separated into two parts:

$$H = I \cdot \omega + h \tag{1.4}$$

where $I$ is the inertia tensor of Earth and $h$ designates the relative angular momentum as seen in the terrestrial frame. From the previous equations we can see that in the absence of external torques one can change, or excite, the Earth rotation both in $\Delta LOD$ and polar

motion in two ways: changing $I$ by redistribution mass and changing $h$ by inducing relative motion [Chao, 1994]. The former is often called the mass term and the latter the motion term; together they yield the forcing or excitation function for Earth rotation. Since any mass redistribution is accompanied by mass motion, the two terms are, in principle, related by conservation of mass. It is worth to recall that $\omega$ and $h$ depend on the realization of the terrestrial frame in which the equations are written.

Nowadays, the duty of Geodesy is helping to the accurate modeling of all the physical processes, including ice melting, redistribution of continental water, sea level, postglacial rebound, atmospheric transport and oceanic circulation, luni-solar tides, mantle convection and tectonic movements in order to get better understanding of the causes and consequences that affect reference frames and produce variations in the EOP and their interactions with each sub-system (fig. 1.5).

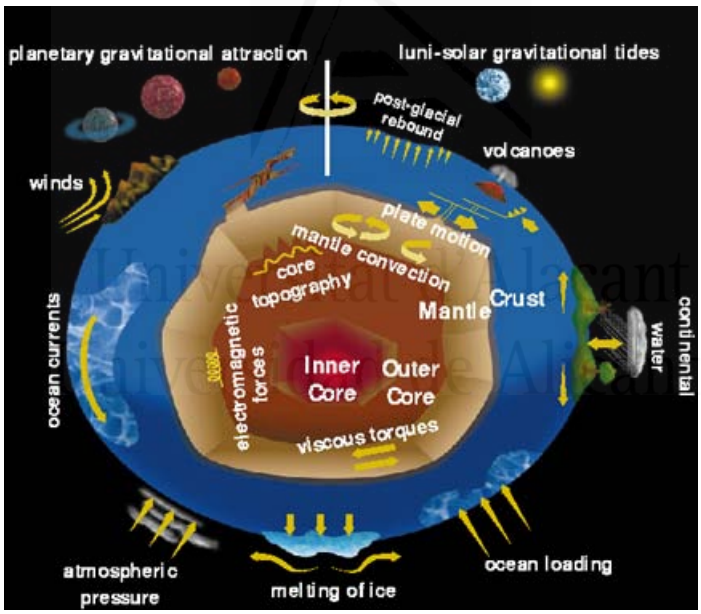


**Figure 1.5:** Schematic illustration of the forces that perturb the Earth's rotation. From http://bowie.gsfc.nasa.gov/ggfc/mantle.htm.

Another fact that perturbs the Earth orientation in the space is for example the different fluid layers. The Earth responds differently due to the presence of those fluid layers, the most significant example being the resonance in the nutation motion at the free core nutation (retrograde motion of the Earth figure axis with a period of about 430 days and an average amplitude of about 100 microarcseconds) caused by the different material characteristics

of the Earth core and the mantle. This causes the rotational axes of those layers to slightly diverge from each other, resulting in a wobble of the Earth rotation axis comparable to nutations. Due to this motion is thought to be not predictable (complex patterns) with theoretical models, precise empirical Free Core Nutation (FCN) models are required to complement the current IAU2000 nutation theory. Several models can be found in Krásná et al. [2013]; Lambert [2007]; Malkin [2010].

At the present time, the mass distribution and transfer of water is crucial for many scientists in understanding the evolution of our climate, which is related to mass changes in the Earth System. Advances in the gravity measurements with free-fall methods have reached accuracies of $10^{-9}g$, allowing the measurements of effects of mass changes in the Earth interior or the geophysical fluids [Blewitt et al., 2010]. These changes can also be detected as gravity variations and can be quantified on a global scale by three main satellite gravity missions so far:

- The first was Challenging Minisatellite Payload (CHAMP) launched in 2000 which was dedicated to infer the gravity variations from orbital perturbations measured with GPS and from a high-precision three axes accelerometer, besides studying the magnetic field and the atmosphere.

- The second is Gravity Recovery And Climate Experiment (GRACE), launched in 2002. This mission inherits the CHAMP techniques and measures the variations of the distance between two satellites at micron meter level accuracy using carrier phase measurements in the K(26 GHz) and Ka(GHz) frequencies to estimate series of monthly Stokes coefficients (SC) of a spherical harmonic representation to infer in variations of Earth's gravity (fig. 1.6) [Tapley et al., 2004].

- The most advanced gravity space mission is Gravity Field and Steady-State Ocean Circulation Explorer (GOCE), launched in 2009. It provides improved observations of Earth's gravity field than CHAMP and GRACE, both in terms of accuracy and spatial resolution, allowing a optimum determination of the global geoid. Additionally, GOCE provides gravity gradients, i.e. the second-order derivative of the gravitational potential of the Earth.

Universitat d'Alacant
Universidad de Alicante

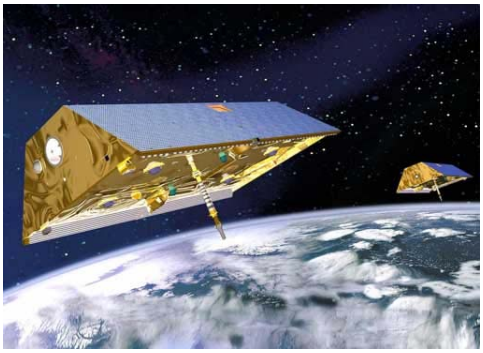

**Figure 1.6:** GRACE satellites. Source http://www.space-airbusds.com.

GRACE and GOCE make gravitational field observations that are sensitive to spatial and temporal variations in the Earth's mass distribution, and can be used to investigate time variations in the shape of the geoid that defines the sea surface in static equilibrium, in the Earth rotation, in ice-sheet volume, and in Sea Level Variation (SLV). In addition, these missions are not sensitive to the volumetric expansion or contraction induced by variations of the temperature and salinity of the sea water. As a result of this and accordingly to equation 1.5, such gravitational measurements with the aid of SLV observations ($SLV_{total}$) can be used to determine the change due to steric ($SLV_{steric}$) and mass contributions ($SLV_{mass}$), being extremely useful to evaluate the global warming covert in the oceans [Watts and Morantine, 1991].

Universitat d'Alacant
Universidad de Alicante

$$SLV_{total} = SLV_{steric} + SLV_{mass} \tag{1.5}$$

As noted earlier, there is a powerful connection among Earth rotation changes, gravity field variations and Sea Level variations. As consequence of this relevant association, the following chapters in this dissertation aim at extending the knowledge to a greater or lesser extent on these three different but connected topics, which in turn are closely linked to the essential three pillars of Geodesy: the rotation of the Earth, gravity field, and geometry (fig. 1.7). Those pillars provide the basis for the realization of the reference systems required to assign time-dependent coordinates to points and object, and to describe the Earth's motion in space. In Chapter 2, the consistency and long-term stability of the current conventional celestial and terrestrial reference frames and the conventional EOP series have been assessed. In chapter 3, a new empirical FCN model based on the analysis of VLBI sessions is performed. In chapter 4, the filtering processing for global applications of the

newly released GRACE data has been updated, optimized and improved. In last chapter 5, a cautionary note on the use of running trends as summary statistics for univariate time series and time series association is presented, being a useful tool in order to avoid misleading interpretations in any climatic and geodetic measurements (e.g. SLV). All these tasks are carried out in order to get more insight into the attainability of the accuracy and stability goals pursued by the GGOS of the IAG (1 $mm$ position and 0.1 $mm/year$ in velocity on global scales for the ITRF [Plag and Pearlman, 2009]) and besides achieving a more precise knowledge about the Earth change. A detailed overview on each chapter is shown.

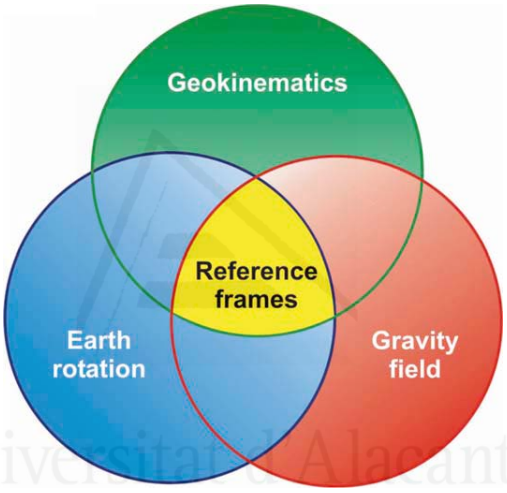


**Figure 1.7:** The three pillars of geodesy provide the reference frames. From Plag and Pearlman [2009].

Different realizations of ITRF (based on VLBI, SLR, GNSS and DORIS techniques) and ICRF (based on VLBI) might cause a slow degradation of the consistency between them (differences in geometry, orientation and scale). Besides, the IERS 08 C04 EOP series are not perfectly aligned to the ITRF and ICRF since they are often referred to different terrestrial and celestial frames, resulting in small inconsistency of the EOP series with respect to the ITRF and ICRF. In chapter 2 according to the aforementioned problems, we empirically assess the consistency among the conventional celestial and terrestrial reference frames and EOP by analyzing 30 years of VLBI sessions. We compare the EOP determined using the same VLBI data by fixing on different TRFs. A complication for the assessment is that the frames are global parameters, while the EOP are determined as local parameters. The effect of unmodelled geophysical signals (i.e. non-linear station mo-

tion) in the regularized coordinates and the sensitivity with respect to different a priori EOP and celestial reference frames is assessed too. We conclude that unmodelled geophysical signals partly affect the IERS 08 C04 EOP series. There are small but not negligible inconsistencies between the conventional celestial reference frame, ICRF2, the ITRF2008 and the conventional EOP that are quantified by comparing VTRF2008 and ITRF2008.

In chapter 3 we report on the progress of the derivation of a new empirical model of FCN based on the analysis of VLBI observations performed with the VieVS package. To obtain a detailed quantitative assessment of the time-variable amplitude, we proceed to conduct multiple sliding window analysis. The method can be seen as an extension of the recent work on FCN by Krásná et al. [2013]. Results have been compared to that model and Lambert [2007], which is the model recommended in the IERS Conventions 2010 [Ma et al., 2009]. The level of agreement is satisfactory but our new model give rise to a noticeable lower Weighted Root Mean Square (WRMS) of residuals along the whole period of VLBI observations according to our computations. Further tests and comparisons with different a priori Earth Rotation Parameters (ERP) series are carried out, concluding that USNO finals performs better than IERS 08 C04 series in our analysis.

Monthly GRACE global gravity solutions are provided by three GRACE data processing centers. GRACE temporal solutions are generally expressed in the form of spherical harmonic coefficients ($C_{lm}$, $S_{lm}$) of the geoid up to a given degree $n$ and order $m$ [Heiskanen and Moritz, 1967]. Two kinds of errors appear in these GRACE monthly solutions [Cazenave and Chen, 2010; Chambers, 2006]: (1) errors introduced by data processing (correlated errors due to unmodeled effects and contamination of other geophysical signals) and (2) post-processing errors (leakage due to signal contamination from regions outside the studied area and spatial smoothing for removing high-frequency noise). In autumn 2012, the new Release 05 (RL05) of monthly geopotencial spherical harmonics SC from GRACE mission was published. This release reduces the noise in high degree and order SC, but they still need to be filtered. One of the most common filtering processing is the combination of decorrelation [Swenson and Wahr, 2006] and Gaussian filters [Jekeli, 1981]. Both of them are parameters dependent and must be tuned by the users. Previous studies have analyzed the parameters choice for the RL05 GRACE data for oceanic applications, and for Release 04 (RL04) data for global application. Chapter 4 updates the latter for RL05 data extending the statistics analysis. The choice of the parameters of the decorrelation filter has been optimized to: (1) balance the noise reduction and the geophysical

Universitat d'Alacant
Universidad de Alicante

signal attenuation produced by the filtering process; (2) minimize the differences between GRACE and model-based data and (3) maximize the ratio of variability between continents and oceans. The Gaussian filter has been optimized following the latter criteria. Besides, an anisotropic filter, the fan filter [Zhang et al., 2009], has been analyzed as an alternative to the Gauss filter, producing better statistics.

Geodesists are specialized in acquiring, analyzing, and interpreting space-based, ground-based, and airborne geodetic measurements that are essential for a better understanding of the full Earth System. In consequence, the treatment of data plays a significant role to draw significant and real conclusions about the Earth changes. Due to its special relevance, in chapter 5, one of several methods widely used in climate research to analyze univariate time series and time series association is studied. It is the Running Trend Analysis (RTA). Given a time series of length $n$, Running Trend Analysis involves evaluating least-square trends over overlapping time windows of $L$ consecutive time points, with overlap by all but one observation. This produces a new series called running trends series. RTA could be a valuable descriptive tool as summary statistics for time series and time series associations, often as a part of more complex studies. However, its general use and interpretation in applied research is unclear. This is why the goal of this chapter is to clarify such an interpretation. An explicit formula is provided to show that RTA, alone, performs very poorly as summary statistics for time series. The use of complementary statistics that can measure the performance of RTA is advocated both for a proper interpretation of RTA and for the optimal choice of its parameter, the common length of the overlapping windows.

Universitat d'Alacant
Universidad de Alicante

## Supporting Publications

The publications listed below are the scientific works which have been carried out in this Ph.D. project.

- Related to Chapter 2

**Belda, S.**, R. Heinkelmann, T. Nilsson, B. Soja, M. Karbon, J. Anderson, L. Liu, C. Lu, J.A. Mora-Diaz, V. Raposo-Pulido, M. Xu, José M. Ferrándiz, and H. Schuh, 2014: Reference frame induced long-term effects on EOP. Geodaetische Woche 2014.

Heinkelmann R., **S. Belda**, José M. Ferrándiz, and H. Schuh H, 2014: The consistency of the current conventional Celestial and Terrestrial Reference Frames and the conventional EOP series. Journ. 2014 Systémes de reference spatio-temporels. In print.

Heinkelmann R., **S. Belda**, José M. Ferrándiz, and H. Schuh, 2014: How consistent are the current conventional Celestial and Terrestrial Reference Frames and the conventional Earth orientation parameters? IAG Symp. Series REFAG 2014 proc. In review.

**Belda S.**, R. Heinkelmann , José M. Ferrándiz, T. Nilsson, and H. Schuh, 2015: On the consistency of the current conventional EOP series and the celestial and terrestrial reference frames. Journal of Geodesy. In review.

Universitat d'Alacant
Universidad de Alicante

- Related to Chapter 3

**Belda S.**, R. Heinkelmann, José M. Ferrándiz, T. Nilsson, and H. Schuh, 2015: A new empirical model for Free Core Nutation. EGU General Assembly. Vol. 17, EGU2015-11088. Geophysical Research Abstracts.

- Related to Chapter 4

**Belda S.**, D. García-García, and José M. Ferrándiz, 2014: On the decorrelation filtering of RL05 GRACE data for global applications. Geophysical Journal International. doi:10.1093/gji/ggu386.

- Related to Chapter 5

Trottini M., I. Vigo, and **S. Belda**, 2015: On the Use of Running Trends as Summary Statistics for Univariate Time Series and Time Series Association. Journal of Climate. doi: 10.1175/JCLI-D-15-0009.1.

*Personally, I think it does help, that it makes a beneficial difference, but the scientific literature on the subject is very messy.*

Jeanne Petrek

CHAPTER

2

# On the consistency of the current conventional EOP series and the Celestial and Terrestrial Reference Frames

Universitat d'Alacant
Universidad de Alicante

## 2.1 Introduction

[1]Assessing the actual accuracy of the EOP is still an open and timely question, into which we need more insight in view of the demanding requirements of accuracy and stability pursued at present by, e.g. the GGOS of the IAG. EOP are currently officially realized by the time series IERS 08 C04 provided by the IERS, which is also in charge of the realization of the conventional ITRF and ICRF. The conventional EOP are the EOP that refer the realization of ITRS, currently ITRF2008 [Altamimi et al., 2011], to the realization of International Celestial Reference System (ICRS), currently ICRF2 [Fey et al., 2004]. The computation of those EOP series that provide the time-varying relative orientation of ICRF and ITRF depends on a complex process, in which the solutions produced by various techniques and by various Analysis Centers (AC) are combined. In such a way

[1]Chapter submitted to Journal of Geodesy

both the IERS 08 C04 series and the ITRF2008 depend on the combination strategy. The actual (not the assumed) accuracy of the current conventional EOP becomes thus a question tightly linked to the previous issue of the level of consistency of that IERS 08 C04 series and ITRF2008 and ICRF2 (the current IERS realizations of the terrestrial and celestial reference systems used in the determination of IERS 08 C04).

The objective of this chapter is presenting the results of some experiments aimed at getting more insight into the issue of the mutual consistency of the time series IERS 08 C04 and ITRF2008 and ICRF2 as well. To do this, various consistency studies are carried out based on VLBI data analyses. When the aforementioned products (IERS 08 C04, ITRF2008, and ICRF2) are evaluated using VLBI data only, it should be mentioned that the assessment will show the inconsistency among the products with respect to VLBI data. In Section 2.4, we first present the results of an experiment designed to assess the effect of unmodeled geophysical signals on the EOP series. Next, the sensitivity of the VLBI EOP solutions to the change of the a priori EOP series is addressed. Then, some TRF and CRF realizations (distinct to those used in the IERS 08 C04 derivation) are tested to study their impact on the EOP, especially on the long-term. Finally, global rotations (from similarity transformations) among the previously used frames are determined and compared with the differences between the associated ERP determined for each frame selection.

Universitat d'Alacant
Universidad de Alicante

## 2.2 Consistency among reference frames and EOP. General aspects

The EOP that are consistently determined with ITRF2008, IERS 08 C04, are pole coordinate offsets and their derivatives as well as universal time with respect to atomic time (UT1-UTC) and Length of day (LOD). The current IERS procedure for ITRF combination omits the celestial pole offsets reported in VLBI SINEX files, i.e. the combined EOP are inconsistent to the celestial pole offsets and disconnected from ICRF. The orientation of the VLBI ground network that refers to ICRF via the VLBI EOP is allowed to rotate during the combination. Consequently, the IERS 08 C04 do not refer to ICRF but to an unknown celestial orientation somewhere between ICRF and the satellite orbit frames of the involved satellite techniques: Doppler Orbitography Integrated by Satellite (DORIS), Global Navigation Satellite Systems (GNSS), and Satellite Laser Ranging (SLR). Concluding, the IERS 08 C04 cannot be considered conventional.

Strictly speaking, the consistency resulting from the combination process could be claimed only for ERP, not for EOP. The International GNSS Service (IGS) solution contributes to ERP about $95\%$, but not to EOP since we can argue that IGS contributes $0\%$ to $dX$, $dY$, thus it is difficult to get full (or rigorous) consistency in the usual meaning of that concept. Besides, the satellite-based techniques and solutions might be inconsistent at a different level, since the Precise Orbit Determination (POD) methods and associated/included geophysical models or certain parameters are not identical for the various techniques or analysis centres. Rigorous consistency is still only a goal, not a fact, at the GGOS level of accuracy.

Some problems arise when assessing the consistency of EOP (time series of local parameters) with respect to reference frames (global parameters, such as constant angles or positions and linear velocities or piece-wise linear models).

First problem: the EOP determined together with global coordinates are consistent with the global coordinates and hence they are not necessarily consistent with the local coordinates. If station positions are adjusted locally, i.e. on the session level, the EOP referring to one session and the EOP referring to another session do not exactly refer to the same coordinates and hence are not consistent. Consequently, those EOP cannot be coherently interpreted because they do not refer to a common reference frame. IERS 08 C04 is an EOP series that is consistent with global coordinates (ITRF2008) and consequently the Root Mean Square (rms) of EOP w.r.t. IERS 08 C04 is smaller if station positions are fixed on ITRF2008 coordinates instead of locally estimated (table 2.3).

The second problem evolves from the misfit of the true coordinates and the simple coordinates model used for its approximation. For each station in the current terrestrial reference frame a constant position and a linear velocity are modelled while a number of non-linear station position variations are corrected for at the observation level prior to the adjustment. However, since not all non-linear effects are removed in advance, the uncorrected non-linear station displacements will propagate into EOP. Those EOP consistently refer to one reference frame but include neglected station displacements that vary with time. This is the case for IERS 08 C04.

Universitat d'Alacant
Universidad de Alicante

## 2.3 Data analysis

The consistency issues are assessed by performing different VLBI data analyses, which are extended to sessions ranging from 1984-07-09 until 2013-12-31 (GeoForschungsZentrum (GFZ) VLBI contribution to ITRF2013) [Heinkelmann et al., 2014c]. The GFZ version of VieVS [Böhm et al., 2012], VieVS@GFZ, was utilized, with the following common processing options: for each EOP one offset per day with respect to a selected a priori series (usually IERS 08 C04) was estimated for each VLBI session. For the modelling of the tropospheric delays we used the Vienna mapping functions (VMF1) [Böhm et al., 2006], and we estimated the zenith wet delays and the tropospheric gradients as piece-wise linear functions with 1 and 6 h interval lengths, respectively. The station clock offsets were estimated as piece-wise linear functions with 1-h interval lengths, plus quadratic terms [Nilsson et al., 2014]. After single-session adjustments, we discarded the VLBI sessions with a posteriori sigma of unit weight larger than 3.

Other processing options depend on the different analyses that have been performed and will be explained in detail in the corresponding sections. For instance, when we intended to determine the effect of a specific TRF or CRF on the EOP we fixed the station and source coordinates on their catalogue values. Thus, various EOP series were determined using different celestial (table 2.1) and terrestrial (table 2.2) reference frames for computing each solution and varying the a priori EOP series (IERS 08 C04, USNO finals and IAU 2006/2000A precession-nutation models).

In general, in order to compare the different pairs of EOP time series estimates, we calculated the Weighted Mean (WM) and the WRMS differences between each of them, by means of the following formulae [Nilsson et al., 2014], where sub-indices EOP1, EOP2 denote the individual solution:

$$
\begin{aligned}
WM &= \frac{\sum_{i=1}^{N} \frac{\widetilde{X}_{EOP1,i} - \widetilde{X}_{EOP2,i}}{\sigma^2_{EOP1,i} + \sigma^2_{EOP2,i}}}{\sum_{i=1}^{N} \frac{1}{\sigma^2_{EOP1,i} + \sigma^2_{EOP2,i}}} \\
WRMS &= \sqrt{\frac{\sum_{i=1}^{N} \frac{(\widetilde{X}_{EOP1,i} - \widetilde{X}_{EOP2,i} - WM)^2}{\sigma^2_{EOP1,i} + \sigma^2_{EOP2,i}}}{\sum_{i=1}^{N} \frac{1}{\sigma^2_{EOP1,i} + \sigma^2_{EOP2,i}}}}
\end{aligned}
\tag{2.1}
$$

Here, $\widetilde{X}$ denote the estimates of EOP values from VLBI analysis using the different settings, and $\sigma$ indicate their respective formal uncertainties. Moreover, when analyzing the residuals between a pair of different EOP solutions, a linear trend was subtracted, made of a shift (referred to epoch J2000.0) and a linear drift calculated by Least Squares (LS).

| **CRF** | **Reference** | **Comment** |
|---|---|---|
| ICRF-Ext.2 | Ma et al. [1998]<br>Fey et al. [2004] | Orientation is based on data until 1995.5 |
| ICRF2 | Ma et al. [2009] | Data until 2009 |

**Table 2.1:** Different CRFs used in this study.

| **TRF** | **Reference** | **Comment** |
|---|---|---|
| ITRF2000 | Altamimi et al. [2002] | Data until 2000 |
| ITRF2005 | Altamimi et al. [2007] | Data until 2005 |
| ITRF2008 | Altamimi et al. [2011] | Data until 2008 |
| VTRF2008 | Böckmann et al. [2010] | Data until 2008, VLBI-only frame, contains the same VLBI data as it was provided to ITRF2008 and DTRF2008 |
| DTRF2008 | Böckmann et al. [2010] | Data until 2008, contains the same data as ITRF2008, different combination approach |

Universitat d'Alacant
Universidad de Alicante

**Table 2.2:** Different TRFs used in this study.

## 2.4 Results

### 2.4.1 Unmodeled geophysical signals

The first analysis is concerned with the effect of the unmodeled geophysical signals affecting the position of VLBI stations. Let us notice that unmodeled is used in the proper sense of a component of a signal not accounted in a given model adopted in the processing strategy, it should not be understood necessarily as a deficiency of a conventional model. Let us recall that the determined station coordinates do not have a simple dependency on geophysical signals, since several models recommended in the IERS Conventions (i.e. solid Earth tides, oceanic and atmospheric tidal loading) are applied as a priori models in various data analyses, including the TRF estimation. However, other geophysical effects (i.e. non-tidal atmosphere, non-tidal ocean, and hydrological loading) are not recommended for conventional analyses; their effect on the results is accumulated together with the inaccuracies of the considered a priori models. Besides, the adopted model for the station coordinates is linear, made up of a position and a constant velocity. The logical consequence of all that is that appearance of unmodeled geophysical signals may broadcast into inaccuracies of the EOP. For these model limitations and to avoid damaging effects, fixing station coordinates to their a priori values is not recommended by the scientific community in general, and in particular when estimating EOP. In this section, we assess the uncertainty and stability attributable to unmodeled geophysical signals in the regularized station coordinates reported in the ITRF2008 by estimating the EOP through two different approaches:

a. Fixed ITRF2008 coordinates (unmodeled geophysical signals propagate into EOP)

b. Free (adjusted) ITRF2008 coordinates (unmodeled geophysical signals cause adjustment of station coordinates)

For the numerical assessment, we compare the resulting EOP series (approach a vs. b) to quantify how important the effects of the unmodeled geophysical signals are. The first global indicators of the differences are provided by the mean and the dispersion of the differences of the series computed for each EOP. Figure 2.1 displays the WM and WRMS differences between the two solutions and table 2.3 shows the shifts and drifts of the EOP differences w.r.t. IERS 08 C04 and the correlation among the two approaches. Fixation of the station positions at their nominal values in the ITRF2008 catalog causes insignificant

WM differences of all EOP; however it generates noticeable scatter, that reaches about 140 $\mu as$, 160 $\mu as$ and 85 $\mu as$ for $x_{pol}$, $y_{pol}$ and $dUT1$ respectively (figure 2.1).

| EOP | ITRF2008 Fixed | | | ITRF2008 Free | | | Fixed vs Free |
|---|---|---|---|---|---|---|---|
| | shift | drift | wrms | shift | drift | wrms | correlation |
| $\Delta x_{pol}(\mu as)$ | -17.4 $\pm$ 10.8 | -2.5 $\pm$ 0.5 | 130.0 | -28.2 $\pm$ 14.1 | -2.5 $\pm$ 0.5 | 175 | 0.49 |
| $\Delta y_{pol}(\mu as)$ | -0.6 $\pm$ 9.5 | 1.2 $\pm$ 0.4 | 122.1 | -34.1 $\pm$ 14.9 | 4.1 $\pm$ 0.5 | 183.1 | 0.44 |
| $\Delta dUT1(\mu s)$ | 5.7 $\pm$ 0.6 | -0.2 $\pm$ 0.03 | 8.1 | 6.0 $\pm$ 0.8 | -0.2 $\pm$ 0.03 | 10.1 | 0.61 |
| $\Delta X(\mu as)$ | -1.2 $\pm$ 5.6 | 0.6 $\pm$ 0.2 | 78.1 | 0.7 $\pm$ 5.8 | 0.4 $\pm$ 0.2 | 78.9 | 0.95 |
| $\Delta Y(\mu as)$ | 14.5 $\pm$ 5.8 | -3.2 $\pm$ 0.2 | 79.4 | 15.2 $\pm$ 5.9 | -3.3 $\pm$ 0.2 | 80.1 | 0.94 |

**Table 2.3:** EOP residuals ($\mu as$ or $\mu s$ for UT1) w.r.t. IERS 08 C04 between solutions using fixed and free ITRF2008 coordinates for the compution of EOP. Shift (referred to epoch J2000.0) and linear trend ($yr^{-1}$) are estimated by Weighted LS. Correlation coefficients between both series are also shown.

CIP coordinates are insignificantly affected by unmodeled signals: the CIP offsets correlation coefficients between solutions following approach a and approach b are very large (0.95, 0.94) and their WRMS are not significantly affected by the approach (table 2.3). However, we notice a small shift and a drift at the level of 3 $\mu as/yr$ at CIP coordinate $Y$ in both approaches.

Universitat d'Alacant
Universidad de Alicante

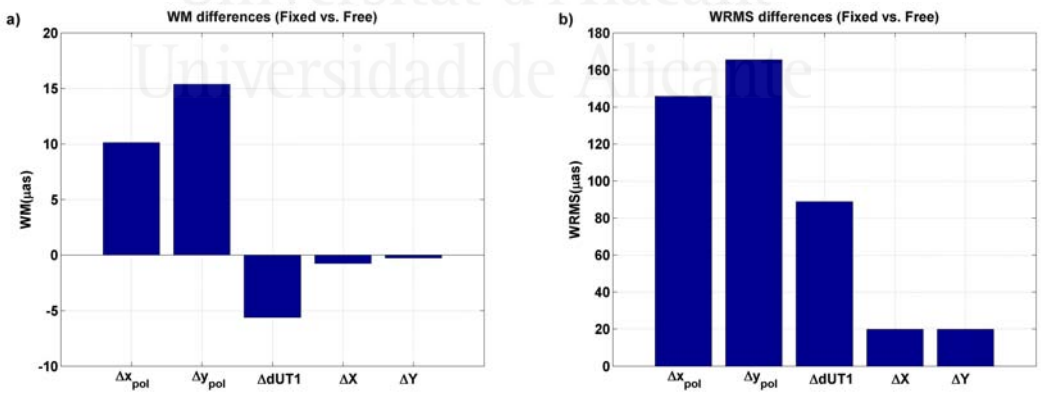


**Figure 2.1:** (a) WM and (b) WRMS differences between EOP estimated using fixed and free ITRF2008 coordinates.

Concerning table 2.3 it is important to note that the different handling of the Terrestrial Reference Frame (TRF) results in a strong decrease of the correlation of the ERP close to 50 per cent, which is consistent with the large values of the WRMS shown in figure

2.1b. The WRMS (weighted root mean square after subtracting the linear component of the difference) of the ERP significantly increase from the fixed to the free approach; our explanation for this is that the IERS 08 C04 EOP are consistent with the linear station model of ITRF2008 and consequently, if station coordinates differ from the catalogue value, the EOP scatter will increase.

### 2.4.2 **Different a priori EOP series**

In a situation in which convenient hypothesis ensuring that the iterations performed by the approximation algorithm converge to a unique solution would hold, the result should be independent on the starting a priori solution. However, the highly accurate estimation of the full set of EOP is not simple from either a mathematical or physical perspective, and the possibility of having effects derived from the choice of the initial solution should not be discarded without some verification. In this test, several a priori EOP series were used to estimate the EOP by VLBI from the current conventional TRF and CRF. First, VLBI time series were determined using a priori EOP from IERS 08 C04 (case 1), second, the a priori ERP and Celestial Pole Coordinates taken from IERS 08 C04 and from the IAU 2006/2000A precession-nutation model, respectively (case 2), and finally the USNO Finals time series were used as a priori EOP values (case 3). The comparison (figure 2.2) shows insignificant EOP WM differences between the IERS 08 C04 and USNO Finals approaches (cases 3 vs 1) whereas their repeatabilities (measured by the WRMS) are close to 40 $\mu as$ in all the EOP with the exception of $dUT1$ that is around 80 $\mu as$. EOP residuals reveal almost negligible and insignificant shifts and drifts (table 2.4). Therefore, VLBI-determined EOP using either IERS 08 C04 or USNO Finals as a priori values are in very good agreement, as expected.

The interpretation of the differences between cases 1 and 2 is not so simple. First, the WM differences of the Polar Motion (PM) parameters and UT1 are insignificant, as it could be expected since the a priori values for the three ERP were not changed. As for the WRMS values, in contrast to the precedent case they are about 20 $\mu as$ for both PM components and smaller for UT1. The differences between the celestial pole offsets are much more significant as expected since they correspond roughly to the deviation between the conventional nutation theory and the operational solution. It is known that the IAU adopted precession/nutation model, currently IAU 2006/2000A [Dehant, 2002; Hilton et al., 2006], contains only the easier to predict, forced astronomical effects, and thus, the FCN is not

included. This has a significant impact on the residuals - apart from the need of some additional corrections. Besides WRMS over 160 $\mu as$, we detect significant WM differences (55 $\mu as$ in dX and -93 $\mu as$ in dY) (figure 2.2) and large shifts (-41.7 in dX and 94.7 in dY) (table 2.4) on the CIP coordinates between the IERS 08 C04 and IAU 2006/2000A approaches are found, showing considerable scattering. The importance of using a good FCN model to get smaller residuals is well known. Due to the relevance and complexity of the FCN as well as the present availability of several empirical models [Krásná et al., 2013; Lambert, 2007; Malkin, 2010; 2013; VondraK and Ron, 2014], this specific topic is addressed in a separate forthcoming chapter.

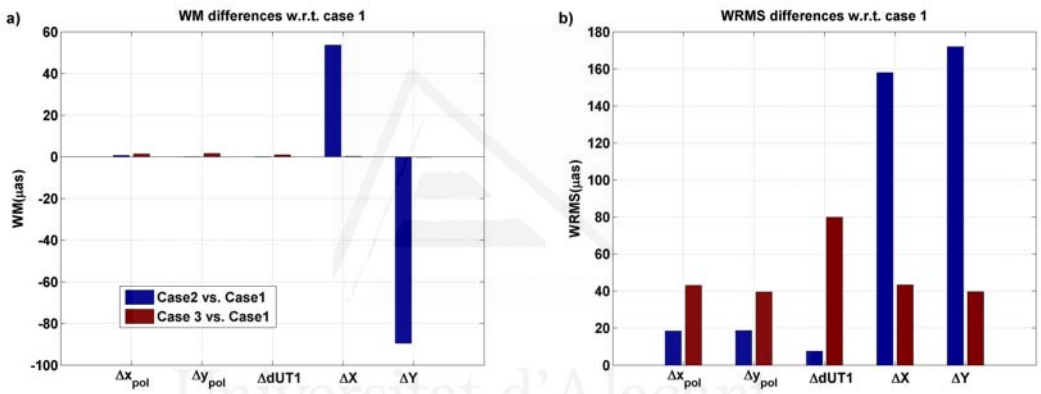


**Figure 2.2:** (a) WM and (b) WRMS differences between EOP estimated with different a priori EOP. Case 1: EOP IERS 08 C04. Case 2: ERP IERS 08 C04 and X,Y IAU 2006/2000A. Case 3: EOP USNO Finals.

| **EOP** | **Case 2 vs. Case 1** | | | **Case 3 vs. Case 1** | | |
|---|---|---|---|---|---|---|
| | shift | drift | wrms | shift | drift | wrms |
| $\Delta x_{pol}(\mu as)$ | -0.8 $\pm$ 1.5 | 0.0 $\pm$ 0.1 | 18.5 | -0.7 $\pm$ 3.5 | -0.1 $\pm$ 0.2 | 43.1 |
| $\Delta y_{pol}(\mu as)$ | -0.7 $\pm$ 1.4 | 0.1 $\pm$ 0.1 | 18.7 | -2.6 $\pm$ 3.0 | 0.2 $\pm$ 0.1 | 39.5 |
| $\Delta dUT1(\mu s)$ | 0.0 $\pm$ 0.04 | 0.0 $\pm$ 0.01 | 0.5 | 0.0 $\pm$ 0.04 | 0.0 $\pm$ 0.02 | 5.3 |
| $\Delta X(\mu as)$ | -41.7 $\pm$ 11.4 | -2.3 $\pm$ 0.5 | 157.4 | 0.8 $\pm$ 3.2 | -0.2 $\pm$ 0.1 | 43.3 |
| $\Delta Y(\mu as)$ | 94.7 $\pm$ 12.6 | -0.9 $\pm$ 0.5 | 171.9 | -0.6 $\pm$ 2.9 | 0.1 $\pm$ 0.1 | 39.6 |

**Table 2.4:** EOP differences ($\mu as$ or $\mu s$ for $UT1$) between solutions using different a priori EOP series (cases are described in the caption of figure 2.2). Shift (referred to epoch J2000.0) and linear trends ($yr^{-1}$) are estimated by Weighted LS.

### 2.4.3 Terrestrial Reference Frames

The impacts of using different TRFs to compute EOP solutions are assessed by fixing the station coordinates to their a priori values taken from the respective catalogues. This deforming procedure is not preferable but necessary here to determine the differences between the investigated catalogues. If the coordinates would not be fixed on catalogue values for this purpose, the VLBI data adjustment would change the coordinates and we would not be able to assess the consistency. Therefore, several EOP series were estimated using the five terrestrial frames given in table 2.2; in all cases, we took IERS 08 C04 for a priori EOP values and radio source coordinates ICRF2. Notice that the estimates for each TRF (fig. 2.3) are made using the same VLBI sessions, holding the $3\sigma$ eligibility criterion for all the implied frames, to achieve the maximum coherence degree in the comparison.

| **Frames** | $\Delta x_{pol}(\mu as)$ | | | $\Delta y_{pol}(\mu as)$ | | |
|---|---|---|---|---|---|---|
| | shift | drift | wrms | shift | drift | wrms |
| $ITRF2000_{fixed}$ | 97.2 $\pm$ 9.6 | 19.3 $\pm$ 0.6 | 116.3 | -122.8 $\pm$ 9.1 | -4.9 $\pm$ 0.6 | 110.3 |
| $ITRF2005_{fixed}$ | -11.3 $\pm$ 4.5 | 7.6 $\pm$ 0.4 | 53.5 | -31.4 $\pm$ 5.7 | -8.8 $\pm$ 0.6 | 75.8 |
| $VTRF2008_{fixed}$ | -48.9 $\pm$ 1.4 | -1.2 $\pm$ 0.1 | 23.3 | -27.9 $\pm$ 1.5 | -19.9 $\pm$ 0.1 | 25.1 |
| $DTRF2008_{fixed}$ | 30.8 $\pm$ 1.4 | -1.8 $\pm$ 0.1 | 20.8 | -9.0 $\pm$ 1.7 | 0.5 $\pm$ 0.1 | 23.9 |

| **Frames** | $\Delta dUT1(\mu s)$ | | |
|---|---|---|---|
| | shift | drift | wrms |
| $ITRF2000_{fixed}$ | 5.0 $\pm$ 0.3 | -0.2 $\pm$ 0.02 | 4.3 |
| $ITRF2005_{fixed}$ | 7.1 $\pm$ 0.3 | -0.5 $\pm$ 0.02 | 2.4 |
| $VTRF2008_{fixed}$ | 6.2 $\pm$ 0.06 | -0.1 $\pm$ 0.01 | 1.1 |
| $DTRF2008_{fixed}$ | 11.5 $\pm$ 0.07 | -0.2 $\pm$ 0.01 | 1.1 |

| **Frames** | $\Delta X(\mu as)$ | | | $\Delta Y(\mu as)$ | | |
|---|---|---|---|---|---|---|
| | shift | drift | wrms | shift | drift | wrms |
| $ITRF2000_{fixed}$ | -1.0 $\pm$ 1.6 | 0.0 $\pm$ 0.1 | 19.3 | -0.6 $\pm$ 1.4 | 0.1 $\pm$ 0.1 | 17.1 |
| $ITRF2005_{fixed}$ | -2.2 $\pm$ 1.0 | 0.0 $\pm$ 0.1 | 13.4 | 0.7 $\pm$ 1.0 | -0.1 $\pm$ 0.1 | 11.8 |
| $VTRF2008_{fixed}$ | -1.3 $\pm$ 0.7 | 0.2 $\pm$ 0.1 | 12.0 | 1.6 $\pm$ 0.7 | -0.3 $\pm$ 0.1 | 11.1 |
| $DTRF2008_{fixed}$ | -1.0 $\pm$ 0.6 | 0.1 $\pm$ 0.03 | 8.8 | 0.5 $\pm$ 0.7 | -0.1 $\pm$ 0.03 | 10.2 |

**Table 2.5:** EOP differences ($\mu as$ or $\mu s$ for $UT1$) between solutions using different TRFs w.r.t. ITRF2008. Shift (referred to epoch 2000.0) and linear trends ($yr^{-1}$) are estimated by LS.

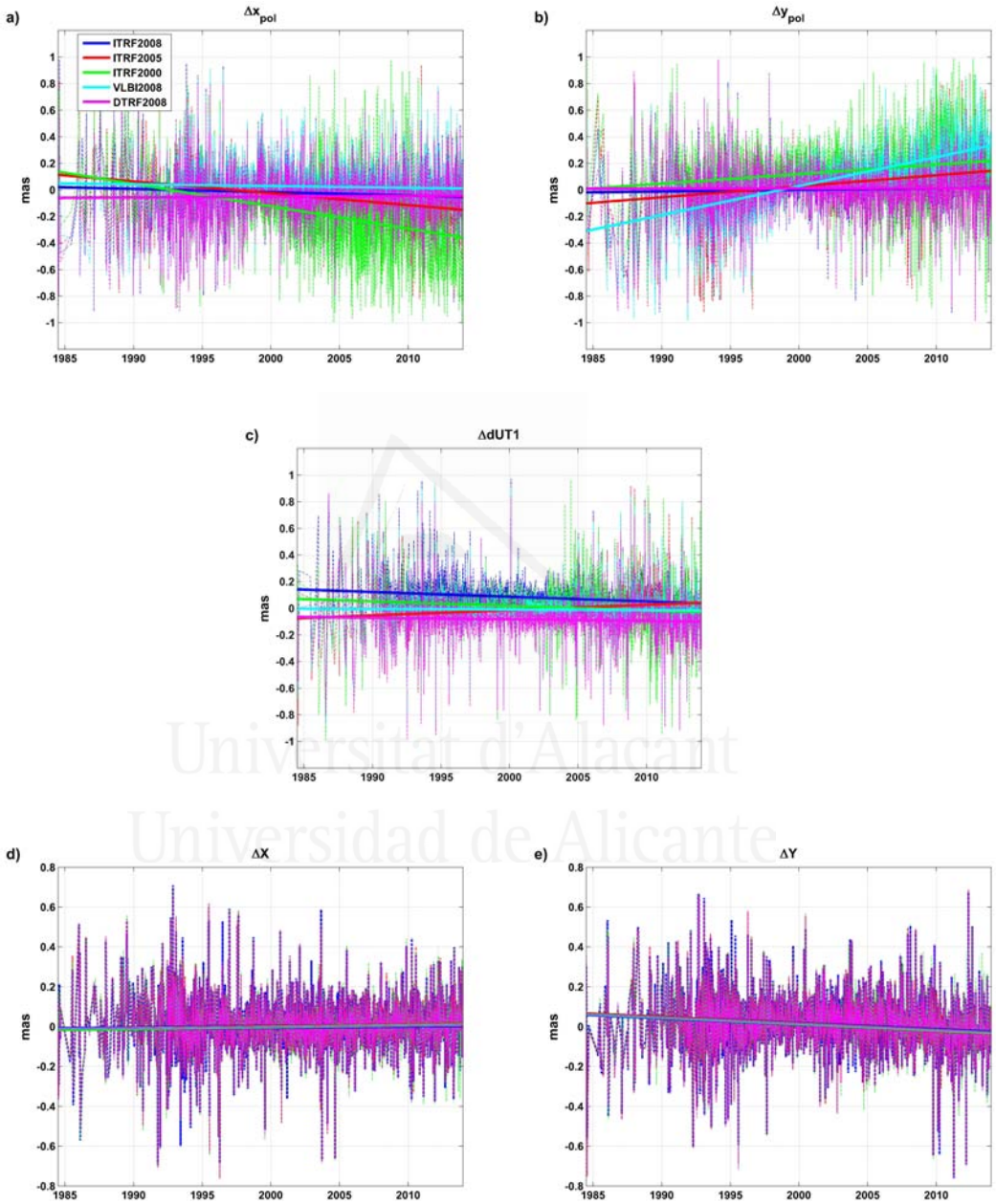


**Figure 2.3:** EOP differences w.r.t. IERS 08 C04 between solutions using different terrestrial reference frames (blue: ITRF2008, red: ITRF2005, cyan: VTRF2008, magenta: DTRF2008 and green: ITRF2000). Straight lines represent the corresponding linear trends.

Universitat d'Alacant
Universidad de Alicante

Figure 2.4 (WM and WRMS) and table 2.5 (shifts and drifts) show the differences of ITRF2000, ITRF2005, VTRF2008 and DTRF2008 w.r.t ITRF2008 expressed through the estimated EOP differences. The sign convention was the EOP series estimated from ITRF2008 minus any alternative TRF. ITRF2000 presents considerable drift for $x_{pol}$ (19.3 $\mu as\ yr^{-1}$) and large WM, WRMS and shifts in $x_{pol}$, $y_{pol}$ and $dUT1$. Between ITRF2005 and ITRF2008 there are still significant shifts in particular in $y_{pol}$. This is astonishing because ITRF2008 orientation and orientation stability are defined by No Net Rotation (NNR) condition with respect to ITRF2005. Obviously the NNR condition (kinematically non-rotation) that is based on a subset of stations common to ITRF2005 and ITRF2008 does not exactly force non-rotation for another subset of stations such as the VLBI station subset used in our study. Further interesting results are found for the VTRF2008 case, with large WM (-133 $\mu as$), WRMS (113 $\mu as$), and drift (-19.9 $\mu as\ yr^{-1}$) for $y_{pol}$; that is the result of multi-technique (ITRF2008) vs single-technique (VTRF2008) combination. DTRF2008 shows large WM (158 $\mu as$) and shift (172.7 $\mu as$) for $dUT1$, which is remarkable because both ITRF2008 and DTRF2008 are based on the same input data and accordingly, they only differ in the weighting of the techniques and the local ties among each other and in the datum definition.

Universitat d'Alacant
Universidad de Alicante

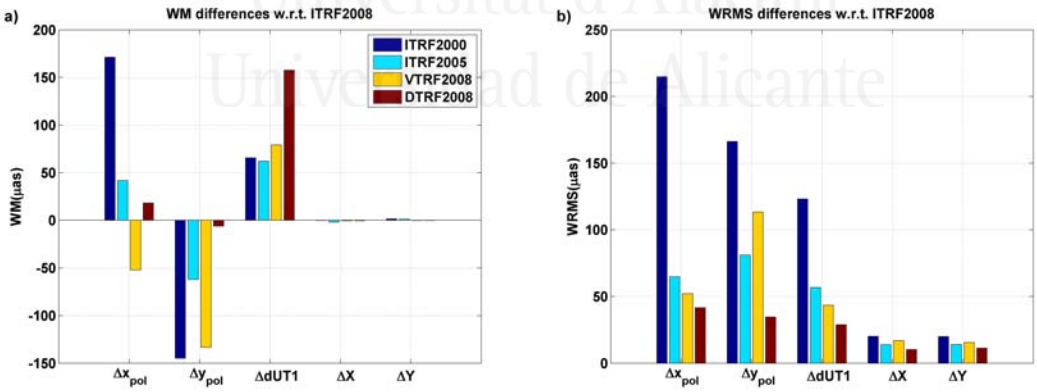


**Figure 2.4:** (a) WM and (b) WRMS differences w.r.t. ITRF2008 between EOP estimated fixing different TRFs.

Celestial pole coordinates do not show systematic effects, with small WM and WRMS (5 $\mu as$ and 10 $\mu as$ respectively) in all the evaluated cases. It is evident that the celestial pole offsets are insensitive to TRF changes, within the accuracy and stability limits set by

GGOS [Plag and Pearlman, 2009], the Global Geodetic Observing System of the IAG, and adopted in the terms of reference of the IAU/IAG Joint Working Group (JGW) on Theory of Earth Rotation [Ferrándiz and Gross, 2014]. The maximum and minimum scatter (WRMS after subtracting the linear component of the difference w.r.t. ITRF2008 series) of the EOP (table 2.5) correspond to ITRF2000 and DTRF2008 respectively.

### 2.4.4 Celestial Reference Frames

Other EOP solution series were calculated using two different Celestial Reference Frames (ICRF2 and ICRF-ext.2, table 2.1) in order to study the sensitivity of VLBI EOP to a priori CRF. In this part, the conventional terrestrial frame (ITRF2008) was used in the VLBI analysis, together with the IERS 08 C04 as a priori EOP. As in previous sections, the difference between both approaches is assessed by means of WM and WRMS.

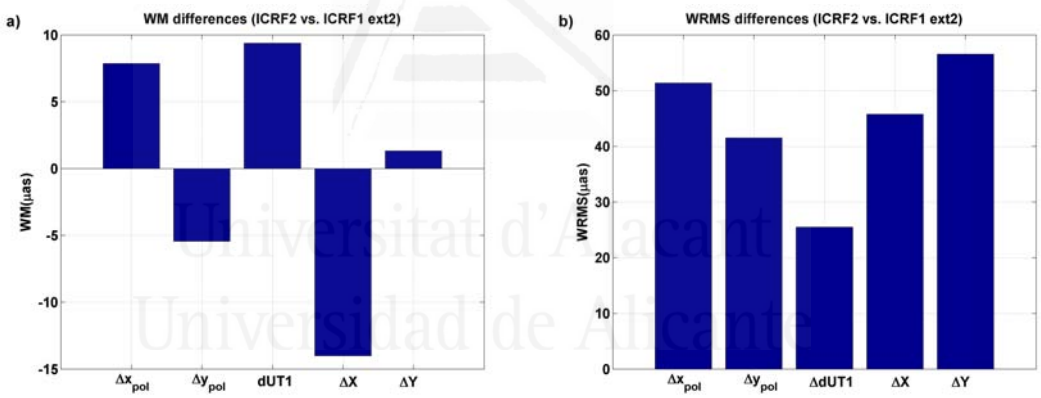


**Figure 2.5:** (a) WM and (b) WRMS differences between EOP estimated with ICRF2 and ICRF1-ext. 2.

Figure 2.5 shows the impact of the two ICRFs on the EOP that is about at the level of stability of ICRF2 axes (10 $\mu as$) with a formal error of about 40 $\mu as$ (the level of mean repeatability of ICRF2 radio source coordinates). This shows that the VLBI analysis does not significantly depend on a priori source positions. The fact that errors in source positions affect EOP in a much lesser extent than errors in station position is not unexpected at all, since in ordinary VLBI sessions the number of observed sources is much larger than the number of participating stations. It also empirically confirms that the statistics given for the ICRF2 are correct and it proofs that additionally including about 15 years

of VLBI observations (comparing ICRF and ICRF2) does not lead to systematic rotations of the ICRF. Shifts and drifts w.r.t. IERS 08 C04 (table 2.6) present analogous results for both studies, where the largest WRMS of the linear regression can be found on the EOP corresponding to ICRF-ext.2.

| **EOP** | **ICRF2** | | | **ICRF-ext.2** | | |
|---|---|---|---|---|---|---|
| | shift | drift | wrms | shift | drift | wrms |
| $\Delta x_{pol}(\mu as)$ | -17.0 ± 10.8 | -2.6 ± 0.5 | 133.4 | -22.3 ± 11.1 | -2.9 ± 0.5 | 140.2 |
| $\Delta y_{pol}(\mu as)$ | -0.4 ± 9.5 | 1.2 ± 0.4 | 122.3 | 8.0 ± 9.8 | 0.6 ± 0.5 | 127.1 |
| $\Delta dUT1(\mu s)$ | 5.8 ± 0.7 | -0.2 ± 0.03 | 8.2 | 4.7 ± 0.7 | -0.2 ± 0.03 | 8.4 |
| $\Delta X(\mu as)$ | -1.2 ± 5.6 | 0.7 ± 0.3 | 78.5 | 8.7 ± 6.2 | 1.3 ± 0.3 | 86.5 |
| $\Delta Y(\mu as)$ | 14.5 ± 5.8 | -3.1 ± 0.3 | 79.9 | 10.0 ± 6.7 | -2.1 ± 0.3 | 92.0 |

**Table 2.6:** EOP differences ($\mu as$ or $\mu s$ for $UT1$) between solutions using ICRF2 and ICRF-ext.2 w.r.t. IERS 08 C04. Shift (referred to epoch J2000.0) and linear trends ($yr^{-1}$) are estimated by Weighted LS.

### 2.4.5 Similarity transformation vs. VLBI ERP differences

To investigate whether the EOP differences determined in the chapter 2.4.3 can be attributed to the differences in orientation of the frames to some extent, the corresponding 6 Helmert transformation parameters were estimated using weighted LS. Transformation parameters of the various frames given in table 2.2 w.r.t. ITRF2008 were computed for each individual station subset of the included VLBI session: three translation components, and three rotation angles, designated $T_x, T_y, T_z, R_1, R_2, R_3$, respectively. The scale factor (D) is not determined in order to be consistent with the VLBI estimates, which have been calculated fixing the station coordinates. Equation 2.2 shows the similarity transformation applied where $x_i$, $y_i$, $z_i$ are the Cartesian coordinates of the i-th point common in the two reference frames, ITRF2008 and each considered alternative TRF:

$$\begin{pmatrix} x_{1i} \\ y_{1i} \\ z_{1i} \end{pmatrix}_{ITRF2008} = \begin{pmatrix} T_x \\ T_y \\ T_z \end{pmatrix} + R \begin{pmatrix} x_{2i} \\ y_{2i} \\ z_{2i} \end{pmatrix}_{TRF} \tag{2.2}$$

with

$$R = \begin{pmatrix} 0 & -R_3 & R_2 \\ R_3 & 0 & -R_1 \\ -R_2 & R_1 & 0 \end{pmatrix}$$

According to formula 2.2, each point generates three equations. Since the proposed system has 6 unknown quantities (where scale factor is omitted), minimum of two points is required to solve the system by weighted LS. The resolution is based in the next mathematical model $A \cdot \bar{x} - \bar{k} = \bar{r}$ with

$$A = \begin{pmatrix} 1 & 0 & 0 & 0 & -Z_{11} & Y_{11} \\ 0 & 1 & 0 & Z_{11} & 0 & -X_{11} \\ 0 & 0 & 1 & -Y_{11} & X_{11} & 0 \\ . & . & . & . & . & . \\ . & . & . & . & . & . \\ . & . & . & . & . & . \\ 1 & 0 & 0 & 0 & -Z_{1i} & Y_{1i} \\ 0 & 1 & 0 & Z_{1i} & 0 & -X_{1i} \\ 0 & 0 & 1 & -Y_{1i} & X_{1i} & 0 \end{pmatrix} r = \begin{pmatrix} r_{x1} \\ r_{y1} \\ r_{z1} \\ . \\ . \\ . \\ r_{xi} \\ r_{yi} \\ r_{zi} \end{pmatrix}$$

$$k = \begin{pmatrix} X_{21} - X_{11} \\ Y_{21} - Y_{11} \\ Z_{21} - Z_{11} \\ . \\ . \\ . \\ X_{2i} - X_{1i} \\ Y_{2i} - Y_{1i} \\ Z_{2i} - Z_{1i} \end{pmatrix} x = \begin{pmatrix} T_x \\ T_y \\ T_z \\ R_x \\ R_y \\ R_z \end{pmatrix}$$

Universitat d'Alacant
Universidad de Alicante

Transformation parameters among frames were estimated after station coordinates were referred to the VLBI session epoch (taking into account the catalog velocities). For each transformation, we used the same number of stations that in VLBI sessions. For the sake of comparison, the derived ERP (section 2.4.3) were expressed as global rotations using

$$\begin{aligned} R_1 &= -y_{pol} \\ R_2 &= x_{pol} \\ R_3 &= r' \cdot dUT1 - A_3 \end{aligned} \tag{2.3}$$

where we assumed the rotational contribution from the ICRF to $dUT1$ to be negligible ($A_3 = 0$) due to the relative insensitivity of celestial pole offsets ($dX, dY$) to TRF changes. Table 2.7 summarizes the statistics of the differences between estimated similarity transformation parameters and estimated VLBI ERP expressed as global rotations in both cases referring to ITRF2008 in terms of their relative linear regressions and Standard Deviation (SD). The most significant results are: i) similar drifts and shifts for both approaches; and ii) a SD of about 20 $\mu as$ probably caused by an incomplete atmosphere modelling and inaccuracies of the station coordinates. The largest SD can be found when comparing ITRF2008 to ITRF2000, and the smallest SD comparing ITRF2008 to DTRF2008. The large drift of $y_{pol}$ found w.r.t. VTRF2008 and the large shift of $dUT1$ w.r.t. DTRF2008 were already addressed in section 2.4.3. This proves that the VLBI data analysis works as an accurate tool to determine frame inconsistencies.

| | | **Helmert trans.** | | **VLBI** | | Comparison |
|---|---|---|---|---|---|---|
| | | shift | drift | shift | drift | sd |
| ITRF2005 | $R_1$ | 21.0 ± 12.7 | 8.8 ± 0.6 | 31.4 ± 5.7 | 8.8 ± 0.6 | 26.0 |
| | $R_2$ | 20.3 ± 8.9 | -7.7 ± 0.4 | 11.3 ± 4.5 | -7.6 ± 0.4 | 29.2 |
| | $R_3$ | 120.4 ± 6.4 | -8.7 ± 0.3 | 107.6 ± 5.8 | -7.9 ± 0.3 | 25.0 |
| DTRF2008 | $R_1$ | -0.7 ± 1.6 | 0.1 ± 0.1 | 9.0 ± 1.7 | -0.5 ± 0.1 | 20.7 |
| | $R_2$ | -35.5 ± 1.1 | 1.8 ± 0.1 | -30.8 ± 1.4 | 1.8 ± 0.1 | 18.1 |
| | $R_3$ | 172.7 ± 0.8 | -3.1 ± 0.1 | 172.7 ± 1.1 | -3.0 ± 0.1 | 13.6 |
| VTRF2008 | $R_1$ | 19.8 ± 1.6 | 19.8 ± 0.1 | 27.9 ± 1.5 | 19.9 ± 0.1 | 21.9 |
| | $R_2$ | 47.1 ± 1.5 | 1.6 ± 0.1 | 48.9 ± 1.4 | 1.2 ± 0.1 | 21.4 |
| | $R_3$ | 96.3 ± 0.9 | -0.5 ± 0.1 | 92.9 ± 0.9 | -1.2 ± 0.1 | 16.7 |
| ITRF2000 | $R_1$ | 113.8 ± 9.9 | 4.3 ± 0.6 | 122.8 ± 9.1 | 4.9 ± 0.6 | 50.5 |
| | $R_2$ | -84.5 ± 8.8 | -19.9 ± 0.6 | -97.2 ± 9.6 | -19.3 ± 0.6 | 50.8 |
| | $R_3$ | 90.9 ± 5.0 | -1.9 ± 0.3 | 74.7 ± 5.3 | -3.2 ± 0.3 | 40.8 |

**Table 2.7:** Global rotations ($R_1, R_2$, and $R_3$) for each VLBI session from similarity transformation and ERP differences between ITRFs w.r.t. ITRF2008 based VLBI solutions. Shifts (referred to epoch J2000.0) and annual drift are estimated by LS. Units: $\mu as$.

## 2.5 Discussions and Conclusions

A consistency study has been shown concerning the current conventional reference frames (ITRF2008 and ICRF2) and the IERS 08 C04 series. To assess the inconsistency among

terrestrial and celestial frames and involved EOP, the only technique that can be applied is VLBI. Notice that the precision of this assessment is limited to the quality of the VLBI data analysis.

Concerning the unmodeled geophysical signals study conducted in section 2.4.1, one can say that these neglected signals induce damaging effects on the pole coordinates and $dUT1$ causing a strong decrease of the correlation among EOP based on fixed coordinates and EOP based on adjusted coordinates with a priories from ITRF2008. Maximal shift of -33.5 $\mu as$ and maximal drift difference of 2.9 $\mu as\ yr^{-1}$ take place in $y_{pol}$.

The EOP estimated by VLBI analysis might in addition depend on the choice of a priori EOP and thus, we investigated that possibility. Here we compare EOP adjustment with respect to IERS 08 C04 when using IERS 08 C04, USNO finals, or the astronomical conventional precession/nutation models, IAU 2006/2000A. EOP estimated using IERS 08 C04 and USNO finals exhibits a large scatter of $dUT1$ at the level of 80 $\mu as$.

VTRF2008 is consistent with ICRF-Ext.2 and ICRF2 contains precise positions of more than 3000 compact radio astronomical sources, more than five times the number as in ICRF1. In order to analyze the stability of the system axes between ICRF2 and ICRF-Ext.2 different EOP series are estimated with identical VLBI solutions but with different celestial reference frames (ICRF2 and ICRF- Ext. 2). The maximal EOP differences (9.9 $\mu as$ at $\Delta X$ and 1 $\mu as\ yr^{-1}$ at $\Delta Y$) obtained fulfills the stability goal of about 10 $\mu as$. Therefore, ICRF2 and ICRF-Ext.2 orientations can be assumed identical within this uncertainty, which is well below the threshold of accuracy targeted for the next years, e.g. by GGOS or associated working groups.

However, when the EOP estimated by fixing station positions on various terrestrial reference frames are compared with respect to ITRF2008, significant inconsistencies are detected. ITRF2000 and ITRF2005 are included in the comparison because the orientation of ITRF2008 is realized by NNR conditions with respect to the orientation of ITRF2005, which in its turn is realized via NNR condition with respect to ITRF2000. It is interesting to note that although the ITRF2008 and the ITRF2005 are constrained to be kinematically non-rotating with an uncertainty of 8 $\mu as$ and 8 $\mu as\ yr^{-1}$ significant differences above this level and even larger discrepancies with respect to ITRF2000 are found (in particular in pole coordinates) based on the VLBI subset of stations. A marked inconsonance is the drift difference in $y_{pol}$ of about -19.9 $\mu as\ yr^{-1}$ between VTRF2008 and ITRF2008, it means that ICRF2, ITRF2008 and the conventional EOP series are not completely consistent.

ITRF2000 shows large shifts in $x_{pol}$ and $y_{pol}$, and a significant drift of about 19.3 $\mu as\ yr^{-1}$ in $x_{pol}$. Besides, $dUT1$ evidences substantial inconsistency problems in all tested TRFs, the most pronounced results being between ITRF2008 and DTRF2008 (more than 5 mm at the Earth equator). These detrimental effects could come from unconsidered geophysical signals (e.g. non-tidal ocean) which are neglected and need to be identified.

In the last 30 years the EOP accuracy has reached levels where the margin of improvement is extremely limited. In spite of this enhancement, our study confirms the conclusion that the IERS EOP series is not accurate enough to achieve the GGOS goal and that some inconsistencies are visible at that stringent accuracy level, like those shown in the various tests performed in this chapter. Problems might come from during the combination of ITRF2008, the EOP that are consistently determined are only the terrestrial pole coordinate offsets, $dUT1$ and LOD. However, offsets of the Celestial Intermediate Pole (based on VLBI results) are ignored and added later for the sake of completeness. Moreover, the orientation of the VLBI ground network that refers to ICRF via the VLBI EOP is allowed to rotate during the combination. Consequently, the IERS 08 C04 does not refer exactly to ICRF. Other potential causes of inconsistency are; the current methodology of inheriting the orientation from the previous realization to the current realization applying the NNR condition, i.e. the new frame inherits the errors of all its predecessors and adds its own errors; and the misfit of the true coordinate and the simple coordinate model used for its approximation, i.e. the uncorrected non-linear station displacement will propagate into EOP since not all non-linear effects are removed. These causes could be among the reasons why the optimum consistency level is not being accomplished yet. Proposals to achieve higher accuracy and consistency are that the ITRF, the EOP and the ICRF have to be determined in one monolithic adjustment including all observations of all involved techniques (VLBI, DORIS, GNSS, and SLR), the usage of epoch reference frames [Bloßfeld et al., 2014] and extending the TRF coordinate model to include seasonal signals as it is foreseen for the next realization of ITRS, ITRF2014 (Altamimi, pers. comm.).

Universitat d'Alacant
Universidad de Alicante

*All of science is nothing more than the refinement of everyday thinking.*

Albert Einstein

CHAPTER

3

# Testing a new Free Core Nutation empirical model

## 3.1 Introduction

[1]The Earth's Free Core Nutation, also known earlier as the Nearly Diurnal Free Wobble (NDFW) because of its origin and period in the terrestrial frame, is a free-oscillation mode of an Earth model consisting of a solid mantle and a fluid core. It is the retrograde motion due to the misalignment between the rotation axes of the mantle and the core [Smith, 1977; Toomre, 1974; Wahr, 1981]. Kinematically, it resides in the "nutation frequency band", along with all astronomical forced nutations and sharing with them the same frequency characteristics. As far as the rotation of the mantle (or "Earth rotation") is concerned, it has a long retrograde period of about 430 days (and an average amplitude of about 100 $\mu as$) relative to the inertial frame, or a retrograde period of slightly shorter than 1 day, in the retrograde-diurnal band, relative to the rotating terrestrial frame. FCN is a free mode of Earth rotation, i.e. it shows variable excitation or damping.

Some of the astronomical nutations have periods sufficiently close to that of FCN that they feel the resonance effect which magnifies their amplitudes, the most notable example

[1]Chapter submitted to Journal of Geodynamics

being the retrograde annual nutation. In fact, that was how FCN was first identified in nutation time series obtained by VLBI [Gwinn et al., 1986; Herring et al., 1986]; the signal was at milli-arcsecond (mas) level. Similarly, gravitational effects of FCN have also been detected in surface gravity records from superconducting gravimeter [Defraigne et al., 1995; Florsch and Hinderer, 2000; Richter, 1988] and long-period seismometers [Cummins and Wahr, 1993]. The period estimates range between 425-435 days, rather than the predicted 460 days based on the hydrostatic theory for the Earth, implying a more elliptical core than would be a hydrostatic core. In a recent accurate study published by Krásná et al. [2013] the FCN period was determined as 431.18 sidereal days, close to the value of 430.21 solar days estimated by Lambert [2007].

It is well known that the current IAU2000 nutation theory needs to be complemented with a model providing the FCN, since otherwise the observation-theory residuals of the CIP coordinates would be noticeably large (approaching about 180 $\mu as$), thus damaging the prediction accuracy. The FCN signal exhibits complex patterns of variation affecting its amplitude, period and phase, whose geophysical causes are not fully understood yet, although recent studies dealing numerically with the effects of excitations are producing interesting insight. Nevertheless, today it is still necessary to use empirical models to describe the inferred FCN signal and to predict it to a limited extent, like the model of Lambert [2007] recommended in the IERS Conventions 2010, which is regularly updated.

IAU2000 nutation theory was fitted with the help of a FCN model that has its amplitude determined as a piecewise linear function of time at yearly intervals. Shirai and Fukushima [2000a;b] used a more involved model including exponential decay and the possibility of sudden jumps. Ferrandiz et al. [2002] developed the first model based on a Sliding Window approach (with window lengths of either one or two FCN periods), that had already been successfully applied in the analyses of PM by Schuh et al. [2000]. Lambert [2007] developed a Sliding Window solution that provides one reference value of the amplitude for each year, which can then be used for interpolation.

The scientific community demands the empirical FCN models with increasingly high accuracy to improve the knowledge about the geophysical excitation mechanisms that cause the amplitude, period, and phase variations. In this research we develop a new empirical FCN model with higher temporal resolution fitting the amplitude parameters directly to the solution of the VLBI data analysis (1984-2013) performed with the GFZ version of the VieVS. A comparison with other recently determined empirical FCN models: Krásná

et al. [2013] and Lambert and Dehant [2007] is included by means of the weight root mean square of the residuals during the entire period of VLBI data. Moreover, we assess the sensitivity of our empirical FCN model with respect to different a priori Earth Orientation Parameter series: IERS 08 C04 and USNO finals.

## 3.2 FCN modeling in VLBI data

The orientation of the Earth's rotation axis in the inertial space is customary given by the $X$ and $Y$ coordinates of the celestial pole. Using distant quasar sources as reference frame, VLBI is at present the unique technique in space geodesy that is capable of accurately observing the 3-D EOP in space. In the VLBI observation of the variation of the Earth's rotation axis, the empirical convention is such that the bulk of the broad-band signal is considered as the polar motion; only the signal residing in the narrow retrograde-diurnal band is considered as nutations.

In this nutation band, the VLBI nutation time series contains FCN plus a great number of astronomical nutation components, many of which have much larger or comparable amplitudes than the FCN can realistically have. In the time domain, the FCN signal is "buried"; it is thus simpler to conceptualize it in the frequency domain. The nutations are purely sinusoidal at periods that are precisely known from celestial mechanics. However, their amplitude and phase are not precisely known, subject to either observational errors or modeling uncertainties. This lack of knowledge is especially severe for components that are close to the FCN period due to the near-resonance magnifying effects mentioned above. As far as FCN itself is concerned, it is thus difficult to completely model and remove the nutation terms, which is necessary in order to reveal the true properties and behavior of FCN. Therefore, one must first carefully model the astronomical nutations to the extent of present knowledge.

The study of Earth Rotation involves to determinate the position of the instantaneous axis of rotation or angular velocity of the Earth in two reference frames (terrestrial and celestial). There are five EOP available and we focus our discussion on two angles with respect to the celestial frame. The celestial pole coordinates $(X, Y)$ are currently provided by VLBI in the form of a time series, that consists of the computed residuals, or "off-sets" $(\Delta X, \Delta Y)$, of the observed CIP coordinates from VLBI with respect to the IAU 2006/2000A precession/nutation models.

Universitat d'Alacant
Universidad de Alicante

In recent years some alternative ”complete” nutation theories have been under development, including IAU 2006/2000A [Capitaine et al., 2003; Mathews et al., 2002], GF2000 [Getino and Ferrándiz, 2000], SF2000 [Shirai and Fukushima, 2001]. These models provided modifications and improvements that compete in accuracy down to the micro-arcsecond level in astronomical precession and nutations. The astronomical nutation models have to be complemented with an empirical term corresponding to the FCN. IERS Conventions 2010 [Petit and Luzum, 2010] recommends an empirical FCN model of Lambert [2007]. However, other models are available today [Krásná et al., 2013; Malkin, 2010].

The procedure leading to the VLBI time series that we utilize is described as follows. We took all available VLBI data from 1984 to 2013. Positions and velocities of all stations as well as source coordinates were estimated by imposing no-net-translation and no-net-rotation conditions with respect to ITRF2008 and ICRF2. After single-session adjustment, we discarded the VLBI sessions with a posteriori sigma of unit weight larger than 3.

## 3.3 Empirical FCN models

FCN models can be characterized from a weighted least squares fit of these equations:

$$\begin{aligned} X_{FCN} &= A_C \cos(\sigma_{FCN} t) - A_S \sin(\sigma_{FCN} t) \\ Y_{FCN} &= A_S \cos(\sigma_{FCN} t) + A_C \sin(\sigma_{FCN} t), \end{aligned} \tag{3.1}$$

where $\sigma = 2\pi/P$ is the frequency of FCN in the Celestial Reference Frame (CRF), $A$ is the amplitude, $t$ is the time relative to J2000.0 and $P$ is the period.

FCN amplitudes and phases are not fix over time, but exhibit a noticeable variation. Causes of this variability need to be identified and predicted with high accuracy, which is an indispensable requirement to fulfill the stringent GGOS targets as well as for many practical geophysical applications. That is why a large quantity of empirical FCN models are estimated and tested here with different sliding window length $N_L$ (from 8 months to 7 years) displaced by different time intervals $N_D$ ($\leq N_L$) to make a new fit with the purpose of finding the optimum parameters that provide the lowest residuals. We adopted a constant period of -431.18 sidereal days, the value determined recently by Krásná et al. [2013], since the phase and period would be correlated in the fitting. Upon considering the fixed period, the possibility to estimate the amplitudes from $N_L$ lesser than the FCN period (-431.18

sidereal days) had to be checked and examined. Therefore, models with high temporal resolution were calculated using a small window size. The advantage of these models is the ability to recognize and relate the geophysical changes with FCN amplitude and phase variations.

Several solutions for the EOP using the VLBI data were carried out. The estimates were computed starting from different a priori ERP series (taking the PM and LOD values from IERS 08 C04 and USNO finals), and the CIP coordinates from IAU 2006/2000A precession/nutation theory. All FCN models were derived on the analysis of the differences between the celestial pole coordinates determined from VLBI observations and the coordinates determined from IAU 2006/2000A theory. The different model simulations were used to eliminate the FCN effect, all of them being a nutation of time-varying amplitude and phase but constant period of -431.18 sidereal days. In the multiple estimates, after removal of the FCN, a small curvature is visible, with approximately the same magnitude and opposite signs. Thus, $\Delta X$ and $\Delta Y$ are corrected for a linear term plus a 18.6 year main nutation term before estimating the FCN models similarly to Capitaine et al. [2009] (figure 3.1).

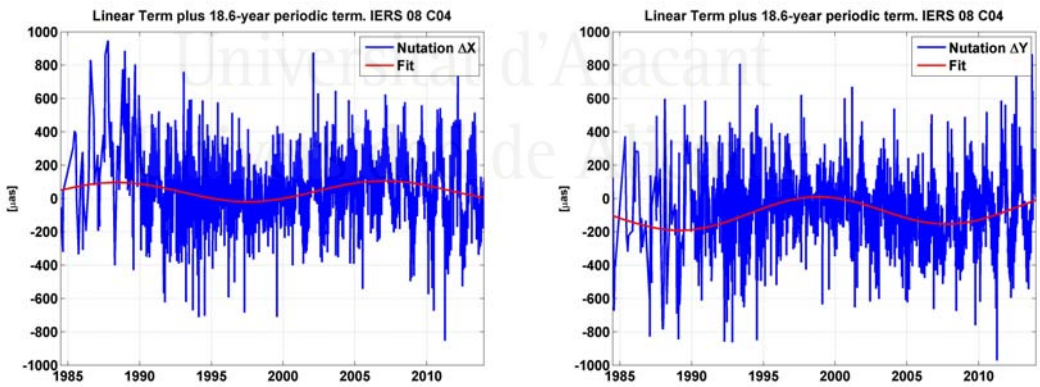


**Figure 3.1:** $\Delta X$ and $\Delta Y$ residuals (blue line) are used to fit a linear trend plus 18.6 year periodic term (red line) using a priori ERP from IERS 08 C04 and a priori X,Y from IAU 2006/2000A model.

## 3.4 Results

### 3.4.1 Sliding Window: Size and Displacement

A large variety of FCN models based on different a priori ERP (IERS 08 C04 and USNO Finals) were determined using different $N_L$ and $N_D$. One of the FCN models which were calculated with a sliding window of 2 FCN periods and half-yearly displaced using a priori ERP from IERS 08 C04 is shown in the figures 3.2a and 3.2b. Theoretically if all signals (linear and non-linear) could be perfectly modeled by IAU 2006/2000A precession/nutation model, the remaining residuals would be close to zero once the FCN effect was deleted. However, this does not happen because of the limitations of theories and models (figures 3.2c and 3.2d).

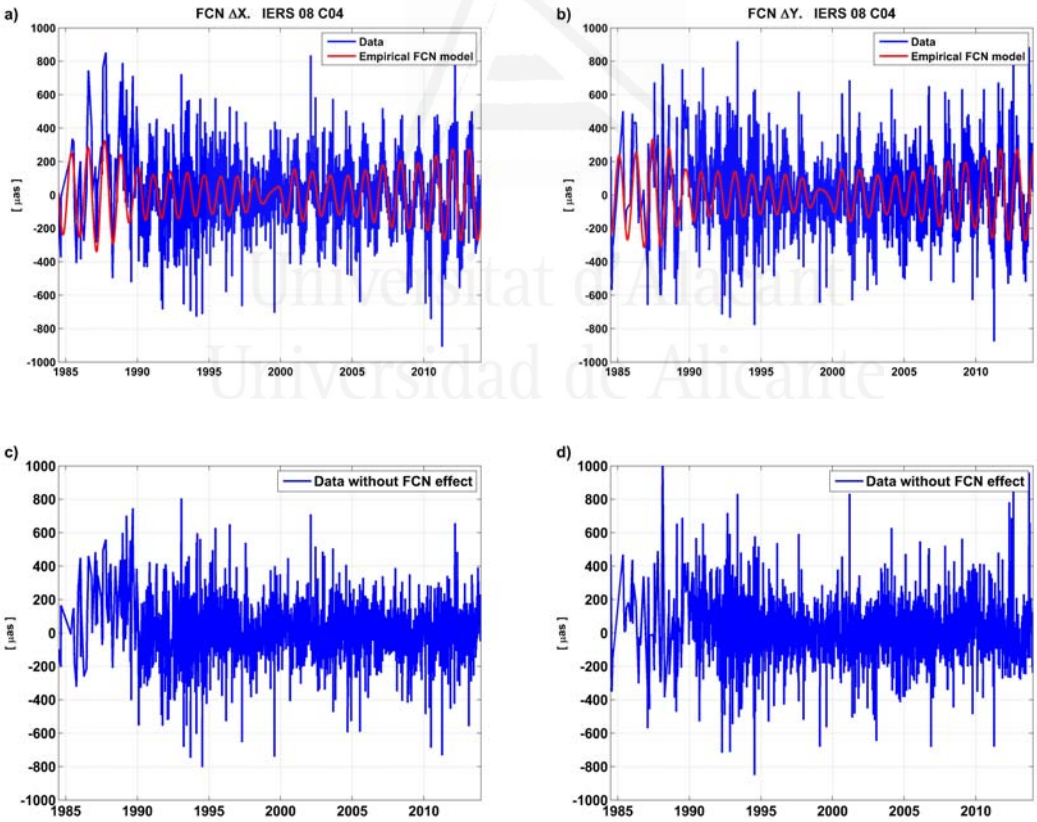


**Figure 3.2:** Upper: Empirical FCN model estimated from a $N_L = 2$ FCN cycles (periods) and $N_D = 6$ months. Lower: Residuals of the IAU 2006/2000A precession/nutation model w.r.t. VLBI time series after FCN has been removed. A priori ERP from IERS 08 C04.

In order to determine and check the most proper values of $N_L$ and $N_D$, the SD of the celestial pole offsets were estimated after removing the FCN effect. The SD for every experiment by both IERS 08 C04 and USNO finals as a priori ERP is shown in figures 3.3a and 3.3c respectively. The most suitable FCN models (low scattering) are located on the left side for each approach (tiny $N_L$). Notice that the smallest error of about 150 $\mu as$ corresponds to use a priori ERP from the USNO finals. However, IERS 08 C04 series causes a slight deterioration at the modeling.

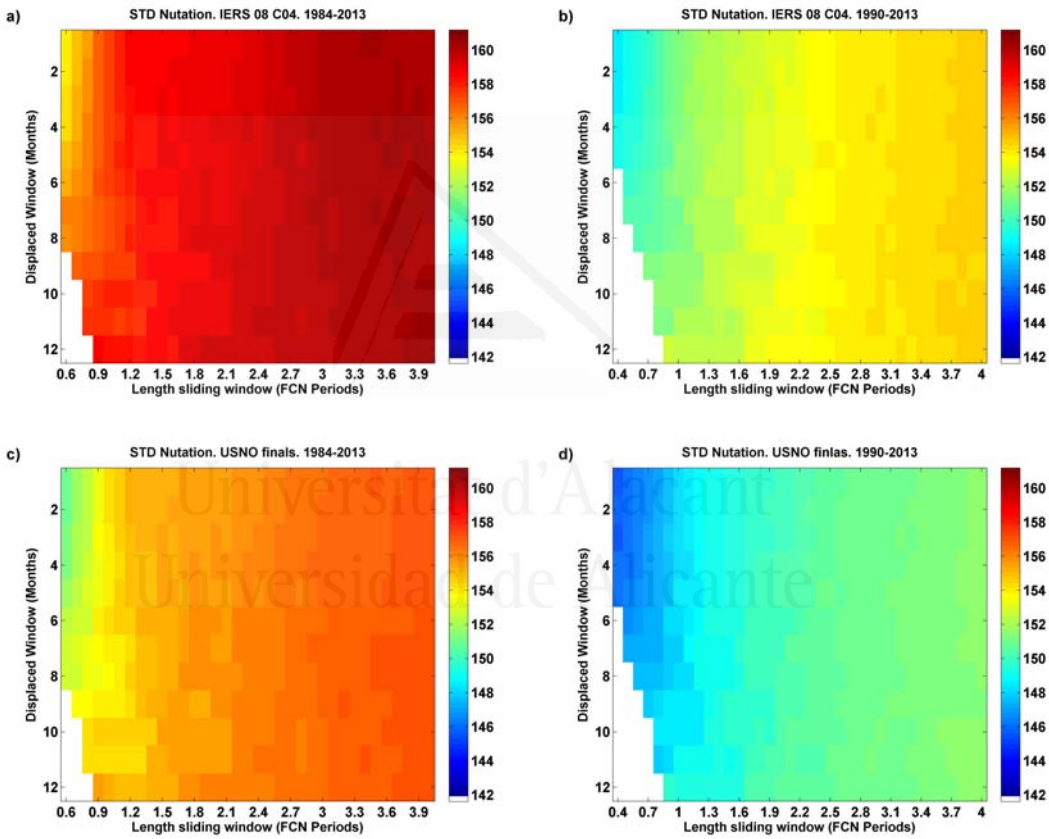


**Figure 3.3:** SD of the residuals after FCN has been removed from different a priori ERP. Upper: IERS 08 C04. Lower: USNO Finals. Left: sessions taken into account from 1984 to 2013. Right: sessions from 1984 to 1990 were discarded. Same color scale was applied for all the figures. White color: no data. Units: $\mu as$.

With the aim of getting more accuracy, the first six years in the VLBI analysis were deleted as a consequence of the poor quality and temporal resolution of VLBI sessions in the eighties (figures 3.3b and 3.3d). In this case the errors drop around 8 percent. It is import-

ant to mark that the range of the sliding window length varies from 0.6 to 4 cycles for the whole period, but if early VLBI sessions had been eliminated the range could be extended up to 0.4. Values of $N_L$ below these quantities models could be unstable.

In addition to the previous error analysis, another study was performed. Supplemental VLBI estimates were computed using different a priori ERP (IERS 08 C04 or USNO Finals) including the Celestial Pole Offsets instead of the IAU 2006/2000A precession/nutation model plus FCN model. With a view to find the maximum consistency and agreement, these new calculations, which should be free of FCN, are compared with remaining residuals of the whole simulated empirical FCN models by means of the WRMS difference (figure 3.4).

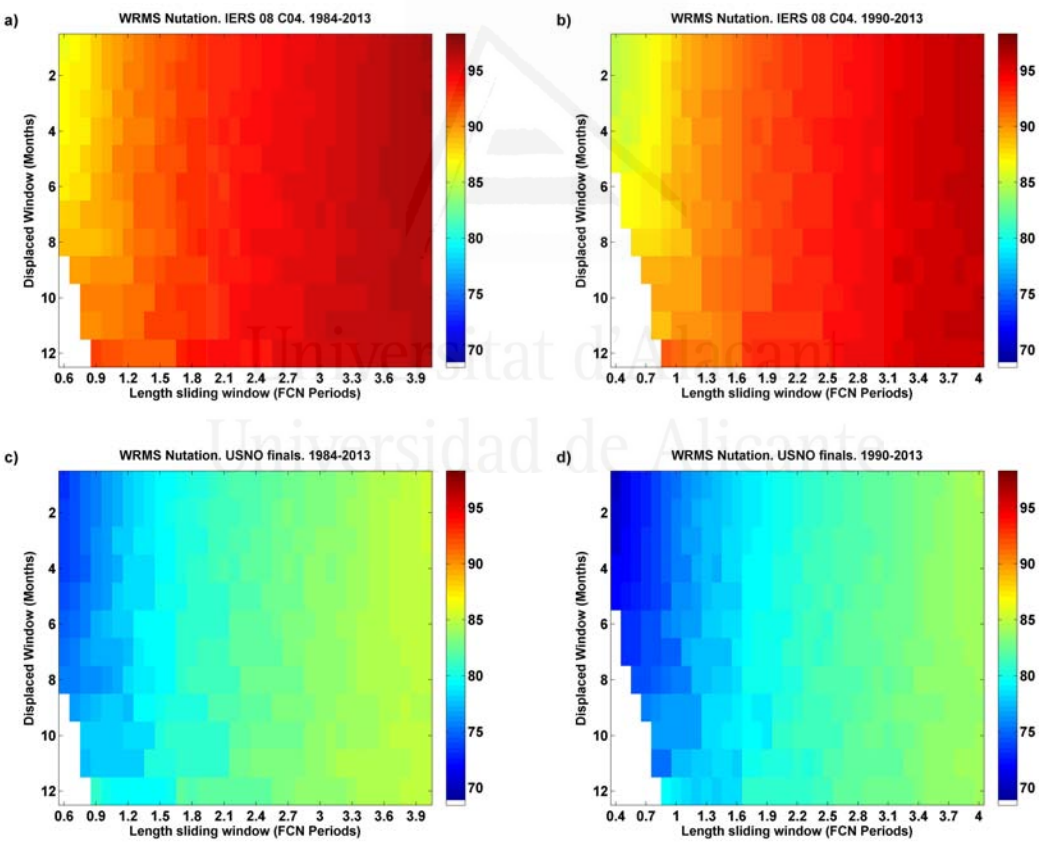


**Figure 3.4:** WRMS differences between the remaining residuals once FCN has been removed using different sliding window lengths w.r.t. VLBI estimates computed from different a priori ERP including the CPO. Description as in figure 3.3. Units: $\mu as$.

The finest results (minimum WRMS) are located close to the smallest $N_L$ values, as the

minimum SD registered in figure 3.3. The FCN models estimated from IERS 08 C04 as a priori ERP achieves the less accurate results with minimum WRMS of about 86 $\mu as$. On the other hand according to our estimates, USNO Finals as a priori ERP seems to provide the most rigorous models (the lowest WRMS over 70 $\mu as$). Anew, residuals decrease when sessions from 1984 to 1900 were not taking into account.

A priori, the previous error analyses (shown in figure 3.3 and 3.4) have proven the great importance to choose the proper sliding window size ($N_L$), since inappropriate values could cause accuracy variations of about 15 $\mu as$. Less significant is the displacement between the subsequent fit ($N_D$) in which the residuals hardly change.

### 3.4.2 Amplitude and phase

Once the usefulness of choosing an appropriate sliding window length is tested in terms of accuracy, the amplitude and phase variations for the whole simulations are analyzed to study their influence and connection to geophysical changes. For any FCN model given in the form of a series of corrections to the $X$ and $Y$ coordinates of the celestial pole, the FCN amplitude $A(t)$ and phase $\theta(t)$ can be easily calculated using

$$\begin{aligned} A(t) &= \sqrt{\Delta X^2 + \Delta Y^2} \\ \theta &= \arctan \frac{\Delta Y}{\Delta X} \end{aligned} \tag{3.2}$$

The values of $\theta$ are in $[0, 2\pi)$, but the image of $\arctan$ is $(-\pi/2,\ \pi/2)$. Then, the signs of $\Delta X$, and $\Delta Y$ must be taken into account to infer the value of $\theta$ as

$$\theta = \begin{cases} \arctan\left(\dfrac{\Delta Y}{\Delta X}\right), & \text{if } \Delta X > 0,\ \Delta Y \geq 0, \\ \pi + \arctan\left(\dfrac{\Delta Y}{\Delta X}\right), & \text{if } \Delta X < 0, \\ 2\pi + \arctan\left(\dfrac{\Delta Y}{\Delta X}\right), & \text{if } \Delta X > 0,\ \Delta Y < 0, \\ \dfrac{\pi}{2}, & \text{if } \Delta X = 0,\ \Delta Y > 0, \\ \dfrac{3\pi}{2}, & \text{if } \Delta X = 0,\ \Delta Y < 0. \end{cases}$$

Universitat d'Alacant
Universidad de Alicante

Depending on the setting ($N_L$ and $N_D$), the amplitude and phase variations can be determined with variable accuracy and approximation. Figure 3.5 displays the most meaningful experiments computed by different sliding window procedure. The data presented show that these FCN models exhibit similar variations in the amplitude and phase in spite of their different scenarios, but the variations assigned to $N_L = 4$ FCN periods and $N_D = 12$ months are smoother than the rest. In summary, the shorter the length of the sliding window is, the bigger the sensitivity with respect to the geophysical changes will be and vice versa.

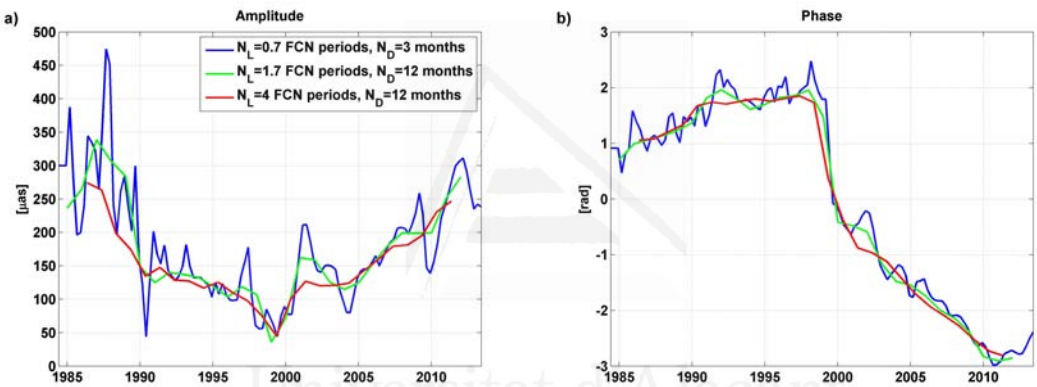


**Figure 3.5:** Amplitude and phase variations from three different FCN models (blue (0.7 periods ≈ 10 months, green ≈ 2 years, and red ≈ 4.6 years).

Another fact to note is that the amplitude is about 250 $\mu as$ prior to 1990, but dropped to about half since 1990. This suggests that FCN follow a exponential decay law to a large extent up to 2000. The behavior is reversed near 2000 up to 2013. Jumps can be visualized with little effort, around the whole series. This supports the hypothesis that FCN can be excited by sparse sudden events, what justifies the analysis via different sliding window length in order to catch the unmodeled signals. Due to the poor VLBI data available in the early years, big jumps could appear as a consequence of low session numbers. Sometimes, this lack of data in the 80s could make it difficult to estimate the amplitude and phase with high resolution. In that case, the interpolation or smoothing are recommended to avoid inaccurate geophysical interpretations.

### 3.4.3 Comparison with other models

Krásná et al. [2013] recently determined a FCN model using groups of 4 years ($\approx$ 3.4 FCN periods) measurements data displaced one year. Data from 1984.0 to 1988.0 in the first run were involved and thus the estimates are valid for 1986.0. The second global solution includes data from 1985.0 till 1989.0 and so on. She used a period of -431.18 sidereal days. Lambert [2007] estimated a FCN model (IERS Conventions 2010) using a period of 431.39 sidereal days, a sliding window size of two years (730 days $\approx$ 1.7 FCN periods) and displaced by one year. These models were compared with respect to the different empirical simulations computed in the previous sections with the aid of the WRMS of the residuals after removing FCN (figure 3.6).

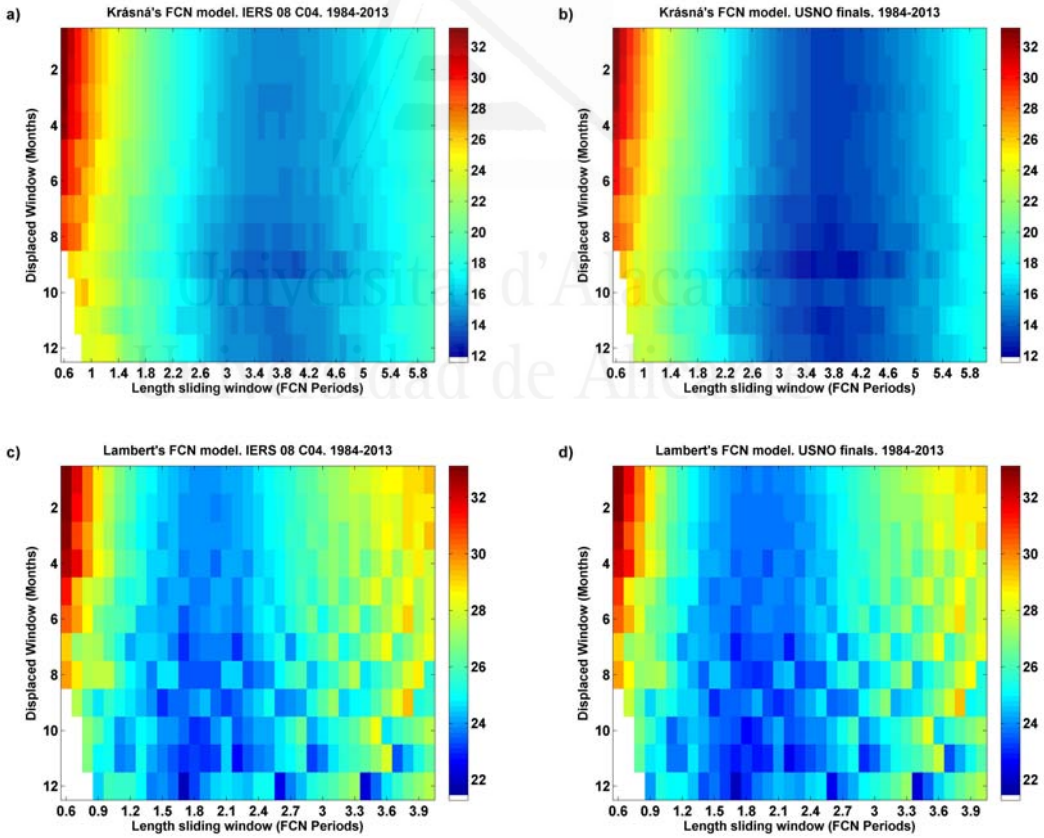


**Figure 3.6:** WRMS difference of the residuals between our estimates and Lambert's (lower) or Krásná (upper) model. FCN effect removed. Right: USNO Finals. Left: IERS 08 C04. White color: no data. Units: $\mu as$.

Consequently, in the comparison procedure we expect the minimum WRMS differences located close to 1.7 and 3.4 FCN cycles, being consistent with the groups of data which were used for Lambert and Krásná, respectively. That is why a area of low residuals can be detected in the figure centers, coinciding with the aforementioned cycles (figure 3.6). A same pattern can be seen with different a priori EOP.
The smallest residuals in the comparison, of about 12 $\mu as$, correspond to the Krásná's model, along with the USNO Finals as a priori ERP. Lambert's model achieves errors 10 $\mu as$ larger than the Krásná model. Note that the best concordance with Krásná model could be due to the use of the same FCN period and VLBI software (VieVS). Again, the USNO Finals series as a priori reaches better accuracy than IERS 08 C04. The improvement is around 2 $\mu as$.

## 3.5 Discussions and Conclusions

Previous studies of FCN mostly focused on FCN's resonance effect on neighboring astronomical nutations found in VLBI and gravity data. Such indirect evidences are well suited for estimating FCN's natural period, but unable to provide information about the behavior of FCN over time. Direct evidences for the latter begin to emerge as VLBI data quality improves. In this study, we estimate different empirical FCN models using the residual VLBI nutation time series from 1984.0 to 2013.0 obtained after the astronomical nutations are accounted for and then removed according to the IAU 2006/2000A precession model. Phase and amplitude variations are examined. Furthermore, different EOP (IERS 08 C04 and Usno Finals) are analyzed with a view to know which series achieves the optimal FCN model. Finally, a comparison with Krásná and Lambert model was done. In all the estimates the period was fixed to the recent value determined by Krásná et al. [2013].

Large number of FCN models were estimated and assessed. The methodology and the choice of the sliding window length vary for each simulation. Least-squares estimates of the amplitude were done at each interval of sliding window, where the displacement between the subsequent fit changes among 1 and 12 months. This investigation confirms that the use of FCN models determined from the shortest sliding window size substantially improved the accuracy of the modeling, achieving an improvement in WRMS up to 15 $\mu as$. Moreover, the usage of IERS 04 C08 as a priori ERP series gives slightly larger residuals. Therefore the USNO Finals series provide the better accuracy when assessed

with these empirical FCN models. The highest agreement for all our simulations with different available FCN models occurs close to the corresponding FCN number of cycles: Krásná's (3.4 cycles) and Lambert's (1.7 cycles), with Krásná et al. [2013] being the most favorable. Our models computed with reduced window lengths show an improvement of 20 $\mu as$ w.r.t. both, Krásná's and Lambert's models. Residuals drop if VLBI sessions from 1984-1990 were eliminated due to the low temporal resolution and accuracy.

The FCN is essentially the only signal that remains above the noise level. It clearly has a time-variable amplitude during the studied period, as can be demonstrated by a simple wavelet time-frequency spectrum. A sliding window least-squares fit of the FCN amplitude yields similar results: To first order, the amplitude hovers around 0.3 mas prior to 1990, then it drops to about half of that value. Dynamically the FCN is a free-oscillation mode in the Earth's rotation and hence a decaying harmonic function of time if left unexcited. Thus the time-variable amplitude is a clear evidence that the FCN has been subjected to episodic, if not continual excitations by some geophysical processes. The situation is analogous to the continual geophysical excitation of the Chandler wobble, another free oscillation in the Earth's rotation, resulting in its time-variable amplitude that has been long observed and studied since around 1900. While the excitation of the Chandler wobble can be traced to meteorological origin [Furuya et al., 1996; Gross, 2000], long-term variation of the Chandler wobble amplitude has not been explained. Similarly, there has been no clear evidence as to the excitation source(s) of FCN. In spite of this, the new tested empirical FCN models of high temporal resolution can help to enhance the understanding about the amplitude and phase variations, which in turn is related to the geophysical excitations. Wider window lengths produce smoother amplitude and phase variations and vice versa.

An ultimate pursuit in front of us is to identify the geophysical phenomena that excited the FCN in the way that is observed. One possible candidate is again meteorological disturbances in the form of broad-band variations of atmospheric, oceanic, and hydrological angular momentum. Furthermore, on excitation-domain study, one can confidently presume that some major FCN excitation occurred around 1990. One can further speculate the possibility of certain large and deep seismic events, some episodic jerky disturbances in the core, or even major solar mass-ejection events exerting magnetic torques on the Earth.

Universitat d'Alacant
Universidad de Alicante

Universitat d'Alacant
Universidad de Alicante

*The logic of validation allows us to move between the two limits of dogmatism and skepticism.*

Paul Ricoeur

CHAPTER

4

# On the decorrelation filtering of RL05 GRACE data for global applications

Universitat d'Alacant
Universidad de Alicante

## 4.1 Introduction

The GRACE mission was launched in March 17, 2002. The GRACE mission measures the distance between two twin satellites in near polar orbit. These distances are used to estimate monthly geopotential spherical harmonics SC, called Level 02 GRACE data, by Center for Space Research (CSR), GFZ, and Jet Propulsion Laboratory (JPL). Actually, these SC represent the geopotential differences with respect to a geopotential background, where some known geophysical processes are modeled: solid Earth and oceanic tides (including pole tides), non-tidal variability of the atmosphere and ocean, and gravity perturbations due to the Sun, Moon and the rest of the planets [Bettadpur, 2012; Dahle et al., 2013; Watkins and Yuan, 2012].

Assuming that the geopotential variations are produced by mass changes at the surface of the Earth, it is possible to estimate the associated mass maps in form of millimetres of water thickness equivalent [WTE; Chao, 2005; Wahr et al., 1998]. These maps show north−south stripes due to some noise in the high degree and order SC. So, they must

be filtered to reduce that noise. However, there is not a standard filtering procedure and the GRACE users must decide which is the most convenient in their studies. There are several ways of filtering the data that can be found in the literature [Duan et al., 2009, and references therein]. However, one of the most popular filtering procedures, due to its easy implementation, is a two-step filter that first applies the decorrelation error filter [Swenson and Wahr, 2006], and then the isotropic Gauss filter [Jekeli, 1981; Swenson and Wahr, 2002]. The decorrelation filter has to be tuned for some parameters, which are left to the user's choice. Several authors have used different parameters depending on the application of the GRACE data [Chambers, 2006; Chambers and Bonin, 2012; Chen et al., 2007; Duan et al., 2009]. Despite the popularity of the Gaussian filter, the filtering process can be improved replacing it by an anisotropic filter that fits better the noise of the data [Chen et al., 2006; García-García et al., 2010; Zhang et al., 2009].

From time to time, the procedure to estimate the SC is improved and new sets of SC are released by the different agencies. In autumn 2012, a new release of GRACE data was published, called RL05. This new release presents less noise than previous releases due to the improvement in the knowledge of alignments between the star camera, accelerometer, and K-band ranging system for Level-1B data, and updated mean gravity field, ocean tide, pole tide and de-aliasing models for Level-2 processing. Therefore, the parameters of the decorrelation filter must be tuned again. Chambers and Bonin [2012] optimized those parameters for ocean applications of the RL05 of GRACE data. In this study the choice of optimal parameters is explored for global applications of the same data set, extending the work that Duan et al. [2009] did for the RL04 GRACE data. The two-step filter is also analysed. The optimal radius of the Gauss filter is studied, as well as the application of an alternative anisotropic filter [Zhang et al., 2009].

## 4.2 Data description and methodology

The level 02 RL05 GRACE data from CSR, GFZ and JPL are used in this study[1]. Data consists of monthly sets of SC spanning from 2004/01 to 2011/12 (except GFZ that starts in 2004/02), with missing values in 2011/01, and 2011/06. During the last months, some components of the GRACE satellites were disconnected in order to minimize the battery problems, and to extend the life of the mission as much as possible. The $C_{20}$ coefficient is

[1] http://podaac.jpl.nasa.gov/gravity/grace

usually replaced by an estimate from Satellite Laser Ranging [Cheng and Ries, 2007]; it is excluded from the analysis. As far as we are interested in the variability of the geopotential, the mean value of the whole period is subtracted.

Assuming that the gravity variations are produced by mass variations on the surface of the Earth (such as the water mass transport within the water cycle, the biggest mass variations of the Earth in the intra-annual timescale), the surface mass variation, $\sigma$, in terms of water thickness equivalent (WTE) can be uniquely determined as:

$$\sigma(\theta,\lambda,t) = \frac{a\rho_E}{3}\sum_{l=0}^{\infty}\sum_{m=0}^{l}\frac{(2l+1)}{1+k'_l}P_{lm}\cos(\theta)[C_{lm}(t)\cos(m\lambda)+S_{lm}(t)\sin(m\lambda)] \quad (4.1)$$

[Chao, 2005; Wahr et al., 1998], where $(\theta,\lambda,t)$ = (colatitude, longitude, time), $a$ and $\rho_E$ are the equatorial radius and the mean density of the Earth, $k'_l$ is the degree-$l$ load Love number, $P_{lm}$ is the $4\pi$-normalized associated Legendre function of degree $l$ and order $m$ and $C_{lm}(t)$ and $S_{lm}(t)$ are the monthly GRACE SC.

Swenson and Wahr [2006] found, for a fixed order, a correlated error for the SC of even and odd degrees. They proposed a decorrelation filter that, for any SC of even (odd) degree, removes a polynomial fitted to some of the adjacent SC of even (odd) degree, which define a moving window. However, the degree of the polynomial or the length of the window was not specified and must be selected by the users. Besides, a portion of low degree and order SC is usually unfiltered, which must also be chosen by the users. An analysis of several configurations of the filter can be found in Duan et al. [2009], as those made (but not published) by Swenson and Wahr [2006], by Chambers [2006] for ocean applications and by Chen et al. [2007] to study the 2004 Sumatra earthquake.

Duan et al. [2009] presented a configuration of the filter similar to Swenson and Wahr [2006]. The idea is filtering stronger where the noise is higher, which can be achieved by increasing the order of the fitting polynomial or reducing the length of the window as the noise increase. They fixed the polynomial degree to 2 and vary the length of the window, $\omega$, accordingly to,

$$\omega = max\left\{Ae^{-\frac{[(1-\gamma)m^p+\gamma l^p]^{\frac{1}{p}}}{k}}+1,5\right\} \quad (4.2)$$

where $l$ and $m$ are the degree and order, respectively, of the SC to be filtered, which is located in the center of that window; and $A, k, \gamma$ and $p$ are the parameters to be fixed, which

define the filter itself. Fig. 4.1 shows, for each degree and order, the length of the associated window accordingly to eq. 4.2 for a selection of parameters. They are clustered in bands, where number, width, slope and curvature are defined by $A$, $k$, $\gamma$ and $p$, respectively. The width of the window decreases (increases) as $A$ or $k$ decreases (increases), which would make the filter stronger (weaker).

The minimum length of the window is fixed to 5 to retain some information after subtracting the polynomial of degree 2. In order to keep the SC to be filtered in the center of the window, the length of the latter is rounded to the nearest odd number. So, the polynomial of degree 2 to be subtracted from the SC of degree $l$ and order $m$, $C_{lm}$ and $S_{lm}$, will be fitted to, $C_{l-2\alpha,m}$, ... , $C_{l-2,m}$, $C_{l,m}$, $C_{l+2,m}$, ... , $C_{l+2\alpha,m}$ , and $S_{l-2\alpha,m}$, ... , $S_{l-2,m}$, $S_{l,m}$, $S_{l+2,m}$, ... , $S_{l+2\alpha,m}$, respectively, where $\omega = 2\alpha + 1$. Only in the case that $l$ is close to the maximum degree available in the data, or to the order $m$, the window is not centered in $C_{lm}$ and $S_{lm}$.

Note that the decorrelation filter has been applied in a different way by Chambers [2006], Chambers and Bonin [2012] and Chen et al. [2007], who, for a fixed order, fitted and subtracted a single polynomial for all the SC of even or odd degree.

The low degree and order SC are less noisy, and for that reason are not usually filtered by the decorrelation filter. Based in a trial and error procedure, Chambers [2006] left unfiltered the SC with degree and order lower than 7 for RL02 GRACE data, and lower than 11 for RL04 GRACE data[1]. Chen et al. [2007] left unfiltered the SC of degree and order below 5 for RL04 GRACE data. On the other hand, Duan et al. [2009] chose the unfiltered SC based in the calibrated SD provided by the agencies of the RL04 GRACE of one single month (as all the months look similar). They fit a curve to a SD value close to 1 $(\times 10^{12})$ and left unfiltered the SC below that curve. For RL05 GRACE it is expected that the SD decrease with respect to former releases, and then the unfiltered portion of SC should be increased. For example, Chambers and Bonin [2012] showed that leaving unfiltered the SC with degree and order lower than 15 improves the statistics when comparing GRACE with ocean models. We will explore the influence of the unfiltered SC including an extra parameter, $l$, in the filter. Then, for each degree $l$ we define a curve going from (degree, order) = $(l, 0)$ to (degree, order) = $(m, m)$ that fits the SD in fig. 4.2. For example, for $l = 38$ the value of $m$ is 11. Then, we left unfiltered the SC below that curve. In RL05, the calibrated SD are only available for GFZ GRACE data.

[1]http://grace.jpl.nasa.gov/files/GRACE-dpc200711RL04.pdf

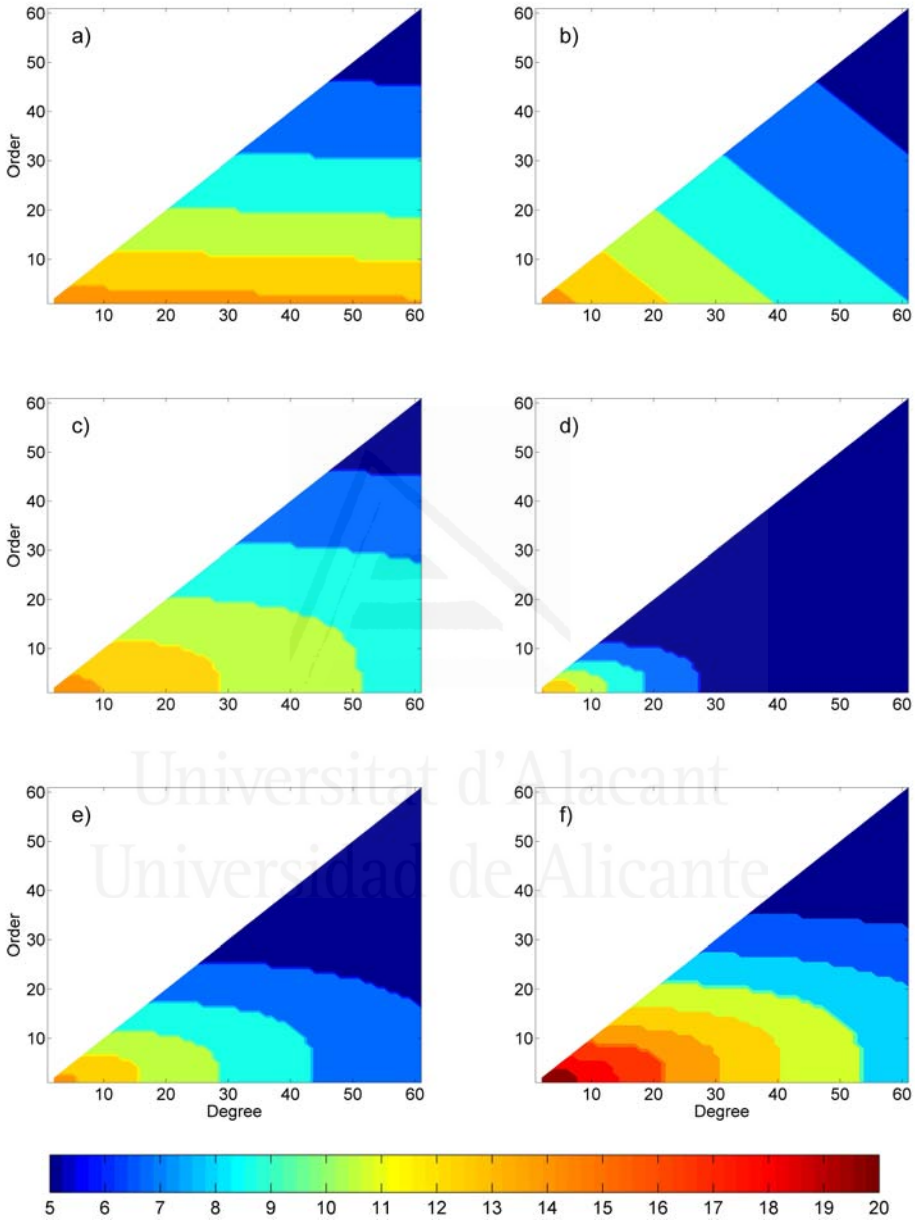


**Figure 4.1:** Length of the window accordingly to eq. 4.2 for each degree and order, and for different parameters configurations: (a) $A = 14, k = 44, \gamma = 0.04, p = 1$; (b) $A = 14$, $k = 44, \gamma = 0.5, p = 1$; (c) $A = 14, k = 44, \gamma = 0.04, p = 3.4$; (d) $A = 14, k = 10$, $\gamma = 0.04, p = 3.4$; (e) $A = 14, k = 24, \gamma = 0.04, p = 3.4$; (f) $A = 21, k = 24, \gamma = 0.04$, $p = 3.4$.

Universitat d'Alacant
Universidad de Alicante

We use the time average for the whole period of the formal (not calibrated) SD of the SC from GFZ and JPL data (they are not available for CSR data). Fig. 4.2 shows the SD of the JPL GRACE data, which is similar to those from GFZ, and it is expected to be similar to those from CSR, as far as it was in previous releases.

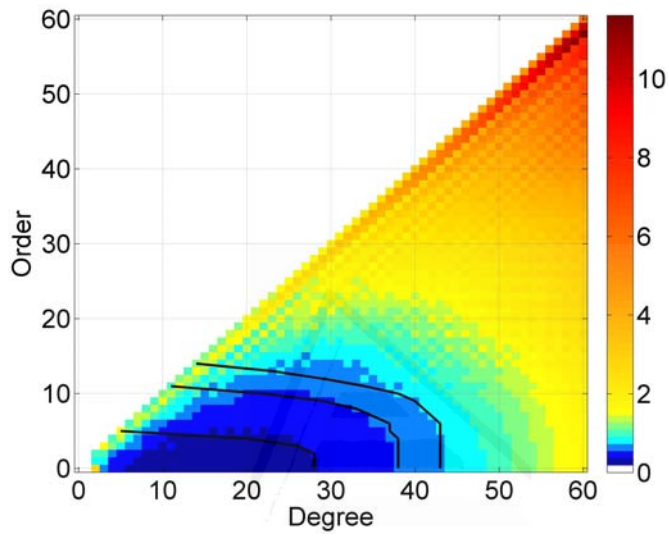


**Figure 4.2:** Time average of the formal (not calibrated) SD (scaled by $\times 10^{12}$) of the JPL RL05 GRACE SC. Black lines represent the curves delimiting the unfiltered SC for $l = 28, 38$ and $43$.

Universitat d'Alacant
Universidad de Alicante

The width of the moving window must vary accordingly to the noise of the data. So, the color bands shown in fig. 4.1 should be aligned with those in fig. 4.2. Following that criteria it is easy to fix the parameters $\gamma = 0.04$ and $p = 3.4$. Then, the filter will be defined once the values of $A$, $k$ and $l$ are determined. We implement several experiments for a wide rank of parameters in order to define an optimal filter for global applications. In particular, GRACE and synthetic GRACE data (see below) are filtered with parameters: $A$ from $10$ to $24$; $k$ from $20$ to $44$ and $l$ from $10$ to $45$. In order to reduce the high computational cost of the experiments, the parameters $A$ and $k$ vary $2$ by $2$, and $l$ does $5$ by $5$ from $10$ to $30$, and $1$ by $1$ from $30$ to $45$.

For the following experiments we will need synthetic GRACE data, which consist of global grids with OBP over the oceans and with terrestrial water storage fields over land. The former is estimated from the Estimating the Circulation and Climate of the Ocean

(ECCO) [Stammer et al., 2002][1] model version $kf080$, and the latter is estimated from surface water storage grids from Global Land Data Assimilation Systems (GLDAS) model [Rodell et al., 2004][2]. These grids are estimated from the integration of four-layer soil moisture, snow equivalent height and canopy water. As the hydrologic model has no data over Greenland and Antarctica, these regions are avoided in the comparison with GRACE. In order to make the synthetic data more realistic an estimate of the Post Glacial Rebound (PGR) from Paulson et al. [2007] have been added to the grids. The synthetic data have been reduced to $1^\circ \times 1^\circ$ monthly grids for the period 2004/01 to 2011/12, and transformed to millimetre of WTE $(kg \cdot m^2)$. The mean value of the whole period is removed from the signal. The points covered neither by GLDAS nor ECCO are set to zero. When the filter is applied to the synthetic data, the degree-1 and the $C_{20}$ coefficients are set to zero.

## 4.3 First-Step Filter

### 4.3.1 Linear trends

When filtering the data, the noise is reduced jointly with some of the sought geophysical signals. On the one hand, if the filter is very weak the noise will dominate the signal. On the other hand, if the filter is very strong the geophysical signal will be too attenuated. In some place between these two opposite cases resides the optimal filtering level. In order to find the latter, we explore the strategy used by Duan et al. [2009] to select the parameters of the filter for RL04 GRACE data, who found the values $A = 30, k = 15, \gamma = 0.1, p = 2$ for CSR data and $A = 30, k = 15, \gamma = 0.1, p = 3$ for JPL data.

The selection is based on the study of the rms of the lineal trend of surface mass grids from GRACE and synthetic data. The unfiltered GRACE data present too high linear trend values, with an associated high rms, due to noise influence. So, the reduction of such trends (and associated rms) would indicate a reduction of the noise. However, an excessive reduction would mean an undesirable attenuation of the geophysical signals. In order to estimate the latter, the filter is applied to noise-free data based on models, the synthetic data. The perfect filter should not reduce the trends of noise-free data. The optimal filter should minimize the rms of the global linear trend in GRACE data, and maximize them in synthetic data. In practice, the rms of the filtered GRACE and synthetic data are normalized

[1] http://www.ecco-group.org/products.htm
[2] http://disc.sci.gsfc.nasa.gov/hydrology/data-holdings

with respect to their rms prior to filtering. This is made to reduce the influence of the high values produced by very noisy GRACE data. After normalization, the linear trend rms from synthetic data present higher values than those from GRACE data. It makes sense since the filter produces attenuation of the signal in both data, but noise reduction only in GRACE data. Therefore, the optimal filter should maximize the difference between the linear trends rms of synthetic and GRACE data. Fig. 4.3 shows the latitude weighted rms of the linear trends for synthetic, and the three agencies GRACE data, and fig. 4.4 shows their differences.

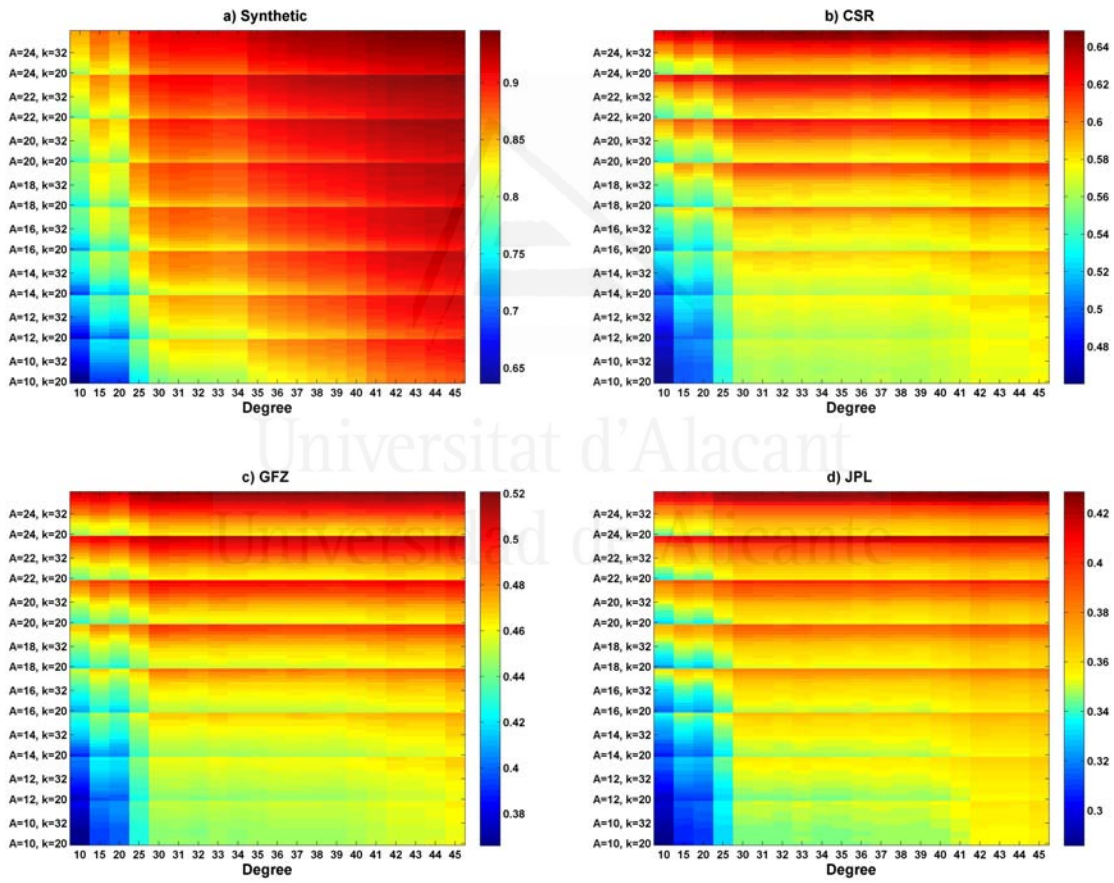


**Figure 4.3:** The rms of the linear trends from (a) synthetic, and GRACE data: (b) CSR; (c) JPL and (d) GFZ. Each value is estimated using a decorrelation filter with different combination of $A$ (from 10 to 24, 2 by 2), $k$ (from 20 to 44, 2 by 2) and $l$ (5 by 5 from 10 to 30, and 1 by 1 from 30 to 45). Units: Percentage with respect to rms prior filtering.

Universitat d'Alacant
Universidad de Alicante

Each value is estimated using a different combination of $A$, $k$ and $l$. The parameter l shows de greatest gradient, with optimal values between 35 and 45, and several combinations of $A$ and $k$. For example, for $CSR$ and $l = 38$, the greatest differences can be reached around $(A, k) = (24, 20)$. This experiment gives an idea about the importance of the parameter $l$, and justifies the finer resolution between 30 and 45. However, the choice of the parameters is too vague and further analyses are needed.

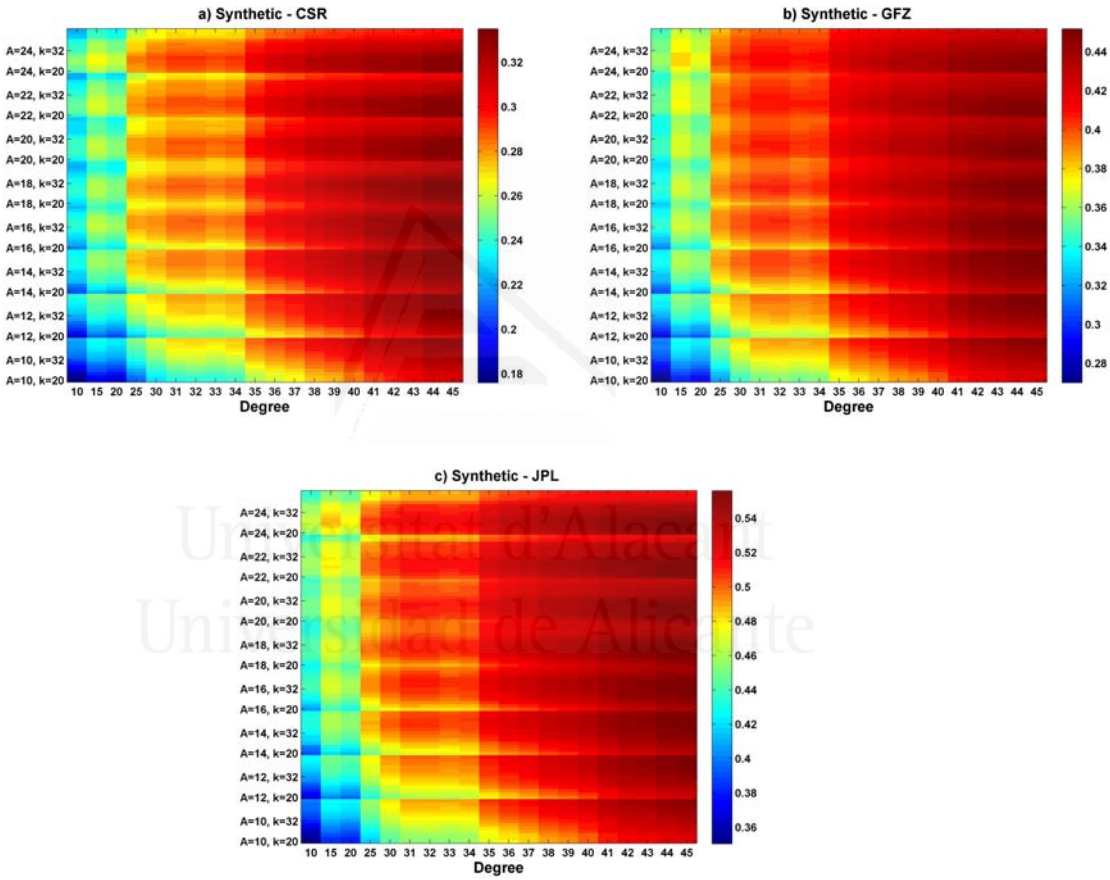


**Figure 4.4:** Differences between the rms of the linear trends from synthetic and GRACE data: (a) CSR, (b) GFZ and (c) JPL. Decorrelation filter applied to GRACE and synthetic data prior subtraction. Units: Percentage with respect to rms prior filtering.

### 4.3.2 GRACE versus synthetic data

GRACE and synthetic data are compared, but some preliminary corrections must be made to the GRACE data. First, as synthetic data represent OBP over the ocean, GRACE should represent the same. It is reached in two steps: (1) the atmospheric and oceanic corrections applied to GRACE over the ocean, the GAD product, is added back and (2) for each month the global ocean Sea Level Pressure (SLP) (from NCEP) average is subtracted from the ocean points in GRACE. Note that the GAD and SLP data are not filtered, so they may modify the absolute values of the linear trends experiment, but not the relative values among them, which we were interested in the previous experiment. Secondly, to make the spatial resolution comparable the synthetic grids are transformed into SC, and then back to grids only using SC up to degree $60$. In the processes the degree-$1$ and $C_{20}$ coefficients are suppressed. No filter is applied. Finally, the regions not covered by the synthetic data-Antarctica, Greenland and Artic ocean-are discarded in the analysis, and the continental leakage is reduced [Wahr et al., 1998].

Since the decorrelation filtered GRACE data are still too noisy to be compared to the unfiltered synthetic data, a Gaussian filter of $500$ km radius is also applied to the former. The Gaussian filter is defined by a radius $r$, and consists of the application of a weight, $W_l^r$, to the SC [see Swenson and Wahr, 2002, for a recursive formula]. Then, the surface mass grids are estimated as

Universitat d'Alacant
Universidad de Alicante

$$\sigma(\theta,\lambda,t) = \frac{a\rho_E}{3}\sum_{l=0}^{\infty}\sum_{m=0}^{l}\frac{(2l+1)}{1+k_l'} \times W_l^r P_{lm}\cos(\theta)[C_{lm}^*(t)\cos(m\lambda) + S_{lm}^*(t)\sin(m\lambda)] \quad (4.3)$$

where $C_{lm}^*(t)$ and $S_{lm}^*(t)$ are the SC once the decorrelation filter has been applied. Note that the only other difference with eq. 4.1 is the term $W_l^r$.

For each gridpoint the rms of the difference between filtered GRACE and unfiltered synthetic data is estimated. Fig. 4.5 shows the spatial average of these rms for different parameters of the filter. The minimum values are reached with parameters $36 \leq l \leq 39$, $10 \leq A \leq 16$ and $20 \leq k \leq 28$. Similarly, the correlation coefficient between filtered GRACE and unfiltered synthetic data is shown in fig. 4.6. The maximum correlations are reached with $38 \leq l \leq 39$, $A \sim 14$ and $20 \leq k \leq 28$ for CSR data, and with $36 \leq l \leq 40$, $10 \leq A \leq 14$ and $20 \leq k \leq 28$ for GFZ and JPL data. Therefore, for all GRACE

data sets the minimum residual and the maximum correlation is reached around the same parameters, narrowing the parameters values selected by the linear trends experiment.

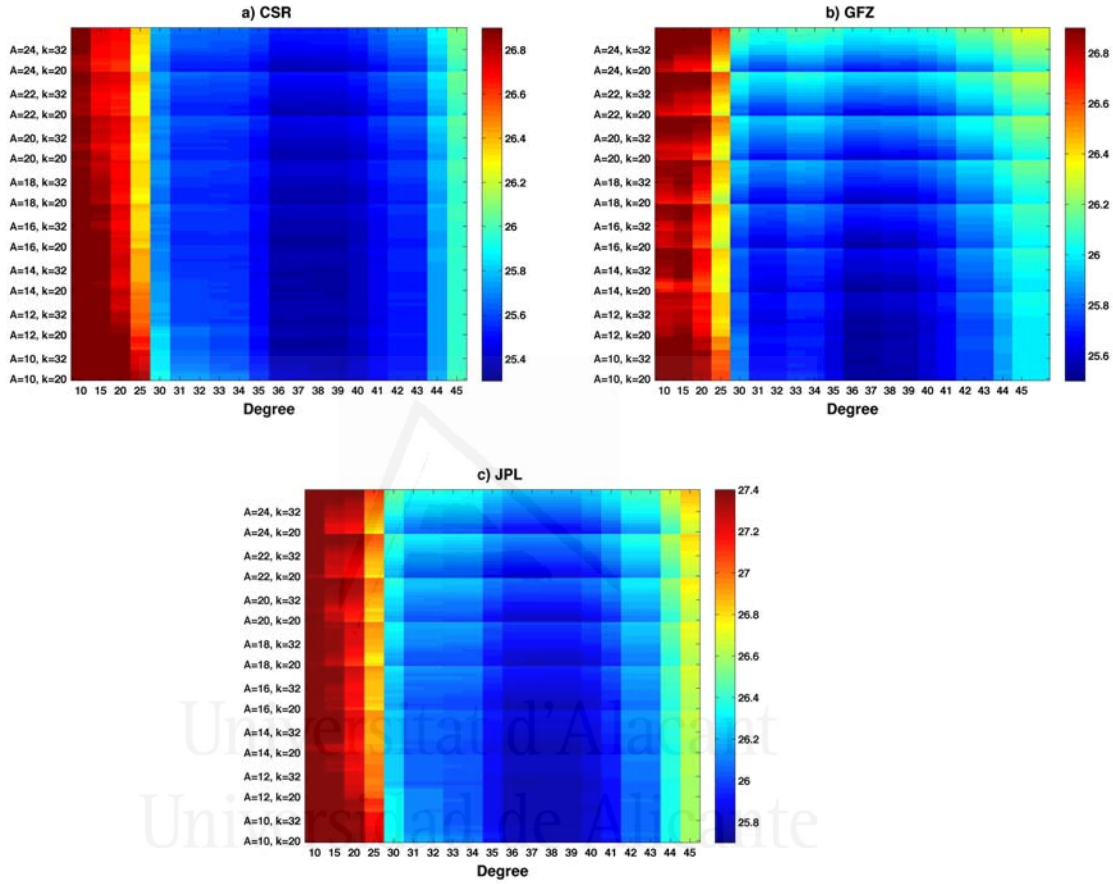


**Figure 4.5:** The rms of the differences between synthetic and GRACE data: (a) CSR, (b) GFZ and (c) JPL. Decorrelation and Gauss ($r = 500$ km) filter applied to GRACE data. Synthetic data truncated at degree 60. Continental leakage reduced. Units: $mm$.

It is worthwhile to remark that the minimum difference between GRACE and synthetic do not necessary define the optimal filter. The reason is that GRACE measures signals that hydrological models generally do not account for, as for example groundwater, river storage or water extraction from aquifers. Besides, during the filtering process the signal amplitude is attenuated and it must be restored to approximate the real signal,which can be done for regional averaged signals [e.g. Velicogna and Wahr, 2006] or gridpoints [Landerer and Swenson, 2012]. In the restoring amplitude process the differences with the synthetic data are not necessarily reduced. On the other hand, the correlation coefficient does not

depends on whether the amplitude of a time-series is restored, since the restoring factor is a constant multiplying the whole time-series.

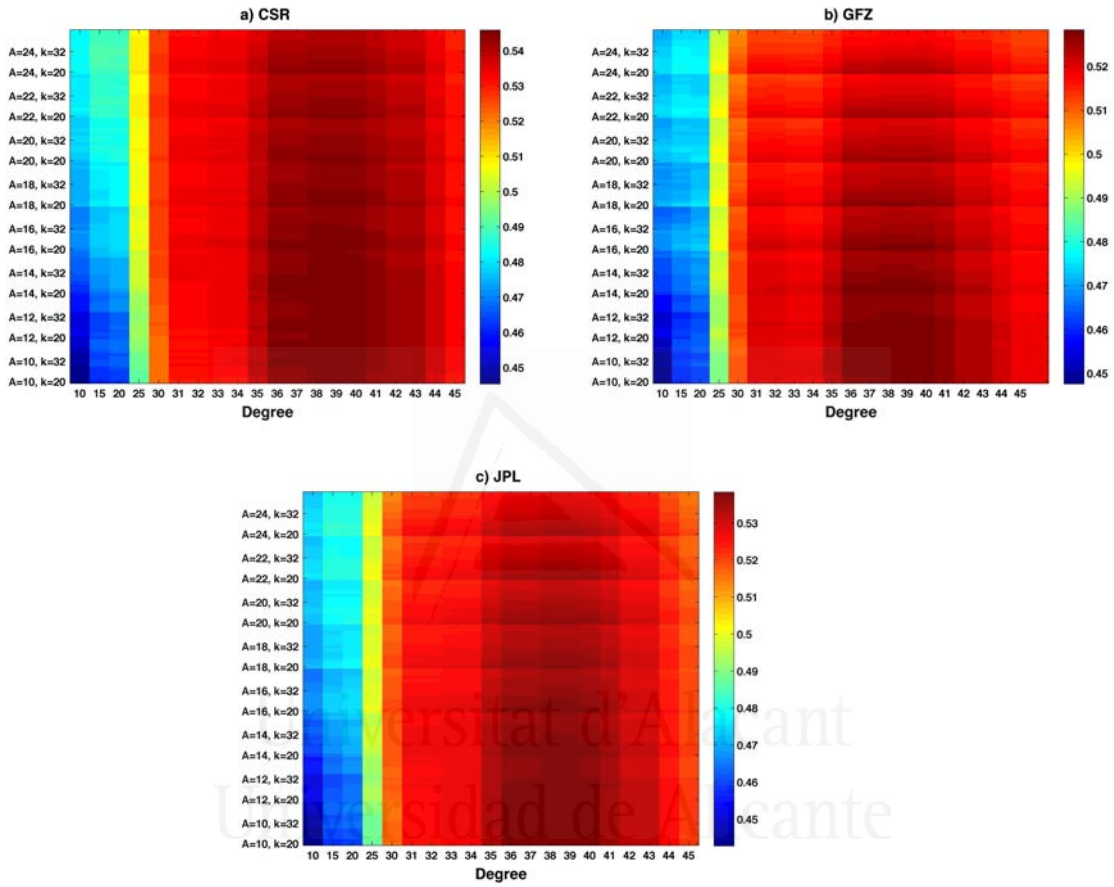


**Figure 4.6:** Correlation coefficients between synthetic and GRACE data: (a) CSR, (b) GFZ and (c) JPL. Data processing as in fig. 4.5.

The annual amplitude has been estimated for each gridpoint of GRACE and synthetic data. Fig. 4.7 shows the correlation coefficients between them. The maximum correlation is reached for the greatest values of $A$, $k$ and $l$, that is, for the weakest version of the filter. It makes sense since the estimation of the annual amplitudes acts as a filter itself. On the other hand, fig. 4.8 shows that a stronger version of the filter with lower $l$ is needed to reach the maximum correlation of the non-seasonal signals (no linear trend nor annual amplitude). It means that a modification of the parameters must be considered depending on the sought-after signal.

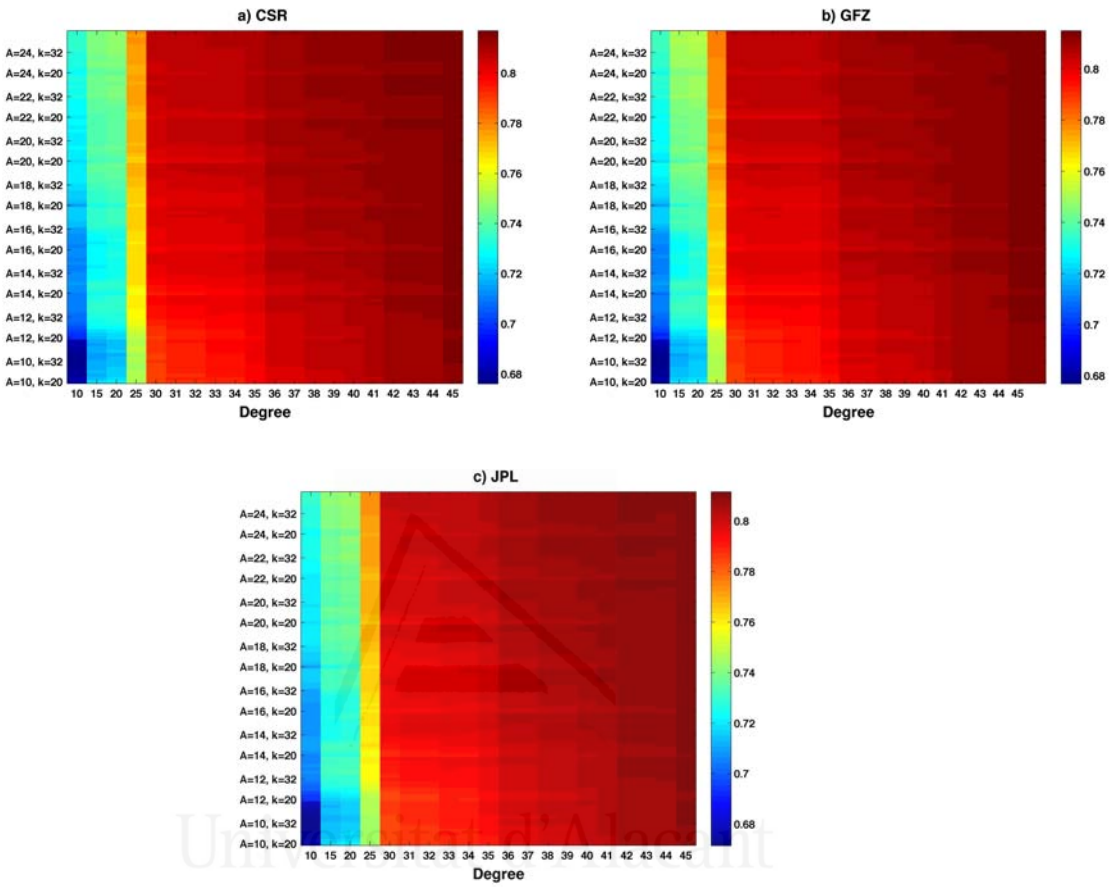


**Figure 4.7:** Correlation coefficients between the annual amplitudes of synthetic and GRACE data: (a) CSR, (b) GFZ and (c) JPL. Data processing as in fig. 4.5.

### 4.3.3 Contienents versus ocean

The optimal filter can also be explored using the criteria that Chen et al. [2007] defined for tuning their anisotropic filter. The idea is based on the fact that the surface mass variability is stronger in the continents than in the oceans. The ratio of variability can be measured as the quotient of the latitude weighted rms of the continental and oceanic signals. On the one hand, if some noise were added to the SC, spurious variability would be introduced in both continents and oceans. On the other hand, if the SC were attenuated the variability in both continents and oceans would be reduced. In any case, the ratio of variability between the continents and the ocean would be reduced. So, the maximum of such ratio would represent the maximum of signal-to-noise ratio,which should be obtained using the optimal filter.

Fig. 4.9 shows the values of that ratio for several decorrelation filters, as well as a Gaussian filter of 500 km, for data from the three agencies. In order to reduce the leakage of the continental signal only the ocean points farther than 500 km from the coast are included. The maximum ratios are obtained with $38 \leq l \leq 43$, $14 \leq A \leq 16$, and any $k$ for CSR data, and with $38 \leq l \leq 41$, $12 \leq A \leq 14$ and any $k$ for GFZ and JPL data.

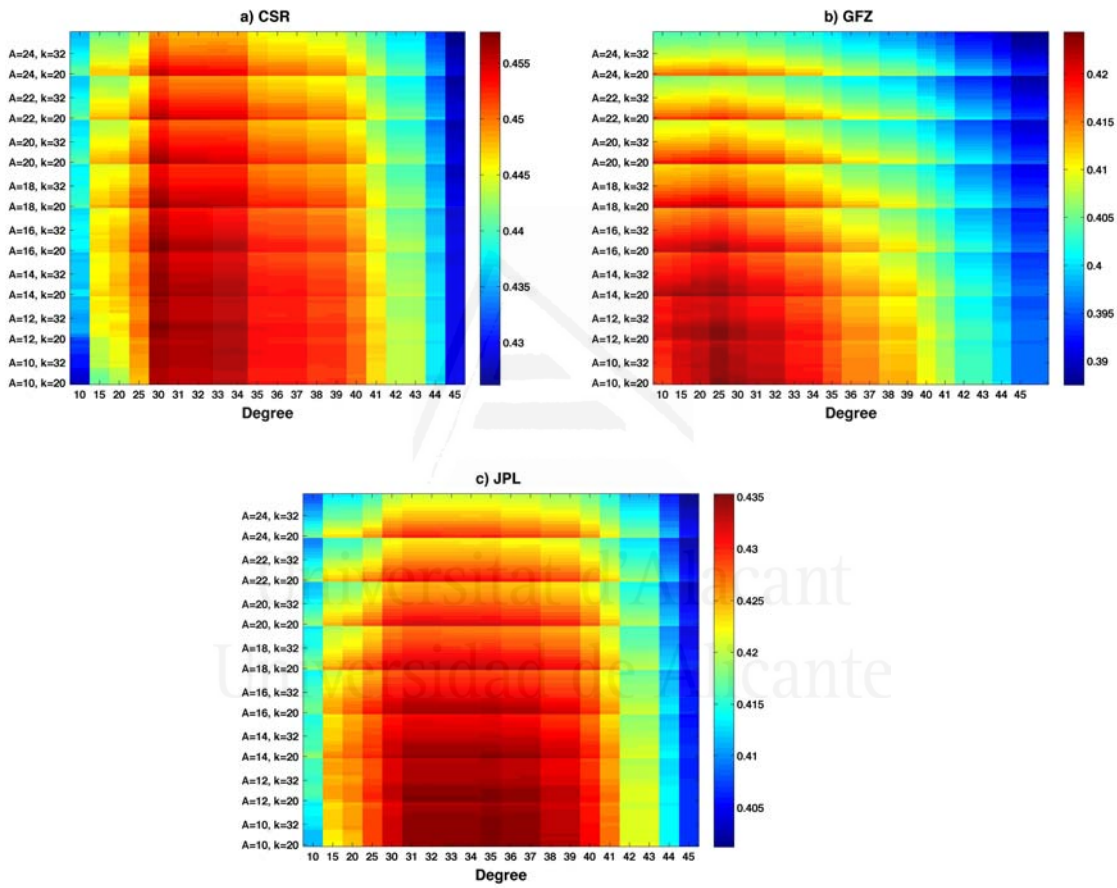


**Figure 4.8:** Correlation coefficients between the non-seasonal signals from synthetic and GRACE data: (a) CSR, (b) GFZ and (c) JPL. Data processing as in fig. 4.5.

### 4.3.4 Parameters selection

Accordingly to the previous experiments some conclusions can be made: (1) the three agencies show a similar noise distribution, but not identical; (2) the portion of unfiltered SC is the most critical parameter; (3) as the latter has increased from RL04 to RL05, it can

be inferred that RL05 data are less noisy than RL04 and (4) the optimal statistics of the experiments is not reached for a unique parameters configuration, but for all the agencies it can be reached with parameters values close to $l = 38$, $A = 14$ and $k = 24$. In Sections 4.3.2 and 4.3.3, a Gaussian filter with a radius of 500 km was also applied to GRACE data. In order to check whether that choice could vary the optimal parameters of the decorrelation filter, the same analysis was implemented with a radius of 300 km. In that case, the obtained results were quite similar.

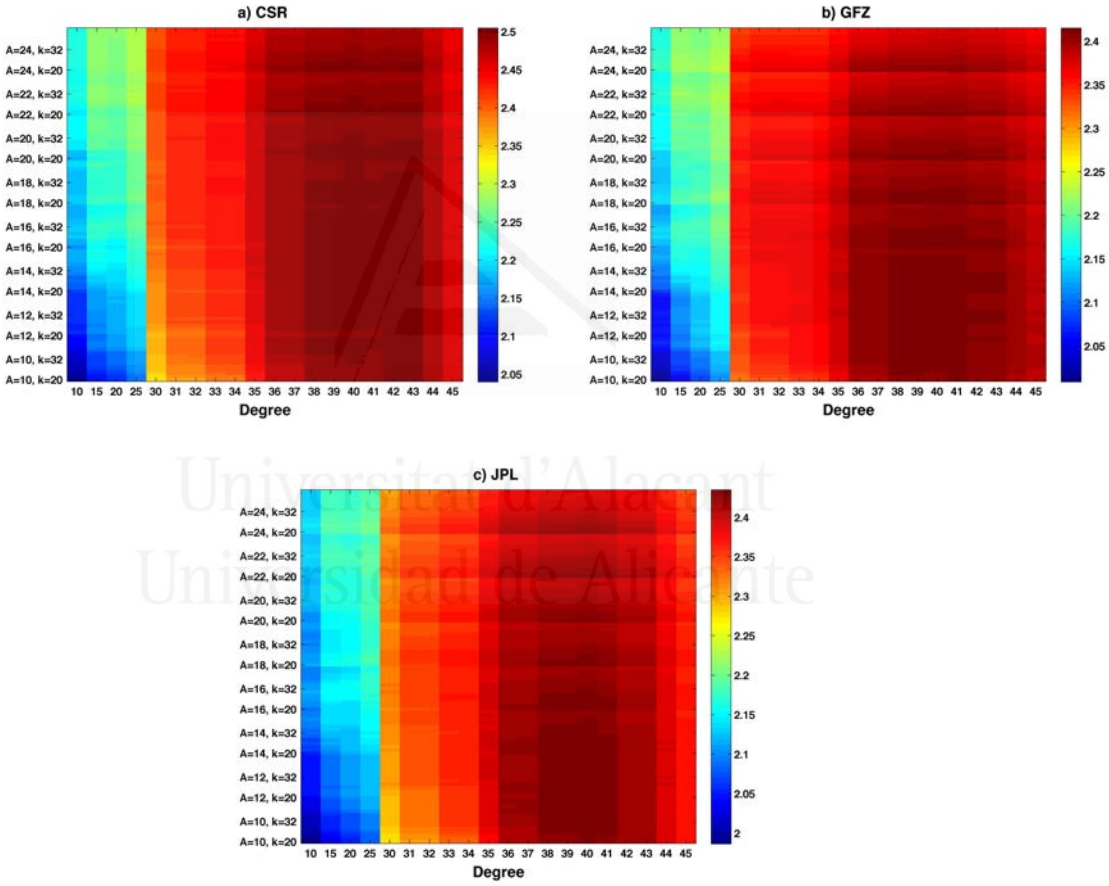


**Figure 4.9:** Ratio of variability between the continents and the ocean: (a) CSR, (b) GFZ and (c) JPL. Decorrelation and Gauss ($r = 500$ km) filter applied to GRACE data. Ocean points closer to 500 km to the continents are avoided.

Universitat d'Alacant
Universidad de Alicante

## 4.4 Second-Step filter

Once the decorrelation error filter is applied, a second filter must be applied, which generally is the isotropic Gaussian one. The parameter $r$ defining the filter approximately fixes the spatial resolution of the filtered grids. Fig. 4.10 shows the weights $W_r^l$ of the Gaussian filter for different radius. Note that the weight of high degree SC decreases as $r$ increases, that is, the spatial resolution decreases as $r$ increases. The parameter $r$ is usually fixed with a visual trial and error procedure looking for grids without north-south stripes. However, an optimal $r$ could be found objectively maximizing the ratio of variability between continents and oceans as in Section 4.3.3 [Chen et al., 2007]. Fig. 4.11 shows the evolution of this ratio, which has been estimated only including the ocean points farther than 500 km from the coast to reduce the leakage from the continental signal. The maximum ratio, and then the optimal Gaussian filter, is obtained with $r = 380$ km for CSR, $r = 420$ km for GFZ and $r = 400$ km for JPL. The maximum ratio in CSR and GFZ data is $\sim 3.5$, while it is 3.3 for JPL data.

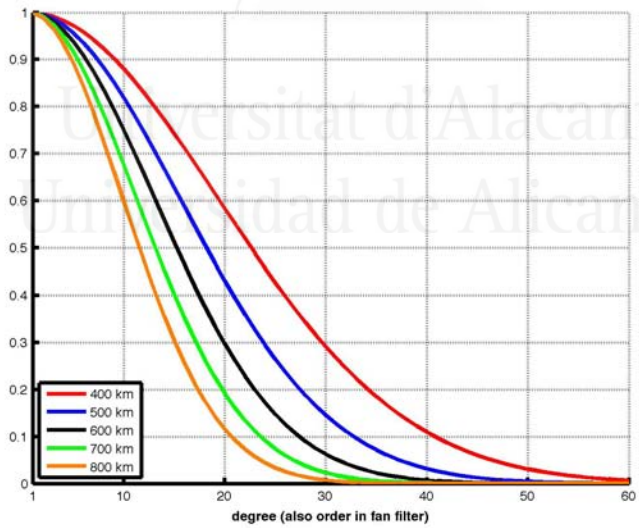


**Figure 4.10:** Weights of the Gaussian filter for different radius: $r = 400$ km (red line), $r = 500$ km (blue line), $r = 600$ km (black line), $r = 700$ km (green line) and $r = 800$ km (orange line).

Note that the radius $r$ roughly represents the spatial resolution of the WTE maps. However, the resolution is limited to $20000/N$ km, where $N$ represents the truncation degree

of the SC. So, if $N = 40$ and $N = 60$ a maximum spatial resolution of 500 and $\sim$ 333 km could be reached, respectively. For that reason, the reported values of $r$ must be interpreted carefully.

In order to estimate the error of the data, the residuals of the differences between GRACE and synthetic data are explored as in Section 4.3.2, but using the optimal $r$ of each agency. Then, the standard deviation of the residual is estimated for each gridpoint. Fig. 4.12 shows the residual for the CSR, GFZ and JPL data using SC up to degree 60,which are very similar. The global latitude-weighted averaged of the residuals are 26.1 mm for CSR and GFZ, and 26.5 mm for JPL. The largest signal is observed around Greenland,which is not modeled by the hydrological model, and in the Amazon, where the surface waters are neither modeled. When these two regions are avoided the residuals are reduced to 24.6 mm for CSR and GFZ and 25.0 mm for JPL. Besides, when the continental leakage is reduced, the residual drops around 1.5 per cent. In any case, remember that noise-free GRACE data are not expected to minimize the residual.

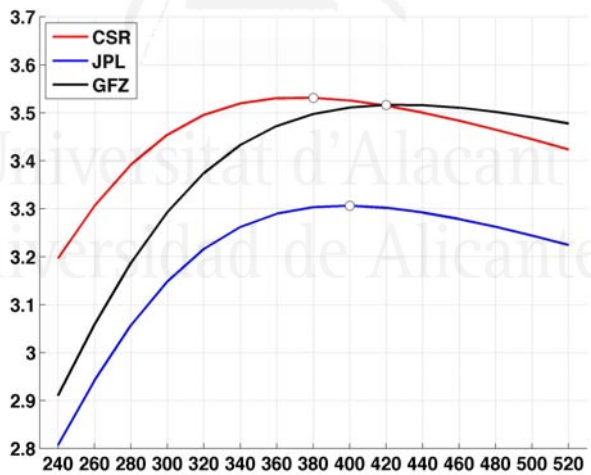


**Figure 4.11:** Ratio of variability between continents and ocean for GRACE data from: (a) CSR, (b) JPL and (c) GFZ, as a function of the radius $r$ of the Gaussian filter. GRACE data have been previously decorrelated. Ocean points closer to 500 km to the continents are avoided.

The two-step filtering process can be improved replacing the isotropic (only degree dependent) Gauss filter by an anisotropic (degree and order dependent) filter. The Gaussian filter applies weights to the SC that decreases as the degree increases. The fan filter is a combination of two Gaussian filters, one applied to the degrees, and another to the orders

[Zhang et al., 2009]. Then, the fan filter can be defined with two radii, one for the degrees, $r_l$, and another for the orders, $r_m$. In this case, the surface mass grids are estimated as

$$\sigma(\theta,\lambda,t) = \frac{a\rho_E}{3}\sum_{l=0}^{\infty}\sum_{m=0}^{l}\frac{(2l+1)}{1+k'_l} \times W_l^{r_l}W_m^{r_m}P_{lm}\cos(\theta)[C^*_{lm}(t)\cos(m\lambda)+S^*_{lm}(t)\sin(m\lambda)] \quad (4.4)$$

where the weights $W_l^{r_l}$ and $W_m^{r_m}$ depends on the degree $l$ and order $m$, respectively. Note that the only difference with eq. 4.3 is the term $W_m^{r_m}$.

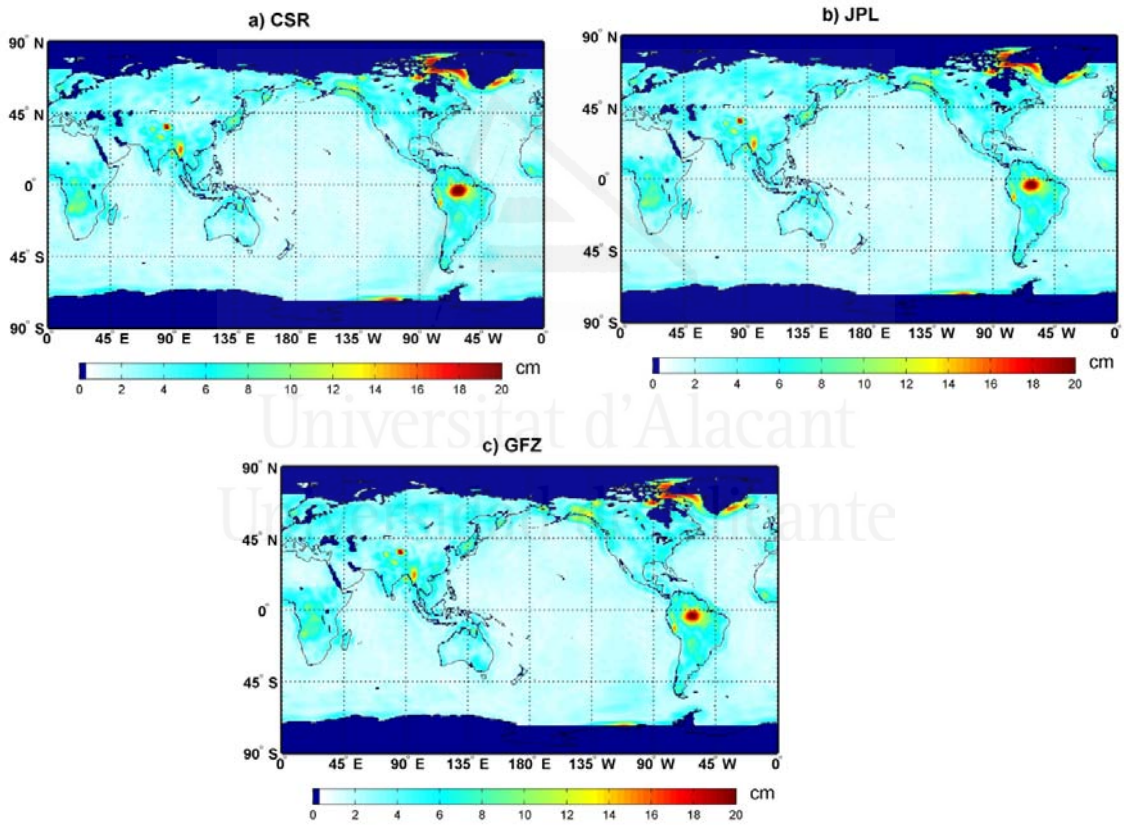


**Figure 4.12:** Standard deviation of the residual between synthetic and filtered GRACE data: (a) CSR, (b) JPL and (c) GFZ. Decorrelation and Gauss ($r = 380$ km for CSR, $r = 420$ km for GFZ and $r = 400$ km for JPL) filter applied to GRACE data. Synthetic data truncated at degree 60. Continental leakage reduced.

In the Gauss filter the radio $r$ roughly represents the spatial resolution in any direction, while $r_l$ and $\sqrt{2}\cdot r_m$ represent the north-south and east-west spatial resolution, respectively.

Similarly to the Gauss filter, the optimal radii of the fan filter are explored to maximize the ratios of variability between continents and oceans. Fig. 4.13 shows that the largest ratios are reached with radii close to $(r_l, r_m) = (290, 690)$ km for CSR, $(r_l, r_m) = (310, 820)$ km for GFZ and $(r_l, r_m) = (290, 640)$ km for JPL. The obtained ratios are larger with the fan filter than with the Gauss filter. Although, the residuals of the differences between GRACE and synthetic data look similar (not shown), their average is $25.4$ mm for CSR, $25.3$ mm for GFZ and $26.1$ mm for JPL. When the points from Amazon and around Greenland are excluded, the residuals are reduced to $23.9$ mm for CSR and GFZ and $24.6$ mm for JPL. In any case, the residuals are smaller than using the Gauss filter. Then, the fan filter seems to be more appropriated than the Gauss filter as second-step filter.

## 4.5 Discussion

GRACE data must be filtered before use to reduce some noise in high degree and order SC. One of the most popular filters is a two-step filter: (1) decorrelation filter and (2) Gauss filter. Both filters must be adapted to the noise level of the data. While the Gauss filter only depends on one parameter, the decorrelation filter depends on several parameters producing multiple combinations. In this study we have analyzed the parameters configurations of the decorrelation filter for the RL05 of GRACE data that optimize several statistics for global applications. These parameters are close to $l = 38$, $A = 14$ and $k = 24$, as well as $\gamma = 0.04$ and $p = 3.4$, for all the agencies. Besides, the application of the isotropic Gauss filter and the anisotropic fan filter as second-step filter has been analysed. The best results for the Gauss filter are obtained with $r = 380$ km for CSR, $r = 420$ km for GFZ and $r = 400$ km for JPL, while for the fan filter are obtained with values close to $(r_l, r_m) = (290, 690)$ km for CSR, $(r_l, r_m) = (310, 820)$ km for GFZ and $(r_l, r_m) = (290, 640)$ km for JPL.

Table 4.1 summarizes the analysed statistics of the reported filters, as well as those using parameter configuration from previous studies. In order to make the different filters comparable, the calculation are made using SC up to degree 40 as in Chambers and Bonin [2012], and up to degree 60 as in Duan et al. [2009] and Chen et al. [2007]. In both cases, and for any agency, the parameters estimated in this study show: (1) smaller rms values in the linear trends of GRACE data; (2) smaller differences and larger correlation with the synthetic data; (3) larger variability ratios between continents and ocean signals,

which are reached with (4) smaller radius in the Gaussian filter. From these results it can be inferred that the filtering parameters estimated in this study present a more optimal compromise between noise elimination and geophysical signals preservation, and a better spatial resolution. The result is not surprising since Duan et al. [2009] proposed a filter for the RL04 data, and Chambers and Bonin [2012] for ocean applications. When regarding to the ocean the latter filter produces a rms of the differences $\sim$ 16 mm for the three agencies, which is similar to the value obtained using the reported parameters and Gauss filter. The global statistics using the fan filter are summarized in table 4.2, and they improve those from the Gaussian filter. As the Gauss and the fan filter are both easily implemented, the latter should be consider as second-step filter.

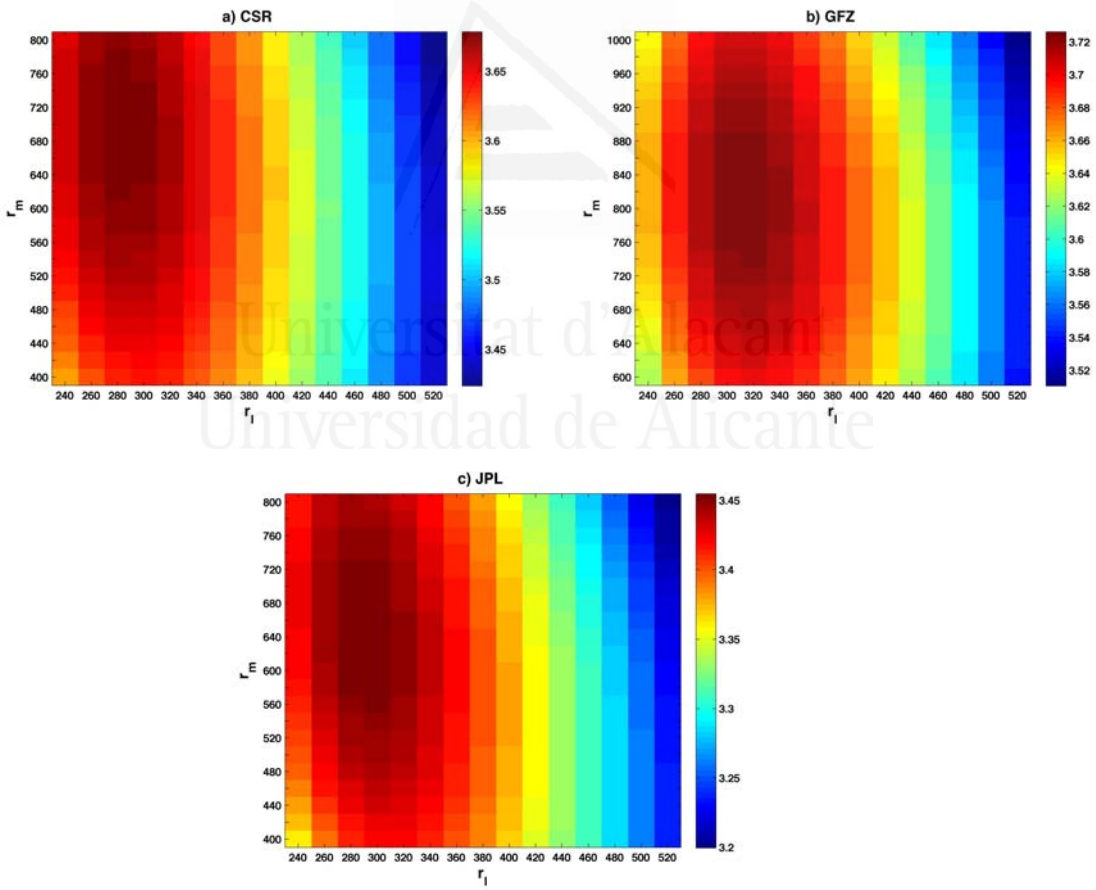


**Figure 4.13:** Ratio of variability between continents and ocean for GRACE: (a) CSR, (b) JPL and (c) GFZ, as a function of the radii $r_l$ and $r_m$ of the fan filter. GRACE data have been previously decorrelated. Ocean points closer to 500 km to the continents are avoided.

The selection of the parameters, and hence the design of the two-step filter depends on the models used in the synthetic data. However, the study of the variability between continents and oceans does not depend on the model and gives an approximation of the filter. Then, the results are not expected to vary significantly as the models change.

This study complements the one done by Chambers and Bonin [2012] for oceanic applications, and it could be of interest for GRACE users that would like to continue processing the RL05 data with the decorrelation filter.

| | | | Decorrelation | Decorrelation and Gauss filters | | | |
|---|---|---|---|---|---|---|---|
| | | | Rms linear trend (mm $yr^{-}1$) | Rms differences (mm) | Correlation coeficients | Ratio contients/ocean | r(km) |
| Degree 60 | Chen et al. [2007] | CSR | 10.7 | 25.8 | 0.53 | 3.27 | 500 |
| | | GFZ | 10.8 | 25.6 | 0.52 | 3.27 | 600 |
| | | JPL | 11.0 | 26.3 | 0.52 | 2.98 | 540 |
| | Duan et al. [2009] | CSR | 10.8 | 25.8 | 0.53 | 3.32 | 490 |
| | | GFZ | - | - | - | - | - |
| | | JPL | 11.5 | 25.9 | 0.53 | 3.03 | 540 |
| | This study | CSR | 9.7 | 26.1 | 0.54 | 3.53 | 380 |
| | | GFZ | 9.6 | 26.1 | 0.52 | 3.52 | 420 |
| | | JPL | 9.6 | 26.5 | 0.53 | 3.31 | 400 |
| Degree 40 | Chambers and Bonin [2012] | CSR | 9.2 | 26.3 | 0.52 | 3.35 | 430 |
| | | GFZ | 9.0 | 25.8 | 0.52 | 3.37 | 520 |
| | | JPL | 9.0 | 26.6 | 0.52 | 3.09 | 480 |
| | This study | CSR | 8.9 | 26.1 | 0.53 | 3.54 | 380 |
| | | GFZ | 8.7 | 26.1 | 0.52 | 3.52 | 420 |
| | | JPL | 8.7 | 26.4 | 0.53 | 3.32 | 400 |

**Table 4.1:** For the three agencies of GRACE data: rms of linear trends from decorrelation filtered GRACE data. The rms of the differences and correlation coefficients between GRACE (decorrelation and Gauss filters) and synthetic data. Maximum ratio of variability continents/oceans from decorrelation and Gauss filtered GRACE data, as well as the radio where the maximum is reached. For comparison purposes the maximum degree is set to 40 and 60.

| | | Decorrelation and fan filters | | | |
|---|---|---|---|---|---|
| | | Rms differences (mm) | Correlation coefficients | Ratio conti./ocean | $r_l/r_m$ (km) |
| Degree 60 | CSR | 25.4 | 0.55 | 3.68 | 290/690 |
| | GFZ | 25.3 | 0.53 | 3.73 | 310/820 |
| | JPL | 26.1 | 0.54 | 3.45 | 290/640 |
| Degree 40 | CSR | 25.3 | 0.54 | 3.70 | 290/690 |
| | GFZ | 25.3 | 0.53 | 3.75 | 310/820 |
| | JPL | 25.9 | 0.53 | 3.48 | 290/640 |

**Table 4.2:** As table 1, but fan filter is used of Gauss filter.

Universitat d'Alacant
Universidad de Alicante

*Historical methodology, as I see it, is a product of common sense applied to circumstances.*

Samuel E. Morison

CHAPTER

5

# A Cautionary Note on the Use of Running Trends as Summary Statistics for Univariate Time Series and Time Series Association

Universitat d'Alacant
Universidad de Alicante

## 5.1 Introduction

RTA is one of several methods used in climate research to analyze univariate time series and time series association. For a given time series $\{y(t)\}$ , observed at $n$ equally spaced points in time $t_1, t_2, \ldots, t_n$, RTA involves defining $n - L + 1$ overlapping time windows, $W_1, W_2, \ldots, W_{n-L+1}$, each with exactly $L$ consecutive time points $t_j, t_{j+1}, \ldots, t_{j+L-1}$, $j = 1, 2, \ldots, n - L + 1$, and then evaluating the least square estimates of the trend for each time window $W_j$. This produces a new series of length $n - L + 1$ called *running trend series*, that is used as a summary statistic of the original series $\{y(t)\}$ for further analysis.

In recent years RTA has been widely used in applied research on climate as a part of more complex time series analysis. Holgate and Woodworth [2004], for example, use

ten-year Global Mean Sea Level (GMSL) running trends (L=10) to study acceleration of GMSL from 1948 to 2002 and to obtain a GMSL reconstruction for the same period. Santer et al. [2014] use 120-month running trends (L=120) of changes in the temperature of the lower troposphere (from satellite measurements made by Microwave Sounding Units on National Oceanic and Atmospheric Administration polar-orbiting satellites) for the period 1979-2012, to analyze volcanic contributions to observed changes in warming rates.

Hamlington et al. [2014; 2013], use twenty-year running trends of Pacific Decadal Oscillation (PDO) and of Annual Mean Sean Level to study the contribution of PDO to Mean Sea level trends both globally [Hamlington et al., 2013] and regionally [Hamlington et al., 2013]. Palmer and McNeall [2014] compute ten-year running trends of the total energy in the Earth System (TE), the Global surface temperature (GST) and the total near-global Ocean heat (OHC), to investigate the relationship between these variables (the model data analyzed are multi-century pre-industrial control simulations from the Couple Model Intercomparison Project 5 (CMIP5) model archive). In the same work the authors use the correlations between running trends in TE and running trends in OHC for a range of periods (running trends of length 2-36 months are considered) to estimate the time scale on which the ocean becomes the dominant term in the planetary energy budget. Risbey et al. [2014] use fifteen-year Global mean surface air temperature (GMST) running trends evaluated using data from CMIP5 models and observations for the period 1880-2012 to study the CMIP5 models' performance (in terms of model's ability to reproduce the fifteen-year observed GMST trends).

There is no doubt that RTA might be a useful descriptive tool, but, despite its general use in applied research, precisely what it reveals about the underlying time series and time series association is unclear and, as a result, its interpretation is unclear too. In this respect a more rigorous study of the information that RTA conveys about the underlying time series and time series association would be desirable. This chapter is intended as a first step in this direction. We provide an explicit formula for the set of time series that share a given series of running trends by showing that such a set is the solution set (of dimension $L-1$) of a linear system with $n-L+1$ equations and $n$ unknowns. Such a representation allows us to clarify important aspects of strengths and limitations of running trends as summary statistics for univariate time series and time series association. The main result of this chapter, which is the explicit formula for the set of time series with a given series of running trends, is presented in section 5.2 and illustrated with an example in section 5.3.

Universitat d'Alacant
Universidad de Alicante

The worked example also serves to anticipate some important consequences that follows from the main result in section 5.2 and that we discuss in more general terms in section 5.4. Concluding remarks and ideas for future work are outlined in section 5.5.

## 5.2 Main Result

Consider $n$ equally spaced time points $t_1, t_2, \ldots, t_n$, and let $\Delta$ be the common length of the time interval between two consecutive points in time. We have:

$$t_k = t_1 + k\Delta, \;\; k = 0, 1, \ldots, n-1.$$

Let $L$ be a positive integer such that $2 \leq L \leq n-1$ and let $W_1, W_2, \ldots, W_{n-L+1}$ be overlapping time windows of length $L\Delta$ defined starting from $t_1$ and advancing by $\Delta$ at a time,

$$W_j = \{t_j, t_{j+1}, \ldots, t_{j+L-1}\}, \;\; j = 1, 2, \ldots, N-L+1.$$

Each time windows $W_j$ contains exactly $L$ of the $n$ time points $t_1, t_2, \ldots, t_n$.

For a generic time series $\{y_t\} = (y_{t_1}, y_{t_2}, \ldots, y_{t_n})$ we define the running trend series associated to $\{y_t\}$ as the series $\{\hat{m}_j\} = (\hat{m}_1, \hat{m}_2, \ldots, \hat{m}_{n-L+1})$ of the the least square estimates of the trend for the time windows $W_j$. That is $\hat{m}_j$ is the least square estimate of the slope $m_j$ in the linear regression

$$y_{t_{j+h-1}} = b_j + m_j \cdot (t_{j+h-1} - \bar{t}_j) + \epsilon_{t_{j+h-1}}, \;\; h = 1, 2, \ldots, L, \tag{5.1}$$

where $\bar{t}_j = \frac{\sum_{i=1}^{L} t_{j+i-1}}{L}$ and $\epsilon_{t_{j+h-1}}$ is an error term.

Let $m_1^\star, m_2^\star, \ldots, m_{n-L+1}^\star$ be $n-L+1$ arbitrary values. We provide a recursive formula to obtain the set of all time series $\{y_t\} = (y_{t_1}, y_{t_2}, \ldots, y_{t_n})$ for which the corresponding trend series $\{\hat{m}_j\} = (\hat{m}_1, \hat{m}_2, \ldots, \hat{m}_{n-L+1})$ is exactly $m_1^\star, m_2^\star, \ldots, m_{n-L+1}^\star$ and we prove that such a set is a vector space of dimension $L-1$. The details are provided in the following theorem (for a proof see the appendix A.1).

**Main result** . *Let $m_1^\star, m_2^\star, \ldots, m_{n-L+1}^\star$ be an arbitrary vector in $\mathbb{R}^{n-L+1}$.*

- **(i)** *The set $S^\star$ of all time series $\{y_t\} = (y_{t_1}, y_{t_2}, \ldots, y_{t_n})$ for which the corresponding trend series $\{\hat{m}_j\} = (\hat{m}_1, \hat{m}_2, \ldots, \hat{m}_{n-L+1})$ is exactly $m_1^\star, m_2^\star, \ldots, m_{n-L+1}^\star$ is a vector space of dimension $L-1$;*
- **(ii)** *The generic element in $S^\star$ is a time series $(y_{t_1}, y_{t_2}, \ldots, y_{t_n})$, where*

- $(y_{t_{n-L+2}}, y_{t_{n-L+3}}, \ldots, y_{t_n})$ *can be arbitrarily chosen in* $\mathbb{R}^{L-1}$,
- $(y_{t_1}, y_{t_2}, \ldots, y_{t_{n-L+1}})$ *can be found using the recursive relation*

$$y_{t_{n-L+1-j}} = \frac{1}{\tilde{t}_1}[c \cdot m^{\star}_{n-L+1-j} - \sum_{h=1}^{L-1} y_{t_{n-L+1-j+h}} \cdot \tilde{t}_h], \quad j = 0, 1, \ldots, n-L \quad (5.2)$$

*where* $\tilde{t}_h = \Delta \cdot (\frac{2h-1-L}{2})$*; and* $c = \sum_{h=1}^{L} (\tilde{t}_h)^2$.

Once we have arbitrarily fixed the values of $(y_{t_{n-L+2}}, y_{t_{n-L+3}}, \ldots, y_{t_n})$, then:

- for $j = 0$ equation 5.2 provides the value of $y_{t_{n-L+1}}$ as a function of $(y_{t_{n-L+2}}, y_{t_{n-L+3}}, \ldots, y_{t_n})$;
- for $j = 1$ equation 5.2 provides the value of $y_{t_{n-L}}$ as a function of $(y_{t_{n-L+1}}, y_{t_{n-L+2}}, \ldots, y_{t_{n-1}})$. And so on.

Implicit in any summary statistics is the trade-off between the ability of the statistic to reduce the dimension of the original data (and thus ease its interpretation) and to preserve as much as possible of the original information. Additional data reduction usually implies higher information loss. According to the above result, and to the intuition, the parameter that controls this trade-off in RTA analysis is $L$, the length of the overlapping time windows $W_j$. The larger is $L$ the larger is the data reduction (since we replace the original series of length $n$ with the new series of running trends of length $n-L+1$), but the smaller is also the amount of information that the series of running trends provides about the underlying time series $\{y_t\}$. As shown in the main result, in fact, the dimension of $S^{\star}$, the space of time series with a given series of running trends, is $L-1$. Thus as $L$ increases the dimension of $S^{\star}$ (and thus the uncertainty on the actual values of the original series $\{y_t\}$) increases as well.

An illustration of the above result and a discussion of its relevance for the interpretation of running trends series as summary statistics for univariate time series and time series association is presented in next sections.

## 5.3 An Illustration

As an illustration of the main result in the previous section, we consider $n = 15$ equally spaced time points $t_1 = 2000$, $t_2 = 2001, \ldots t_{15} = 2014$ (i.e. $\Delta = 1$) and 11 overlapping time windows $W_j$ of length $L = 5$ ($n - L + 1 = 11$). In order to show the general

applicability of the main result we consider three scenarios. Each scenario corresponds to a choice of the series of running trends, and for each scenario we use the main result in section 5.2 to generate five time series of length $n = 15$ that share the same series of running trends. The three scenarios considered are:

**Scenario 1** The series of running trends is approximately linearly increasing (it follows a linear function plus noise);

**Scenario 2** The series of running trends is approximately periodic (follows a sine function plus noise);

**Scenario 3** The series of running trends is a realization of a random noise process. In particular the running trends are generated independently from a normal distribution with mean 300 and standard deviation 50.

The series of running trends for the three scenarios above are shown in table 5.1 and plotted in the top left corner of figures 5.1, 5.2 and 5.3. For each series of running trends the average of the absolute value of the series, $\bar{m}$, is also shown in table 5.1 as an indicator of the magnitude of the running trends in each of the three scenarios considered in the study. Notice that the series of running trends for Scenario 3 is generated independently of the two running trends series for Scenarios 1 and 2. This will be used later in the example.

| | $m_1^\star$ | $m_2^\star$ | $m_3^\star$ | $m_4^\star$ | $m_5^\star$ | $m_6^\star$ | $m_7^\star$ | $m_8^\star$ | $m_9^\star$ | $m_{10}^\star$ | $m_{11}^\star$ | $\bar{m}$ |
|---|---|---|---|---|---|---|---|---|---|---|---|---|
| Scenario 1 | 6.0 | 8.0 | 10.0 | 11.8 | 14.1 | 16.1 | 17.9 | 19.8 | 21.7 | 24.1 | 26.5 | $\hat{m}_1 = 16$ |
| Scenario 2 | -2.5 | -1.6 | 0.9 | 2.4 | 2.1 | 0.2 | -2.4 | -2.4 | -0.4 | 1.7 | 2.3 | $\hat{m}_2 = 1.72$ |
| Scenario 3 | -22.8 | 6.7 | 1.1 | 4.7 | -7.5 | -6.1 | 25.7 | 17.2 | 8.6 | -1.1 | -26.6 | $\hat{m}_3 = 11.65$ |

**Table 5.1:** Series of running trends for the three scenarios considered in the study ($\bar{m}$ denote the average of the absolute value of the runnning trends series).

Let $S_h^\star$ be the space of time series of length $n = 15$ whose running trends series is the one corresponding to Scenario $h$ in table 5.1, $h = 1, 2, 3$. According to the main result in section 5.2, each space $S_h^\star$ has dimension $L - 1 = 4$ and in order to specify a series in $S_h^\star$, we have to arbitrarily fix the values of $(y_{t_{12}}, y_{t_{13}}, y_{t_{14}}, y_{t_{15}})$ which correspond to the *free variables* $(y_{t_{n-L+2}}, y_{t_{n-L+3}}, \ldots, y_{t_n})$ in the main result. The rest of the series is then determined using the recursive formula (5.2). For each scenario we consider five choices of $(y_{t_{12}}, y_{t_{13}}, y_{t_{14}}, y_{t_{15}})$ and thus five time series of length $n = 15$ with the same running trends as those in table 5.1. Four of the five choices are common across scenarios,

in particular we choose $(y_{t_{12}}, y_{t_{13}}, y_{t_{14}}, y_{t_{15}})$ to be: a) constant; b) cubically increasing; c) cubically decreasing; d) alternate. To add a fifth choice, e), different in the different scenarios, we consider $(y_{t_{12}}, y_{t_{13}}, y_{t_{14}}, y_{t_{15}})$ to be: quadratically increasing for Scenario 1; realization of a sine function for Scenario 2; and realizations of a random noise process for Scenario 3. Table 5.2 provides the details.

| SCENARIO | Choice | $(y_{t_{12}}, y_{t_{13}}, y_{t_{14}}, y_{t_{15}})$ | $\bar{y}_{free}$ | $\bar{y}_{free}/\bar{m}_1$ | $\bar{y}_{free}/\bar{m}_2$ | $\bar{y}_{free}/\bar{m}_3$ |
|---|---|---|---|---|---|---|
| | a) | (100 ,100, 100, 100) (constant) | 100 | 6.2 | 58 | 8.6 |
| | b) | (1000, 12704, 49296, 125000) (cubically increasing) | 47000 | 2937.5 | 27265.1 | 4035.9 |
| Scenario 1 | c) | (1500, -10204, -46796, -122500) (cubically decreasing) | 45250 | 2828.1 | 26249.9 | 3885.6 |
| | d) | (100,1100, 100,1100) (alternate) | 600 | 37.5 | 348.1 | 51.5 |
| | e) | (146,171, 199, 228) (quadratically increasing) | 186 | 11.6 | 107.9 | 16 |
| | a)-d) | same as in Scenario 1 | | | | |
| Scenario 2 | e) | (-2.86, 2.84, 4.35, 3.16) (sine) | 3.30 | 0.2 | 1.9 | 0.3 |
| | a)-d) | same as in Scenario 1 | | | | |
| Scenario 3 | e) | (357, 298, 309, 264) (random noise) | 307 | 19.2 | 178.1 | 26.4 |

**Table 5.2:** Choices of the free variables $(y_{t_{12}}, y_{t_{13}}, y_{t_{14}}, y_{t_{15}})$ for the three scenarios considered in the study.

For each choice of the free variables $(y_{t_{12}}, y_{t_{13}}, y_{t_{14}}, y_{t_{15}})$ the average of the absolute value of the $L-1=4$ free variables, $\bar{y}_{free}$, is also shown in table 5.2 as an indicator of the magnitude of the free variables $(y_{t_{12}}, y_{t_{13}}, y_{t_{14}}, y_{t_{15}})$. To compare the magnitude of the free variable with the magnitude of the running trends considered in the three Scenarios 1-3 we also show in table 5.2 the ratio between $\bar{y}_{free}$ and the values of $\bar{m}$ in table 5.1. We see that choices b) and c) in table 5.2 correspond to free variables that in magnitude

are much larger than the series of running trends for the three Scenarios considered in the study; while choices a) and d) correspond to choices of the free variables that in magnitude are moderately larger than the series of running trends for the three Scenarios 1-3. Again, this will be used later in the discussion of the example.

For each scenario, using the five choice of $(y_{t_{12}}, y_{t_{13}}, y_{t_{14}}, y_{t_{15}})$ in table 5.2, we generate five time series in $S_h^\star$ (i.e. five time series with the exactly the same trends series as in table 5.1). The five time series of length $n = 15$ for Scenarios 1, 2 and 3 are plotted in figures 5.1, 5.2 and 5.3 respectively. Since each series correspond to a choice of $(y_{t_{12}}, y_{t_{13}}, y_{t_{14}}, y_{t_{15}})$, we label the series with the same label as the choice of $(y_{t_{12}}, y_{t_{13}}, y_{t_{14}}, y_{t_{15}})$ in table 5.2. To distinguish the values of the free variables $(y_{t_{12}}, y_{t_{13}}, y_{t_{14}}, y_{t_{15}})$, from the rest of the series, in each time series plot $(y_{t_{12}}, y_{t_{13}}, y_{t_{14}}, y_{t_{15}})$ are represented in red. Complete details of each series is provided in table 5.3. In each figure we also plot the series of running trends that they share.

Universitat d'Alacant
Universidad de Alicante

| | Series (a) | Series (b) | Series (c) | Series (d) | Series (e) |
|---|---|---|---|---|---|
| | -139.72 | 142005.14 | -139984.58 | 860.28 | 3.00 |
| | -17.27 | -38372.07 | 40637.54 | -17.27 | 7.00 |
| | -82.65 | 39051.90 | -36917.19 | 917.35 | 11.00 |
| | -90.41 | 75095.12 | -72975.94 | -90.41 | 19.00 |
| | -73.15 | 85301.54 | -83147.84 | 926.85 | 27.00 |
| | 17.98 | -61456.89 | 63792.86 | 17.98 | 39.00 |
| Scenario 1 | -86.84 | 107377.91 | -105251.59 | 913.16 | 51.00 |
| | -24.56 | 64115.94 | -61865.06 | -24.56 | 66.00 |
| | 18.62 | 22585.62 | -20248.38 | 1018.62 | 84.00 |
| | 45.75 | -18980.25 | 21371.75 | 45.75 | 103.00 |
| | -32.50 | 149015.50 | -146780.50 | 967.50 | 122.00 |
| | 100.00 | 1000.00 | 1500.00 | 100.00 | 146.00 |
| | 100.00 | 12704.00 | -10204.00 | 1100.00 | 171.00 |
| | 100.00 | 49296.00 | -46796.00 | 100.00 | 199.00 |
| | 100.00 | 125000.00 | -122500.00 | 1100.00 | 228.00 |
| | 100.97 | 142245.82 | -139743.89 | 1100.97 | 5.66 |
| | 107.37 | -38247.43 | 40762.18 | 107.37 | 3.95 |
| | 95.61 | 39230.15 | -36738.94 | 1095.61 | 0.80 |
| | 92.82 | 75278.35 | -72792.71 | 92.82 | -3.45 |
| | 95.57 | 85470.25 | -82979.12 | 1095.57 | -3.32 |
| | 99.47 | -61375.40 | 63874.35 | 99.47 | -1.91 |
| | 96.72 | 107561.47 | -105068.03 | 1096.72 | 4.47 |
| Scenario 2 | 104.44 | 64244.94 | -61736.06 | 104.44 | 4.85 |
| | 103.52 | 22670.52 | -20163.48 | 1103.52 | 3.74 |
| | 97.16 | -18928.84 | 21423.16 | 97.16 | -0.45 |
| | 88.48 | 149136.48 | -146659.52 | 1088.48 | -4.75 |
| | 100.00 | 1000.00 | 1500.00 | 100.00 | -2.86 |
| | 100.00 | 12704.00 | -10204.00 | 1100.00 | 2.84 |
| | 100.00 | 49296.00 | -46796.00 | 100.00 | 4.35 |
| | 100.00 | 125000.00 | -122500.00 | 1100.00 | 3.16 |
| | 235.21 | 142380.07 | -139609.64 | 1235.21 | 387.00 |
| | 59.00 | -38295.81 | 40713.80 | 59.00 | 330.00 |
| | 92.79 | 39227.34 | -36741.76 | 1092.79 | 272.00 |
| | 37.61 | 75223.14 | -72847.92 | 37.61 | 242.00 |
| | 131.91 | 85506.59 | -82942.78 | 1131.91 | 317.00 |
| | 72.94 | -61401.94 | 63847.81 | 72.94 | 341.00 |
| | 80.62 | 107545.37 | -105084.13 | 1080.62 | 228.00 |
| Scenario 3 | 86.75 | 64227.25 | -61753.75 | 86.75 | 310.00 |
| | 87.50 | 22654.50 | -20179.50 | 1087.50 | 295.00 |
| | 39.00 | -18987.00 | 21365.00 | 39.00 | 277.00 |
| | 233.00 | 149281.00 | -146515.00 | 1233.00 | 373.00 |
| | 100.00 | 1000.00 | 1500.00 | 100.00 | 357.00 |
| | 100.00 | 12704.00 | -10204.00 | 1100.00 | 298.00 |
| | 100.00 | 49296.00 | -46796.00 | 100.00 | 309.00 |
| | 100.00 | 125000.00 | -122500.00 | 1100.00 | 264.00 |

**Table 5.3:** Time series for each of the three scenarios considered.

Universitat d'Alacant
Universidad de Alicante

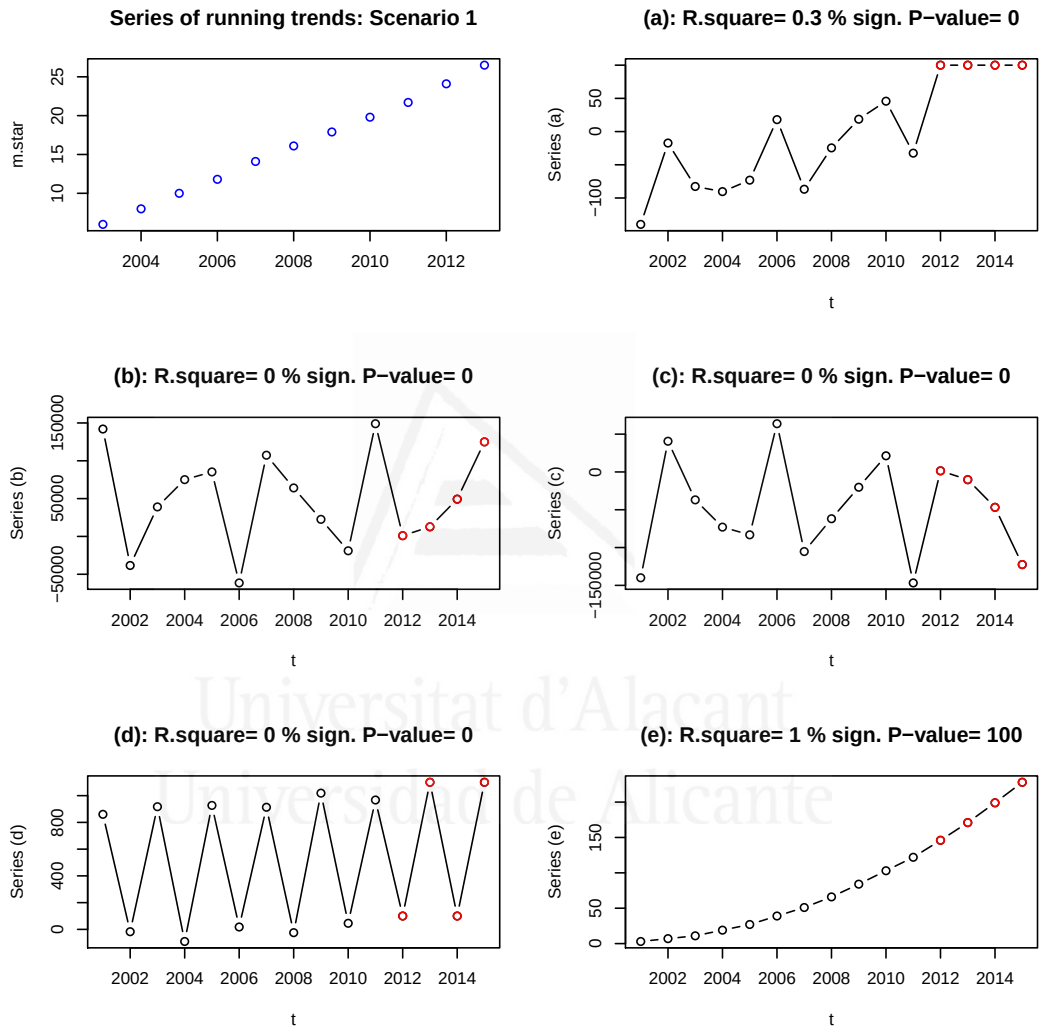


**Figure 5.1:** Five series with the same runnig trend series as in Scenario 1. Since each series correspond to a choice $(y_{t_{12}}, y_{t_{13}}, y_{t_{14}}, y_{t_{15}})$ in table 5.2 we label the series with the same label as the choice of $(y_{t_{12}}, y_{t_{13}}, y_{t_{14}}, y_{t_{15}})$ in table 5.2. For each series, the average R-square across different windows and the percentage of running trends that are statistically significant at the significant level $\alpha = 0.05$ are denoted by *Avg. R-square* and *% sig. trends* respectively.

Universitat d'Alacant
Universidad de Alicante

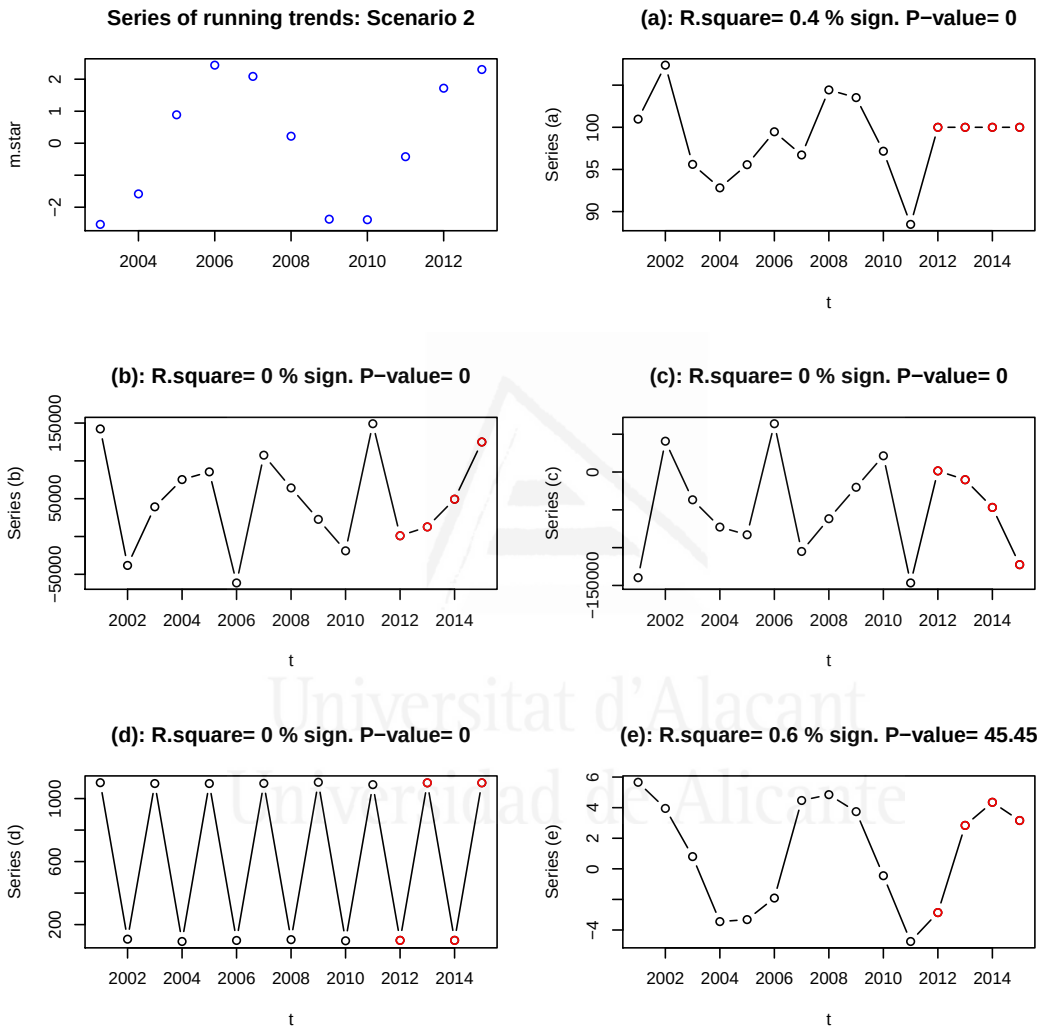


**Figure 5.2:** Five series with the same runnig trend series as in Scenario 2. Since each series correspond to a choice $(y_{t_{12}}, y_{t_{13}}, y_{t_{14}}, y_{t_{15}})$ in table 5.2 we label the series with the same label as the choice of $(y_{t_{12}}, y_{t_{13}}, y_{t_{14}}, y_{t_{15}})$ in table 5.2. For each series, the average R-square across different windows and the percentage of running trends that are statistically significant at the significant level $\alpha = 0.05$ are denoted by *Avg. R-square* and *% sig. trends* respectively.

Universitat d'Alacant
Universidad de Alicante

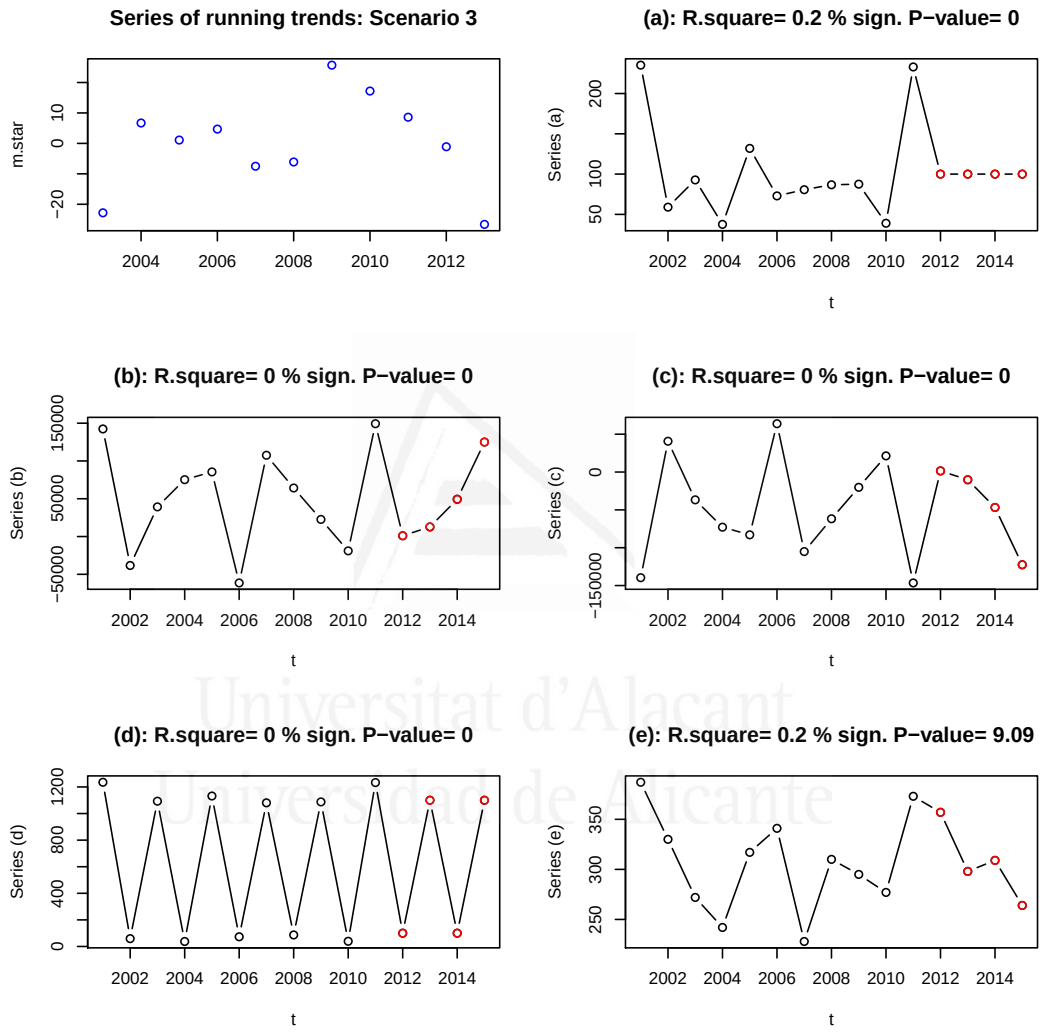


**Figure 5.3:** Five series with the same runnig trend series as in Scenario 3. Since each series correspond to a choice $(y_{t_{12}}, y_{t_{13}}, y_{t_{14}}, y_{t_{15}})$ in table 5.2 we label the series with the same label as the choice of $(y_{t_{12}}, y_{t_{13}}, y_{t_{14}}, y_{t_{15}})$ in table 5.2. For each series, the average R-square across different windows and the percentage of running trends that are statistically significant at the significant level $\alpha = 0.05$ are denoted by *Avg. R-square* and *% sig. trends* respectively.

Universitat d'Alacant
Universidad de Alicante

## 5.4 Discussion

Despite its simplicity, the worked example in section 5.3 highlights some importante consequences of the main result in section 5.2. In particular:

1. Time series with a very different behaviour might share exactly the same running trends series (compare the series (a)-(e) in each of the figures 5.1-5.3). This is true in general. Different choices of the free variables $(y_{t_{n-L+2}}, y_{t_{n-L+3}}, \ldots, y_{t_n})$ in the main result (increasing, decreasing, constant, periodic, etc.), will lead to time series with the same running trends but whose behaviours are very different. This remark has two important implications.

   First of all, a series of running trends, alone, provides a poor description of the underlying time series. That is, **a running trends series alone, has a poor performance, as summary statistics of univariate time series**.

   Secondly, **strong association between running trends series, alone, does not imply any association between the underlying time series**. Consider, for example, the time series (c) and (e) in figure 5.1. Suppose that series (c) represents simulations of a certain variable $X$ (for the period 2000-2014) from a given model and that series (e) represents the observed values of $X$ for the same period. If we use the correlation between 5-year running trends of series (c) and (e) to assess the model's performance, we would conclude that the model performance is very good (the correlation between the two running trends series is 1 since (c) and (e) share exactly the same series of running trends). However this result would be misleading. If we compare the series (c) and (e) we would say that the model's performance is extremely poor.

   The fact that strong association between running trends series, alone, does not imply any association between the underlying time series is particularly evident if we focus on the last time window $W_{n-L+1}$. According to the main result in section 5.2, in fact, we can arbitrary fix the value of $L-1$ out of the $L$ points in $W_{n-L+1}$ and then use the recursive equation 5.2 to obtain a series with the desired running trends. In the example above this was exemplified by our arbitrary choice of the free variables $(y_{t_{12}}, y_{t_{13}}, y_{t_{14}}, y_{t_{15}})$ in table 5.2.

   As an illustration, consider again the time series (c) and (e) in figure 5.1. Suppose that series (c) represents the time series of a certain variable $X$ (for the period 2000-

2014) and that series (e) represents the time series of a certain variable $Y$ for the same period. The association between the running trends series corresponding to series (c) and (e) is perfect (since the two time series share the same series of running trends). However this information, alone, does not tell us anything about the contribution of $X$ to $Y$ (or the relationship between $X$ and $Y$ ) for the period 2009-2014 (i.e. in the time $W_{11}$) since 4 out of 5 values of each series in $W_{11}$ are completely unconstrained.

2. Time series with very different running trends series might be almost identical. For example, compare the series (b) in figures 5.1, 5.2 and 5.3 (or equivalently consider the time series (b) in table 5.3 corresponding to the the three scenarios). We observe that the three series are almost identical (the minimum correlation between pair of (b) series corresponding to two of the three scenarios considered in the study is greater than 0.999999 !) despite the fact the the corresponding series of running trends are at best only weakly associated. The implication of this remark is that **absence of association between running trends series does not imply absence of association between the original series**. Once again, consider the series (b) in figure 5.1 and in figure 5.3. Suppose that series (b) in figure 5.1 represents simulations of a certain variable $X$ (for the period 2000-2014) from a given model and that series (b) in figure 5.3 represents the observed values of $X$ for the same period. If we use the association between 5-year running trends of series (b) in figure 5.1 and series (b) in figure 5.3 to assess the model's performance, we would conclude that the model performance is very poor (the correlation between the two running trends series is 0.035). However this result would be misleading. If we compare the series (c) and (e) we would say that the model's performance is excellent.

   Again this is true in general and can be explained by the difference in magnitude between the running trends series and the free variables $(y_{t_{n-L+2}}, y_{t_{n-L+3}}, \ldots, y_{t_n})$. Given a series of running trends $m_1^\star, m_2^\star, \ldots, m_{n-L+1}^\star$, we can always choose the magnitude of the free variables $(y_{t_{n-L+2}}, y_{t_{n-L+3}}, \ldots, y_{t_n})$ sufficiently large to make negligible the contribution of the running trends in the recursive equation in 5.2. Thus it is possible to have two time series $\{x_t\}$ and $\{y_t\}$ that are almost identical (and thus that show very high association) but whose running trends series are practically independent. To build two such time series $\{x_t\}$ and $\{y_t\}$ it would be sufficient to: (i) generate independently two series of running trends; (ii) then arbitrarily fix the value

of $(x_{t_{n-L+2}}, x_{t_{n-L+3}}, \ldots, x_{t_n})$ for the first series in such a way that the magnitude of $(x_{t_{n-L+2}}, x_{t_{n-L+3}}, \ldots, x_{t_n})$ is much larger than the magnitude of the two series of running trends and set $(y_{t_{n-L+2}}, y_{t_{n-L+3}}, \ldots, y_{t_n}) = (x_{t_{n-L+2}}, x_{t_{n-L+3}}, \ldots, x_{t_n})$; finally (iii) use the vectors of free variables in (ii), the two series of running trends in (i) and the recursive equation in 5.2 to obtain the desired series $\{x_t\}$ and $\{y_t\}$. This is exactly what we did for the (b)-series in our example. The running trend series for Scenario 1 and 3 were generated independently, and the series (b) where generated for each Scenario by choosing the magnitude of the free variables much larger than the magnitude of the corresponding running trends series (compare the value of $\bar{y}_{free}$ and the values of $\bar{m}_i$ for $i \in \{1, 2\}$ in table 5.2). The corresponding (b)-series were then completed using the recursive formula 5.2.

## 5.5 Conclusions

Running trends series are widely used as summary statistics for univariate time series and time series association. In this chapter we obtained an explicit formula for the set of time series with a given series of running trends and we used this formula to better understand the limitations of running trend series as descriptive statistics for univariate time series and time series association. The most important implications of the main result in section 5.2, as we discussed in the previous section, are that: (i) running trends, *alone*, provides very limited information about the underlying time series; and (ii) lack or presence of association between the running trends of two time series, *alone*, tell us almost nothing about the association of the underlying time series. This should not be interpreted as an argument against the use of running trends as descriptive statistics for univariate time series and time series association but rather as a cautionary note on the use of running trends in applications. It is quite common in descriptive statistics that a descriptive measure, *alone*, is of very limited use. For example, a measure of location, like the mean, provides very limited information about the underlying data set if it is not accompanied by a measure of dispersion, like the variance, and information about presence of outliers. A small variance, and absence of outliers, imply that the mean is a representative value of the underlying data set. While a high variance or the presence of outliers would suggest that the mean is a poor descriptive statistics for the underlying data set. Thus the question is what are the descriptive measures that should accompany the running trends series and that can be used as an

indicator of the performance of running trend series as descriptive statistics for univariate time series and time series association?. In our understanding such descriptive measures should be numerical indices that summarize the extent to which the linear models in 5.1 provide a suitable description of the behaviour of the series in each of the overlapping time windows $W_j$. One of such measure could be, for example, the average of the $n - L + 1$ $R$-squares corresponding to fitting the linear models in 5.1 for each time windows $W_j$. For a given time series, the $R$-square for the time window $W_j$ measures the proportion of the total variability of the series explained by (the least square estimate of) the linear model in 5.1, thus $R$-square takes value in $[0, 1]$. An $R$-square close (equal) to 1 for a certain time window $W_j$ would indicate that the time series is approximately (exactly) linear in $W_j$ and thus the estimated linear trend $m_j^\star$ provides a a very good (perfect) description of the behaviour of the time series in $W_j$. The average $R$-square across different windows (Avg. R-square) would thus be a natural summary of the overall performance of running trends as summary statistics. An alternative measure could be the percentage of the $n-L+1$ running trends that are statistically significant at the significant level $\alpha = 0.05$ (% sig. trends). The value of these two summary statistics has been reported for each series in figures 5.1-5.3. If we consider figure 5.1 (Scenario 1), for example, we see that according to the average R-square, and the percentage of running trends that are statistically significant at the significant level $\alpha = 0.05$, running trends as summary statistics, performs very well for the series (e), and very poorly for all the other series. For series (e) which is quadratically increasing, the average R-square is approximately 1, that means that running trends describe almost perfectly the behaviour of the series in each time window $W_j$, and can in fact be interpreted as acceleration of the underlying series (e). A reconstruction (by integration) of the original series (e) based on the running trend, in this case, would reproduce almost perfectly the original series in (e). In terms of time series association, the small (approximately 0) value of the average $R$-square and of the percentage of running trends that are statistically significant at the significant level $\alpha = 0.05$ for series (a)-(d) would imply that running trend series would provide a very poor measure of association between any pair of the series in figure 5.1. The definition of suitable measures of the performance of running trends as summary statistics for univariate time series and time series association can be an interesting topic for future work. The two examples that I discussed (average $R$-square and percentage of statistically significant p-values ) were just used for illustrative purposes, and

further research we think should be done in this direction. Such a research would be relevant not only for the assessment of the performance of running trends as summary statistics but also for the definition of criteria for the choice of the optimal time window length, $L$, to be used in running trend analysis.

Universitat d'Alacant
Universidad de Alicante

CHAPTER

# A

# Appendix

## A.1 Running Trends Analysis: Proof of the Main results

Consider a time series $y_{t_1}, y_{t_2}, \ldots, y_{t_n}$, and the linear model in (5.1) for a given $j \in \{0, 1, \ldots, n-L\}$ and let $\tilde{t}_h = \Delta(\frac{2h-1-L}{2})$. The least square estimate of the regression coefficients $b_j$ and $m_j$ are given by:

$$\begin{pmatrix} \hat{b}_j \\ \hat{m}_j \end{pmatrix} = \left[ \begin{pmatrix} 1 & 1 & \ldots & 1 \\ \tilde{t}_1 & \tilde{t}_2 & \ldots & \tilde{t}_L \end{pmatrix} \begin{pmatrix} 1 & \tilde{t}_1 \\ 1 & \tilde{t}_2 \\ \ldots & \ldots \\ 1 & \tilde{t}_L \end{pmatrix} \right]^{-1} \begin{pmatrix} 1 & 1 & \ldots & 1 \\ \tilde{t}_1 & \tilde{t}_2 & \ldots & \tilde{t}_L \end{pmatrix} \begin{pmatrix} y_{t_j} \\ y_{t_j+1} \\ \ldots \\ y_{t_j+L-1} \end{pmatrix}$$

$$= \frac{1}{L \cdot \sum_{h=1}^{L} (\tilde{t}_h)^2} \cdot \begin{pmatrix} \sum_{h=1}^{L} (\tilde{t}_h)^2 & 0 \\ 0 & L \end{pmatrix} \begin{pmatrix} \sum_{h=1}^{L} y_{t_j+h-1} \\ \sum_{h=1}^{L} \tilde{t}_h \cdot y_{t_j+h-1} \end{pmatrix} = \begin{pmatrix} \frac{\sum_{h=1}^{L} y_{t_j+h-1}}{L} \\ \frac{\sum_{h=1}^{L} \tilde{t}_h \cdot y_{t_j+h-1}}{\sum_{h=1}^{L} (\tilde{t}_h)^2} \end{pmatrix}$$

Let $c = \sum_{h=1}^{L} (\tilde{t}_h)^2$, according to the above formula the running trend for time windows $W_j$ can be written as

$$\hat{m}_j = \frac{1}{c} \times \sum_{h=1}^{L} \tilde{t}_h \cdot y_{t_j+h-1} = \begin{cases} (\tilde{t}_1, \tilde{t}_2, \ldots, \tilde{t}_L, 0, 0, 0, \ldots, 0)(y_{t1}, y_{t2}, \ldots, y_{t_n})^T & if\ j = 1 \\ (0, \tilde{t}_1, \tilde{t}_2, \ldots, \tilde{t}_L, 0, 0, \ldots, 0)(y_{t1}, y_{t2}, \ldots, y_{t_n})^T & if\ j = 2 \\ (0, 0, \tilde{t}_1, \tilde{t}_2, \ldots, \tilde{t}_L, 0, \ldots, 0)(y_{t1}, y_{t2}, \ldots, y_{t_n})^T & if\ j = 3 \\ \ldots\ldots\ldots\ldots\ldots\ldots\ldots\ldots\ldots\ldots\ldots\ldots & \ldots \\ (0, 0, \ldots, 0, 0, \tilde{t}_1, \tilde{t}_2, \ldots, \tilde{t}_L)(y_{t1}, y_{t2}, \ldots, y_{t_n})^T & if\ j = n-L+1 \end{cases} \tag{A.1}$$

where "T" denotes transposition.

According to formula A.1, the set $S^\star$ of all time series $\{y_t\} = (y_{t_1}, y_{t_2}, \ldots, y_{t_n})$ for which the corresponding trend series $\{\hat{m}_j\} = (\hat{m}_1, \hat{m}_2, \ldots, \hat{m}_{n-L+1})$ is exactly $m_1^\star, m_2^\star, \ldots, m_{n-L+1}^\star$ is the solution set of the following linear system with $n - L + 1$ equations (the number of time windows $W_j$) and $n$ unknowns $(y_{t_1}, y_{t_2}, \ldots, y_{t_n})$.

$$\left\{ \begin{array}{ccccccccccc} \tilde{t}_1 \cdot y_{t_1} & \tilde{t}_2 \cdot y_{t_2} & \ldots & \tilde{t}_L \cdot y_{t_L} & & & & & & & = c \cdot m_1^\star \\ & \tilde{t}_1 \cdot y_{t_2} & \tilde{t}_2 \cdot y_{t_3} & \ldots & \tilde{t}_L \cdot y_{t_{L+1}} & & & & & & = c \cdot m_2^\star \\ & & \tilde{t}_1 \cdot y_{t_3} & \tilde{t}_2 \cdot y_{t_4} & \ldots & \tilde{t}_L \cdot y_{t_{L+2}} & & & & & = c \cdot m_3^\star \\ \ldots & \ldots & \ldots & \ldots & \ldots & \ldots & \ldots & \ldots & \ldots & & \ldots \\ & & & & & \tilde{t}_1 \cdot y_{t_{n-L+1}} & \tilde{t}_2 \cdot y_{t_{n-L+2}} & \ldots & \tilde{t}_L \cdot y_{t_n} & & = c \cdot m_{n-L+1}^\star \end{array} \right. \tag{A.2}$$

From standard algebra we obtain that solution set of the above system has dimension $L-1$ and the generic solution of the system is obtained by assigning an arbitrary value to the *free variables* $(y_{t_{n-L+2}}, y_{t_{n-L+3}}, \ldots, y_{t_n})$ and evaluating the rest of the variable using back-substitution in formula A.2. This leads to the recursive formula:

$$y_{n-L+1-j} = \frac{c}{\tilde{t}_1} \cdot m_{n-L+1-j}^\star - \sum_{h=1}^{L-1} y_{t_{n-L+1-j+h}} \cdot \tilde{t}_h, \quad j = 0, 1, \ldots, n-L$$

Once we have arbitrarly fixed the values of $(y_{t_{n-L+2}}, y_{t_{n-L+3}}, \ldots, y_{t_n})$, then:

- for $j = 0$ the recursive formula above provides the value of $y_{t_{n-L+1}}$ as a function of $(y_{t_{n-L+2}}, y_{t_{n-L+3}}, \ldots, y_{t_n})$.
- for $j = 1$ the recursive formula above provides the value of $y_{t_{n-L}}$ as a function of $(y_{t_{n-L+1}}, y_{t_{n-L+2}}, \ldots, y_{t_{n-1}})$. And so on.

Universitat d'Alacant
Universidad de Alicante

# References


Altamimi, Z., X. Collilieux, J. Legrand, B. Garayt, and C. Boucher, 2007: ITRF2005: A new release of the International Terrestrial Reference Frame based on time series of station positions and Earth Orientation Parameters. *J. Geophys. Res.*, **112**, B09 401, doi: 10.1029/2007JB004949. 19

Altamimi, Z., X. Collilieux, and L. Metivier, 2011: ITRF2008: an improved solution of the International Terrestrial Reference Frame. *J. Geod.*, **85**, 457–473, doi: 10.1007/s00190-011-0444-4. xii, 15, 19

Altamimi, Z., P. Sillard, and C. Boucher, 2002: ITRF2000: A new release of the International Terrestrial Reference Frame for Earth science applications. *J. Geophys. Res.*, **107**, ETG 2–1 ETG 2–19, doi:10.1029/2001JB000561. 19

Belda, S., J. Böhm, and J.-M. Ferrándiz, 2014a: Improvements in EOPs and baseline estimation using the future RAEGE network. *Geophys. Res. Abstr. EGU2014-9997*, **35**. ix, 6

Belda, S., D. García-García, and J.-M. Ferrándiz, 2014b: On the decorrelation filtering of RL05 GRACE data for global applications. *Geophys. J. Int.*, **200**, 173–184, doi:10.1093/gji/ggu386.

Belda, S., R. Heinkelmann, J.-M. Ferrándiz, T. Nilsson, and H. Schuh, 2015a: A new empirical model for Free Core Nutation. *Geophys. Res. Abstr. EGU2015-11088*, **17**.

Belda, S., R. Heinkelmann, J.-M. Ferrándiz, T. Nilsson, and H. Schuh, 2015b: On the consistency of the current conventional EOP series and the Celestial and Terrestrial reference frames. *J. Geod.*, **In review**.


Universitat d'Alacant
Universidad de Alicante

Belda, S., and Coauthors, 2014c: Reference frame induced long-term effects on EOP. *Geodaetische Woche*.

Bettadpur, B., 2012: CSR Level-2 processing standards document for product release 05. *GRACE 327-742*, **Revison 4.0**. 47

Blewitt, G., and Coauthors, 2010: Geodetic Observations and Global Reference Frame Contributions to Understanding Sea-Level Rise and Variability. *Understanding Sea-Level Rise and Variability*, **Chapter**, 9, doi:10.1002/9781444323276.ch9. x, 9

Bloßfeld, M., M. Seitz, and D. Angermann, 2014: Non-linear station motions in epoch and multi-year reference frames. *J. Geod.*, **88**, 46–63, doi:10.1007/s00190-013-0668-6. 32

Böckmann, S., T. Artz, and A. Nothnagel, 2010: VLBI Terrestrial Reference Frame contributions to ITRF2008. *J. Geod.*, **84**, 201–219, doi:10.1007/s00190-009-0357-7. 19

Böhm, J., S. Böhm, A. Pany, L. Plank, H. Spicakova, T. Teke, and H. Schuh, 2012: The new Vienna VLBI Software VieVS. *Geodesy for Planet Earth*, **Proc. of the 2009 IAG Symp.**, 1007–1011, doi:10.1007/978-3-642-20338-1_126. xii, 18

Böhm, J., B. Werl, and H. Schuh, 2006: Troposphere mapping functions for GPS and very long baseline interferometry from European Centre for Medium-Range Weather Forecasts operational analysis data. *J. Geophys. Res.*, **1111**, B2, doi:10.1029/2005JB003629. 18

Bradley, B., D. Vallado, A. Sibois, and P. Axelrad, 2012: Earth Orientation Parameter Considerations for Precise Spacecraft operations. *Astronaut. Sci.*, **142**, 13. 1

Campbell, J., 2000: From Quasars to Benchmarks: VLBI Links Heaven and Earth. *IVS 2000 General Meeting Proc.*, **CP-2000-209893**. 3

Cannon, W., 1999: Overview of VLBI. *International VLBI Service for Geodesy and Astronomy 1999 Annual Report*, **TP-1999-209243**. viii, 4

Capitaine, N., P. Mathews, V. Dehant, P. Wallace, and S. Lambert, 2009: On the IAU 2000/2006 precession–nutation and comparison with other models and VLBI observations. *Celest. Mech. Astron.*, **103**, 179–190, doi:10.1007/s10569-008-9179-9. 37

Universitat d'Alacant
Universidad de Alicante

Capitaine, N., P. Wallace, and J. Chapront, 2003: Expressions for IAU 2000 precession quantities. *Astron. Astrophys.*, **412**, 567–586, doi:10.1051/0004-6361:20031539. 36

Cazenave, A., and J. Chen, 2010: Time-variable gravity from space and present-day mass redistribution in the Earth system. *Earth and Planet. Sci. Lett.*, **298**, 263–274, doi:10.1016/j.epsl.2010.07.035. 12

Chambers, D., 2006: Evaluation of new GRACE time-variable gravity data over the ocean. *Geophys. Res. Lett.*, **33**, L17 603, doi:10.1029/2006GL027296. 12, 48, 49, 50

Chambers, D., and J. Bonin, 2012: Evaluation of Release-05 GRACE time-variable gravity coefficients over the Ocean. *Ocean Sci. Discuss.*, **9**, 2187–2214, doi:10.5194/os-8-859-2012. xxiv, 48, 50, 65, 66, 67

Chao, B., 1994: The Geoid and Earth rotation. *Geoid and its geophysical Interpretations*, **ed. P. Vanicek and N. Christou**, 285–298. x, 7, 8

Chao, B., 2005: On inversion for mass distribution from global (time variable) gravity field. *J. Geodyn.*, **39**, 223–230, doi:10.1016/j.jog.2004.11.001. xx, xxi, 47, 49

Chen, J., C. Wilson, and K. Seo, 2006: Optimized smoothing of gravity recovery and climate experiment (GRACE) time-variable gravity observations. *J. Geophys. Res*, **111**, B06 408, doi:10.1029/2005JB004064. 48

Chen, J., C. Wilson, B. Tapley, and S. Grand, 2007: Grace detects coseismic and post-seismic deformation from the Sumatra-Andaman earthquake. *Geophys. Res. Lett.*, **34**, L13 302, doi:10.1029/2007GL030356. xxi, xxii, xxiv, 48, 49, 50, 59, 62, 65, 67

Chen, J., C. Wilson, and Y. Zhou, 2012: Seasonal excitation of polar motion. *J. Geod.*, **62**, 8–15, doi:10.1016/j.jog.2011.12.002. 7

Cheng, M., and J. Ries, 2007: GRACE technical note 05: monthly estimates of C20 from 5 SLR satellites. *Available at: http://podaac.jpl.nasa.gov/grace/documentation*. 49

Cummins, P., and J. Wahr, 1993: A study of the Earth's free core nutation using IDA gravity data. *J. Geophys. Res.*, **98**, 2091–2104, doi:10.1029/92JB01956. 34

Universitat d'Alacant
Universidad de Alicante

Dahle, C., F. Flechtner, C. Gruber, D. König, R. König, G. Michalak, and K.-H. Neumayer, 2013: GFZ GRACE level-2 processing standards document for level-2 product release 0005. *Available at: http://podaac.jpl.nasa.gov/gravity/grace-documentation*. 47

Defraigne, P., V. Dehant, and P. Paquet, 1995: Link between the Retrograde-Prograde Nutations and Nutations in Obliquity and Longitude. *Celest. Mech. Dyn. Astron.*, **62**, 363–376, doi:10.1007/BF00692286. 34

Dehant, V., 2002: Report of the IAU working group on 'Nonrigid-Earth Nutation Theory'. *Highlights of Astron.*, **12**, 117–119. 22

Dehant, V., O. Viron, and J. Barriot, 2005: Geophysical excitation of the Earth orientation parameters EOP and its contribution to GGOS. *J. Geodyn.*, **40**, 394–399, doi:10.1016/j.jog.2005.06.004. ix, 5

Duan, X., J. Guo, C. Shum, and W. Van der Wal, 2009: On the postprocessing removal of correlated errors in GRACE temporal gravity field solutions. *J. Geod.*, **83**, 1095–1106, doi:10.1007/s00190-009-0327-0. xxi, xxiv, 48, 49, 50, 53, 65, 66, 67

Feissel, M., and Coauthors, 2013: Earth Orientation and related Reference Frames. *Contributions of Space Geodesy to Geodynamics: Earth Dynamics*, **24**, 99–111, doi:10.1029/GD024p0099.

Ferrándiz, J.-M., and R. Gross, 2014: The new IAU/IAG Joint Working Group on Theory of Earth Rotation. *Proc. of the IAG Symp. (to appear)*, **143**. 27

Fey, A. L., and Coauthors, 2004: The Second Extension of the International Celestial Reference Frame: ICRF-EXT.1. *Astron. J.*, **127**, 3587, doi:10.1086/420998. xii, 15, 19

Florsch, N., and J. Hinderer, 2000: Bayesian estimation of the free core nutation parameters from the analysis of precise tidal gravity data. *Phys. Earth Planet. Inter.*, **117**, 21–35, doi:10.1016/S0031-9201(99)00084-9. 34

Furuya, M., Y. Hamano, and I. Naito, 1996: Quasi-periodic wind signal as a possible excitation of Chandler wobble. *J. Geophys. Res.*, **101**, 25 537–25 546, doi:10.1029/96JB02650. 45

Universitat d'Alacant
Universidad de Alicante

García-García, D., B. Chao, and J.-P. Boy, 2010: Steric and mass-induced sea level variations in the Mediterranean Sea. *J. Geophys. Res.*, **115**, C12 016, doi:10.1029/2009JC005928. 48

Getino, J., and J.-M. Ferrándiz, 2000: Accurate analytical nutation series. *Mon. Not. R. Astr. Soc.*, **306**, L45–L49, doi:10.1046/j.1365-8711.1999.02741.x. 36

Gross, R., 2000: The excitation of the Chandler wobble. *Geophys. Res. Lett.*, **27**, 2329–2332, doi:10.1029/2000GL011450. 45

Gwinn, C., T. Herring, and I. Shapiro, 1986: Geodesy by radio interferometry: Studies of the forced nutations of the Earth: 2. interpretation. *J. Geophys. Res.*, **91**, 4755–4765, doi:10.1029/JB091iB05p04755. 34

Hamlington, B. D., M. W. Strassburg, R. R. Leben, W. Han, R. S. Nerem, and K.-Y. Kim, 2014: Uncovering an antropogenic sea-level rise signal in the Pacific ocean. *Nat. Clim. Change*, **4**, 782–785, doi:10.1038/nclimate2307. xxiv, 70

Hamlington, B. D., M. W. Strassburg, R. R. Leben, R. S. Nerem, and K.-Y. Kim, 2013: Contribution of the Pacific Decadal Oscillation to global mean sea level trends. *Geophys. Res. Lett.*, **40**, 5171–5175, doi:10.1002/grl.50950. xxiv, 70

Heinkelmann, R., S. Belda, J.-M. Ferrándiz, and H. Schuh, 2014a: The consistency of the current conventional Celestial and Terrestrial Reference Frames and the conventional EOP series. *Journ. 2014 Systémes de reference spatio-temporels*, **In print**.

Heinkelmann, R., S. Belda, J.-M. Ferrándiz, and H. Schuh, 2014b: How consistent are the current conventional Celestial and Terrestrial Reference Frames and the conventional Earth orientation parameters? *IAG Symp. Series REFAG 2014 Proc.*, **In review**.

Heinkelmann, R., T. Nilsson, M. Karbon, V. Raposo-Pulido, B. Soja, and H. Schuh, 2014c: Reference frame-induced error in VLBI Earth orientation determinations. *Geophy. Res. Abst.*, **16**, EGU2014–5107. 18

Heiskanen, W., and H. Moritz, 1967: Physical Geodesy. *Book*. 12

Herring, T., C. Gwinn, and I. Shapiro, 1986: Geodesy by radio interferometry: Studies of the forced nutations of the Earth: 1. Data analysis. *J. Geophys. Res.*, **91**, 4745–4754, doi:10.1029/JB091iB05p04745. 34

Universitat d'Alacant
Universidad de Alicante

Hilton, J., and Coauthors, 2006: Report of the International Astronomical Union Division I Working Group on Precession and the Ecliptic. *Celest. Mech. Dyn. Astron.*, **94**, 351–367, doi:10.1007/s10569-006-0001-2. 22

Holgate, S. J., and P. L. Woodworth, 2004: Evidence for enhanced coastal sea level rise during the 1990s. *Geophys. Res. Lett.*, **31**, L07 305, doi:10.1029/2004GL019626. xxiv, 69

Jekeli, C., 1981: Alternative methods to smooth the Earth's gravity field. Department of Geod. Sci. and Surv., Ohio State Univ. (Columbus). xx, 12, 48

Kierulf, H., and H. Plag, 2006: Precise point positioning requires consistent global products. *EUREF Publication No. 14*, **35**, 111. viii, 3

Krásná, H., J. Böhm, and H. Schuh, 2013: Free Core Nutation observed by VLBI. *Astron. Astrophys.*, **555**, A29, doi:10.1051/0004-6361/201321585. x, xvii, xviii, xix, 9, 12, 23, 34, 36, 43, 44, 45

Lambert, S., 2007: Empirical model of the Free Core Nutation. *Technical note available at http://syrte.obspm.fr/.* x, xvii, xix, 9, 12, 23, 34, 36, 43

Lambert, S., and V. Dehant, 2007: The Earth's core parameters as seen by the VLBI. *Astron. and Astrophys.*, **469**, 777–781, doi:10.1051/0004-6361:20077392. 35

Landerer, F., and S. Swenson, 2012: Accuracy of scaled GRACE terrestrial water storage estimates. *Water Resour. Res.*, **48**, W04 531, doi:10.1029/2011WR011453. 57

Ma, C., E. F. Arias, T. Eubanks, A. Fey, A.-M. Gontier, C. Jacobs, O. S. . B. Archinal, and P. Charlot, 1998: The International Celestial Reference Frame as Realized by Very Long Baseline Interferometry. *Astron. J.*, **116**, 516, doi:10.1086/300408. 19

Ma, C., and Coauthors, 2009: The Second Realization of the International Celestial Reference Frame by Very Long Baseline Interferometry. *IERS Technical Note*, **No. 35**, 1–204. xvii, 12, 19

Malkin, Z., 2004: Comparison of VLBI nutation series with the IAU2000A model. *Proc. of Journ. 2003: Astrom., Geodyn. and Solar System Dyn.: from milliarcseconds to microarcseconds*, **Eds. A. Finkelstein, N. Capitaine**, 24–31.

Universitat d'Alacant
Universidad de Alicante

Malkin, Z., 2007: Empirical Models of the Earth's Free Core Nutation. *Sol. Syst. Res.*, **41 (6)**, 492–497, doi:10.1134/S0038094607060044.

Malkin, Z., 2010: Comparison of CPO and FCN empirical models. *In: Proc. Journ. 2010: New challenges for reference systems and numerical standards in astronomy*, **ed. N. Capitaine**, 172–175. x, 9, 23, 36

Malkin, Z., 2013: Free core nutation and geomagnetic jerks. *J. Geodyn.*, **72**, 53–58, doi: 10.1016/j.jog.2013.06.001. 23

Mathews, P., T. Herring, and B. Buffet, 2002: Modeling of nutation and precession: New nutation series for nonrigid Earth and insights into the earth's interior. *J. Geophys. Res.*, **107**, 3–1–3–26, doi:10.1029/2001JB000390. 36

Moritz, H., and I. Mueller, 1987: Earth Rotation. Theory and observation. *Ung. Publ. New York*. 7

Nilsson, T., R. Heinkelmann, M. Karbon, V. Raposo-Pulido, B. Soja, and H. Schuh, 2014: Earth Orientation Parameters estimated from VLBI during the CONT11 campaign. *J. Geod*, **88**, 491–502, doi:10.1007/s00190-014-0700-5. xiii, 18

Palmer, M. D., and D. J. McNeall, 2014: Internal variability of Earth's energy budget simulated by CMIP5 climate models. *Environ. Res. Lett.*, **9**, 034 016, doi:10.1088/1748-9326/9/3/034016. xxiv, 70

Paulson, A., S. Zhong, and J. Wahr, 2007: Inference of mantle viscosity from GRACE and relative sea level data. *Geophys. J. Int.* 53

Peters, T., J. Muller, and N. Sneeuw, 2002: Temporal variations in the Earth's gravity field with emphasis on atmospheric effects. *Schuh, H.; Soffel, M.; Hornik, H. (eds.) Vortrage beim 4. DFG-Rundgespräch im Rahmen des Forschungsvorhabens 'Rotation der Erde'*, **118**, 133–140. x, 7

Petit, G., and B. Luzum, 2010: IERS convention 2010. *IERS Technical Note*, **36**. vii, xiii, 1, 2, 36

Petrachenko, B., 2009: Progress Report of the IVS VLBI2010 Committee: Desing Aspects of the VLBI2010 System. *Technical report*, **IVS VLBI 2010 Committee**. ix, 5

Universitat d'Alacant
Universidad de Alicante

Plag, H., and M. Pearlman, 2009: Global Geodetic Observing System: Meeting the Requirements of a Global Society on a Changing Planet in 2020. *Springer*, 332 pages, doi:978-3-642-02687-4. 11, 27

Richter, B., 1988: Chandler effect and Nearly Diurnal Free Wobble as determined from observations with superconducting gravimeter. *Proc. 128 IAU Symp.*, **Kluwer Academic**, 309–315. 34

Risbey, J. S., S. Lewandowsky, C. Langlais, D. P. Monselesan, T. J. O'Kane, and N. Oreskes, 2014: Well-estimated global surface warming in climate projections selected for ENSO phase. *Nat. Clim. Change*, **4**, 835–840, doi:10.1038/nclimate2310. 70

Rodell, M., K. Mitchell, M. Bosilovich, D. Toll, and D. Lohmann, 2004: The global land data assimilation system. *Bull. am. Meteorol. Soc.*, **85(3)**, 381–394. 53

Santer, B. D., and Coauthors, 2014: Volcanic contribution to decadal changes in tropospheric temperature. *Nat. Geosci.*, **7**, 185–189, doi:10.1038/ngeo2098. xxiv, 70

Schuh, H., and D. Behrend, 2012: VLBI: A fascinating technique for Geodesy and astrometry. *J. Geodyn.*, **61**, 68–80, doi:10.1016/j.jog.2012.07.007. 4

Schuh, H., and J. Böhm, 2013: Sciences of Geodesy. *G.Xu (ed.)*, **Springer-Verlag Berlin Heidelberg**. viii, ix, 3, 5

Schuh, H., B. Richter, and S. Nagel, 2000: Analysis of Long Time Series of Polar Motion. *Polar Motion: Historical and Scientific Problems. ASP Conference Series. IAU Colloquium*, **208**, 321, doi:1-58381-039-0. 34

Seitz, M., D. Angermann, M. Blobfeld, H. Drewes, and M. Gerstl, 2012: The 2008 DGFI realization of the ITRS: DTRF2008. *J. Geod*, **86**, 1097–1123, doi:10.1007/s00190-012-0567-2.

Shirai, T., and T. Fukushima, 2000a: Improvement of Nonrigid-Earth Nutation Theory by adding a Model Free Core Nutation Term. *Proc. of IAU Colloquium*, **180**, 223–229. 34

Shirai, T., and T. Fukushima, 2000b: Numerical convolution in the time domain and its application to the nonrigid-Earth nutation theory. *Astron. J.*, **119**, 2475–2480, doi:10.1086/301359. 34

Universitat d'Alacant
Universidad de Alicante

Shirai, T., and T. Fukushima, 2001: Construction of a new forced nutation theory of nonrigid Earth. *Astron. J.*, **121**, 3270–3283, doi:10.1086/321067. 36

Smith, M., 1977: Wobble and nutation of the Earth. *Geophys. J. R. Astron. Soc.*, **50**, 103–140, doi:10.1111/j.1365-246X.1977.tb01326.x. xvi, 33

Stammer, D., C. Wunsch, I. Fukumori, and J. Marshall, 2002: State estimation in modern oceanographic research. *Trans. Am. Geophys. Un.*, **83**, 294–295. 53

Sun, J., J. Böhm, T. Nilsson, H. Krásná, S. Böhm, and H. Schuh, 2014: New VLBI2010 scheduling strategies and implications on the terrestrial reference frames. *J. Geod.*, **88**. 6

Swenson, S., and J. Wahr, 2002: Methods for inferring regional surface mass anomalies from Gravity Recovery and Climate Experiment (GRACE) measurements of time-variable gravity. *J. Geophys. Res.*, **107(B9)**, 2193, doi:10.1029/2001JB000576. xx, 48, 56

Swenson, S., and J. Wahr, 2006: Post-processing removal of correlated errors in GRACE data. *J. Geophy. Res.*, **33**, L08 402, doi:10.1029/2005GL025285. xx, xxi, 12, 48, 49

Tapley, B., S. Bettadpur, M. Watkins, and C. Reigber, 2004: The Gravity Recovery and Climate Experiment: Mission overview and early results. *Geophys. Res. Lett.*, **31**, L09 607, doi:10.1029/2004GL019920. 9

Toomre, A., 1974: On the Nearly Diurnal Wobble of the Earth. *Geophys. J. R. Astron. Soc.*, **38**, 335–348, doi:10.1111/j.1365-246X.1974.tb04126.x. xvi, 33

Trottini, M., I. Vigo, and S. Belda, 2015: On the use of Running Trends as Summary Statistics for Univariate Time Series and Time Series Association. *J. Clim.*, **In review**.

Velicogna, I., and J. Wahr, 2006: Measurements of time-variable gravity show mass loss in Antarctica. *Sci.*, **311**, 1754–1756. 57

VondraK, J., and C. Ron, 2014: Geophysical excitation of nutation - comparison of different models. *Acta Geodyn. Geomater*, **11 No. 3 (175)**, 193–200, doi:10.13168/AGG.2014.0007. 23

Universitat d'Alacant
Universidad de Alicante

Wahr, J., 1981: The forced nutations of an elliptical, rotating, elastic and oceanless Earth. *Geophys. J. R. Astron. Soc.*, **64**, 705–727, doi:10.1111/j.1365-246X.1981.tb02691.x. xvii, 33

Wahr, J., M. Molenaar, and F. Bryan, 1998: Time-variability of the Earth's gravity field: hydrological and oceanic effects and their possible detection using GRACE. *J. Geophys. Res.*, **103**, 30 205–30 229. xx, xxi, 47, 49, 56

Watkins, M., and D.-N. Yuan, 2012: JPL level-2 processing standards document for level-2 product release 05, revision 5.0. *Available at: http://podaac.jpl.nasa.gov/gravity/grace-documentation*, **Revision 5.0**. 47

Watts, R., and M. Morantine, 1991: Is the greenhouse gas-climate signal hiding in the deep ocean. *Clim. Change*, **18(4)**, iii–vi, doi:10.1007/BF00142966. xi, 10

Zhang, Z., B. Chao, Y. Lu, and H. Hsu, 2009: An effective filtering for GRACE time-variable gravity: fan filter. *Geophys. Res. Lett.*, **36**, L17 311, doi:10.1029/2009GL039459. xx, xxiii, 13, 48, 64

Universitat d'Alacant
Universidad de Alicante

# Acronyms

**AAM** Atmospheric angular momentum

**AC** Analysis Centers

**CHAMP** Challenging Minisatellite Payload

**CIO** Celestial Intermediate Origin

**CIP** Celestial Intermediate Pole

**CMIP5** Couple Model Intercomparison Project 5

**CRF** Celestial Reference Frame

**CSR** Center for Space Research

**DORIS** Doppler Orbitography Integrated by Satellite

**ECCO** Estimating the Circulation and Climate of the Ocean

**EOP** Earth Orientation Parameters

**ERA** Earth rotation angle

**ERP** Earth Rotation Parameters

**FCN** Free Core Nutation

**FICN** Free Inner Core Nutation

**GCRS** Geocentric Celestial Reference System

**GEO** Group on Earth Observations

Universitat d'Alacant
Universidad de Alicante

**GEOSS** Global Earth Observing System of Systems

**GFZ** GeoForschungsZentrum

**GGOS** Global Geodetic Observing System

**GLDAS** Global Land Data Assimilation Systems

**GMSL** Global Mean Sea Level

**GMST** Global mean surface air temperature

**GNSS** Global Navigation Satellite Systems

**GOCE** Gravity Field and Steady-State Ocean Circulation Explorer)

**GRACE** Gravity Recovery

**GST** Global surface temperature

**HAM** Hydrological angular momentum

**IAG** International Association of Geodesy

**ICRF** International Celestial Reference Frames

**ICRF2** International Celestial Reference Frame 2

**ICRS** International Celestial Reference System

**IERS** International Earth Rotation and Reference System Service

**IGS** International GNSS Service

**ITRF** International Terrestrial Reference Frames

**ITRS** International Terrestrial Reference System

**JGW** Joint Working Group

**JPL** Jet Propulsion Laboratory

**LOD** Length of day

Universitat d'Alacant
Universidad de Alicante

**LS** Least Squares

**NDFW** Nearly Diurnal Free Wobble

**NNR** No Net Rotation

**OAM** Oceanic angular momentum

**OBP** Ocean Bottom Pressure

**OHC** Ocean heat

**PDO** Pacific Decadal Oscillation

**PGR** Post Glacial Rebound

**PM** Polar Motion

**POD** Precise Orbit Determination

**RAEGE** New Atlantic Network of Geodynamical and Space Stations

**RL04** Release 04

**RL05** Release 05

**rms** Root Mean Square

**RTA** Running Trend Analysis

**SC** Stokes coefficients

**SD** Standard Deviation

**SLP** Sea Level Pressure

**SLR** Satellite Laser Ranging

**SLV** Sea Level Variation

**TE** Earth System

**TIO** Terrestrial Intermediate Origin

Universitat d'Alacant
Universidad de Alicante

**TRF** Terrestrial Reference Frame

**TWS** Terrestrial Water Storage

**USNO** United States Naval Observatory

**UT1** Universal Time

**VieVS** Vienna VLBI Software

**VLBI** Very Long Baseline Interferometry

**VMF1** Vienna Mapping Functions

**WM** Weighted Mean

**WRMS** Weighted Root Mean Square

**WTE** Water Thickness equivalent

Universitat d'Alacant
Universidad de Alicante

# Declaration

I herewith declare that I have produced this work without the prohibited assistance of third parties and without making use of aids other than those specified; notions taken over directly or indirectly from other sources have been identified as such. This work has not previously been presented in identical or similar form to any examination board.

The dissertation work was conducted from 2011 to 2015 under the supervision of José Manuel Ferrándiz Leal at the University of Alicante.

Alicante,

Universitat d'Alacant
Universidad de Alicante

This dissertation was finished writing in Alicante on Tuesday 1st September, 2015

Universitat d'Alacant
Universidad de Alicante

Universitat d'Alacant
Universidad de Alicante